iMALDI as a tool to improve patient stratification for targeted cancer therapies

by

Robert Popp
BSc, University of Applied Sciences Fresenius, Germany, 2012
MSc, University of Applied Sciences Fresenius, Germany, 2013

A Dissertation Submitted in Partial Fulfillment
of the Requirements for the Degree of

DOCTOR OF PHILOSOPHY

in the Department of Biochemistry and Microbiology

Supervisory Committee

iMALDI as a tool to improve patient stratification for targeted cancer therapies

by

Robert Popp
BSc, University of Applied Sciences Fresenius, 2012
MSc, University of Applied Sciences Fresenius, 2013

Supervisory Committee

Dr. Christoph H. Borchers, Department of Biochemistry and Microbiology
Supervisor

Dr. Caroline E. Cameron, Department of Biochemistry and Microbiology
Departmental Member

Dr. John E. Burke, Department of Biochemistry and Microbiology
Departmental Member

Dr. J. Scott McIndoe, Department of Chemistry
Outside Member

Abstract

The PI3K/AKT/mTOR signaling pathway is commonly dysregulated in cancer. The goal of this thesis project was to assess the hypothesis of a strong correlation between PI3K/AKT/mTOR pathway activity and the response to targeted therapies, by using a protein quantitation technique called immuno-matrix assisted laser desorption/ionization (iMALDI).

The use of iMALDI as a clinical tool was demonstrated by automating an established iMALDI assay for quantifying plasma renin activity. The results from the automated method gave high correlation coefficients of ≥0.98 with a clinical LC-MS/MS method and could be performed significantly faster than with manual sample preparation. The 7.5-fold faster analysis compared to LC-MS/MS, reduction in human error, and higher throughput, demonstrated the suitability of this assay for clinical use.

The automated iMALDI platform was then adapted for use with cancer cell lines and tissue analysis, targeting the kinases AKT1 and AKT2 as surrogate proteins for signaling pathway activity. Using minute amounts (10 µg/capture), AKT1 and AKT2 expression and phosphorylation stoichiometry (PS) were successfully quantified via their C-terminal tryptic peptides, which encompassed key phosphorylation sites. After assay optimization, the assays were analytically validated for linear range, accuracy, and interferences. In addition, PS cut-off values based on measurement errors were established for confident PS quantitation. The functionality of the assay was demonstrated with cell lines, and flash-frozen and FFPE tissue lysates, with, on average, lower AKT1/AKT2 measurements obtained from FFPE samples. The developed assays were sensitive and precise enough to detect differences between matched normal and adjacent tumor tissues.

To answer the hypothesis, patient-derived xenograft (PDX) mouse-model tumors treated with Herceptin, Everolimus, a combination of both (E+H), or with no treatment, were assessed for molecular patterns linked to tumor response. One mouse from the E+H group showed a partial response, with elevated total and phosphorylated AKT1/AKT2. Unfortunately, overlapping values between treatment groups were obtained in this study,

and the large within-group spread and the low number of biological replicates made it difficult to confirm a definite correlation between PI3K/AKT/mTOR pathway activity and response to treatment. A follow-up study with additional protein targets, a larger number of samples, and serial biopsies will be required to determine if there is, in fact, a correlation between PI3K/AKT/mTOR pathway activity and response to treatment.

Table of Contents

List of Tables

List of Appendix Tables

List of Figures

List of Appendix Figures

List of Abbreviations

Abbreviation	Meaning
AAA	Amino acid analysis
ACE	Angiotensin-converting enzyme
ACN	Acetonitrile
ADT	Androgen-deprivation therapy
AKT	Protein kinase B
ALL	Acute lymphocytic leukemia
AmBic	Ammonium bicarbonate
AML	Acute myelogenous leukemia
APC	Adenomatous polyposis coli protein
ATCC	American Type Culture Collection
ATP	Adenosine triphosphate
BCA	Bicinchoninic acid
BSA	Bovine serum albumin
CAR	Chimeric antigen receptor
CEWA	Chicken egg white albumin
CHAPS	3-[(3-Cholamidopropyl)dimethylammonio]-1-propanesulfonate
CISH	Chromogenic in situ hybridization
CLL	Chronic lymphocytic leukemia
CML	Chronic myelogenous leukemia
CPTAC	Clinical Proteomic Tumor Analysis Consortium
CRC	Colorectal cancer
CTLA-4	Cytotoxic T-lymphocyte-associated protein 4
CV	Coefficient of variation
CZE	Capillary zone electrophoresis
DDA	Data-dependent acquisition
DOC	Sodium deoxycholate
DTT	Dithiothreitol
EDTA	Ethylenediaminetetraacetic acid
EGFR	Epidermal growth factor receptor
ELISA	Enzyme-linked immunosorbent assay
END	Endogenous peptide
ER	Estrogen receptor
FA	Formic acid
FAK	Focal adhesion kinase
FBS	Fetal bovine serum
FDA	U.S. Food and Drug Administration
FFPE	Formalin-fixed paraffin-embedded
FISH	Fluorescence in situ hybridization
FT/ICR	Fourier-Transform/Ion Cyclotron Resonance

Abbreviation	Meaning
GnHCl	Guanidine hydrochloride
GPCR	G protein-coupled receptor
HCCA	α-Cyano-4-hydroxycinnamic acid
HCl	Hydrochloric acid
HER2	Epidermal growth factor receptor 2
HER3	ErbB3
IAA	Iodoacetamide
ICC	Immunocytochemistry
ICPC	International Cancer Proteogenome Consortium
IGF-1	Insulin growth factor 1
IHC	Immunohistochemistry
IMAC	Immobilized metal affinity chromatography
iMALDI	immuno-matrix assisted laser desorption/ionization
IRS1	Insulin receptor substrate 1
iTRAQ	Isobaric tags for relative and absolute quantitation
JGH	Jewish General Hospital
LC-MS	Liquid chromatography mass spectrometry
LDT	Laboratory developed test
LLOQ	Lower limit of quantitation
LOD	Limit of detection
m/z	Mass to charge ratio
MALDI	Matrix assisted laser desorption/ionization
MEK	Mitogen-activated protein kinase kinase
MIR	Mortality Incidence ratio
MRM	Multiple reaction monitoring
MS	Mass spectrometry
MS/MS	Tandem mass spectrometry
mTOR	Mechanistic target of rapamycin
mTORC1/mTORC2	mTOR complexes 1 and 2
NAT	Natural (light) version of a peptide
NCD	Non-communicable disease
NCI	US National Cancer Institute
NGS	Next-generation sequencing
NMI	Natural and Medical Sciences Institute
OECD	Organisation for Economic Co-Operation and Development
PBS	Phosphate buffered saline
PBSC	Phosphate buffered saline + 0.015% CHAPS
PD	Progressive disease
PD-1	Programmed cell death protein 1
PD-L1	Programmed death-ligand 1
PDK1	3-phosphoinositide-dependent protein kinase 1

Abbreviation	Meaning
PDX	Patient-derived xenograft
PI3K	Phosphatidylinositol-3-kinase
PIKK	Phosphoinositide-3-kinase-related protein kinase
PIP_2	Phosphatidylinositol-4,5-bisphosphate
PIP_3	Phosphatidylinositol-3,4,5-trisphosphate
PMSF	Phenylmethane sulfonyl fluoride
PPQ	Phosphatase-based phosphopeptide quantitation
PR	Partial response
PRM	Parallel reaction monitoring
PS	Phosphorylation stoichiometry
PTEN	Phosphatase and tensin homolog
PTM	Post-translational modification
RAAS	Renin angiotensin aldosterone system
RNA-seq	RNA sequencing
RPMI	Roswell Park Memorial Institute
RT	Room temperature
RTK	Receptor tyrosine kinase
RT-PCR	Real time polymerase chain reaction
S/N	Signal to noise ratio
SD	Stable disease
SDS	Sodium dodecyl sulphate
SILAC	Stable isotope labeling in cell cultures
SIS	Stable isotope-labeled standard
SISCAPA	Stable Isotope Standards and Capture by Anti-Peptide Antibodies
SMKI	Small molecule kinase inhibitor
SPPS	Solid phase peptide synthesis
TARGET	Therapeutically Applicable Research to Generate Effective Treatments
TBS	Tris-buffered saline
TBSC	Tris-buffered saline + 0.015% CHAPS
TCEP	Tris(2-carboxyethyl)phosphine
TCGA	The Cancer Genome Atlas
T-DM1	Ado-trastuzumab emtansine
TFA	Trifluoroacetic acid
TLCK	Tosyl-L-lysyl-chloromethane hydrochloride
TOF	Time of flight
TSC1/TSC2	Tuberous sclerosis protein 1 and 2
UICC	Union for International Cancer Control
VEGF	Vascular endothelial growth factor
WHO	World Health Organization

Acknowledgments

I would like to acknowledge several people involved in this thesis project: Dr. Christoph Borchers for giving the opportunity and support to work on this project; members of the Jewish General Hospital for providing samples and advice, including Dr. Adriana Aguilar-Mahecha, Dr. Mark Basik, Dr. René Zahedi, Dr. André LeBlanc, and Dr. Gerald Batist; Dr. Michael Chen for providing access to the MALDI-TOF instrument at the Victoria General Hospital; Björn Fröhlich, David Lin, Dr. David Malmström, and Dr. Huiyan Li for general support; Karl Makepeace for growing and providing *E. coli* cells; Angela Jackson and Darryl Hardie for their support and discussions, as well as Dr. Oliver Pötz for discussion and advice related to antibodies; and Adam Pistawka, Nick Sinclair and Jillaine Proudfoot for peptide synthesis and purification. I would also like to thank Grace van der Gugten and Dr. Daniel Holmes from St. Paul's Hospital for their support with the plasma renin activity project. I am further grateful to Dr. Carol Parker for proof-reading and suggesting edits for manuscripts.

I would further like to acknowledge my committee members Dr. Caroline Cameron, Dr. John Burke, and Dr. Scott McIndoe for their input, and the University of Victoria for funding, fellowships, awards, and scholarships. Additionally, I am grateful for financial support from external funders, including the James A. & Laurette Agnew Memorial Scholarship, the Dr. Julius F. Schleicher Graduate Scholarship, and the Yvonne Allen Cancer Research Scholarship. Lastly, I would to acknowledge the organizations that provided financial support for the project itself, namely Genome Canada and Genome British Columbia.

Dedication

I dedicate this thesis to my wife Claudia for all her support, our two dogs Canela and Lyla for forcing me to take breaks every now and then, and my parents for their lifelong support and allowing me to do whatever I wanted to do (within reason).

Chapter 1: Introduction

1.1 Cancer

Cancer, also called malignancy, is defined as a "group of diseases characterized by uncontrolled growth and spread of abnormal cells" (American Cancer Society, 2016a). In contrast to benign cell growths, malignancies are characterized by their potential or ability to metastasize through the blood and lymph systems or to invade adjacent tissues, and by not being self-limited regarding growth.

1.1.1 *Classification*

Cancers are classified in a variety of ways. The most common ways of classification are based on the origin of the cancer by tissue type (histological type), by the primary site in the body, or by a combination of both.

The major histological cancer categories are carcinoma, sarcoma, myeloma, leukemia, lymphoma, central nervous system cancers, and mixed types (U. S. National Institutes of Health, 2018). Carcinomas are malignancies of epithelial tissue and are further sub-divided into adenocarcinoma which develop in organs or glands (e.g. adenocarcinoma of the colon or esophagus), and squamous cell carcinoma, which is a type of skin cancer and originates in squamous epithelial cells. Sarcomas originate in connective and supportive tissues including bones, cartilage, muscle and fat. Examples include sarcomas of the bone (osteosarcoma), liposarcoma (adipose tissue) or leiomyosarcoma (smooth muscle). Myeloma relates to cancers that originate in the plasma cells of the bone marrow. It can be sub-classified into multiple myeloma which affects several areas of the body, whereas plasmacytoma describes a condition where only a single site of myeloma cells is evident in the body. Furthermore, localized myeloma describes the evidence of myeloma cells in neighbouring sites, whereas extramedullary myeloma describes the involvement of tissues other than the bone marrow, including lungs, muscles, and skin.

Leukemia is a summary term for cancers of the bone marrow which is often associated with the overproduction of immature white blood cells. Leukemia is further categorized into acute or chronic lymphocytic leukemia (ALL, CLL) and acute or chronic myelogenous leukemia (AML, CML), depending on whether the white blood cells are more like stem cells and cannot mature properly (acute), or mature (chronic), and whether the cancer cells originate in lymphoid progenitor (lymphocytic) or myeloid progenitor cells (myelogenous). Lymphomas are cancers that develop in the glands or nodes of the lymphatic system. For example, primary central nervous system lymphomas are classified into Hodgkin and non-Hodgkin lymphomas. These are characterized by the presence of Reed-Sternberg cells in Hodgkin lymphoma. Additionally, mixed cancer types exist which show characteristics of multiple categories, such as adenosquamous carcinoma or carcinosarcoma.

Due to their significant heterogeneity, cancers are further sub-classified into clinically relevant subtypes -- which affect treatment decisions and prognosis -- by using molecular profiling approaches. For example, Sorlie et al. defined five breast cancer sub-groups based on hierarchical clustering, linking gene-expression profiling data to clinical outcomes (Sorlie et al., 2001), and extensive research efforts today aim at refining the sub-classification process to establish molecular features that allow the highest probability of treatment success for patients. Overall, more than 200 different forms of cancer with various subtypes are known, each with different genetic abnormalities such as somatic mutations, copy number variations, changed gene profiles, and epigenetic alterations (Lahtz and Pfeifer, 2011; Tomczak et al., 2015).

1.1.2 *Cancer statistics*

Incidence and mortality

Second only to cardiovascular disease, cancer is the major non-communicable disease contributor to worldwide mortality, with 14.1 million new diagnoses and 8.2 million global deaths in 2012 (Ferlay J. et al., 2013; World Health Organization, 2015). The most commonly diagnosed cancers (in male and female patients combined) were lung, breast,

and colorectal cancers (CRC) (1.82, 1.67, and 1.36 million, respectively), while the most frequent mortalities were attributed to lung, liver, and stomach cancers (1.59, 0.75 and 0.72 million, respectively) (Figure 1A). Interestingly, for some cancers such as lung and liver cancer, the mortality-to-incidence ratio (MIR) is significantly higher than in other cancers such as breast, colorectal, and prostate. This could be attributable to biological differences in the virulence of disease, as well as to differences in the feasibility of and access to screening and diagnostic services, treatment, and follow-up procedures (Hébert et al., 2009). In addition to the type of cancer, the MIR can further vary significantly based on other measures such as gender and socioeconomic disparities (Wong et al., 2017), and may be useful for estimating prognosis (L. Ellis et al., 2014). Overall, the differences in MIR indicate great heterogeneity in terms of patient outcome for various cancers.

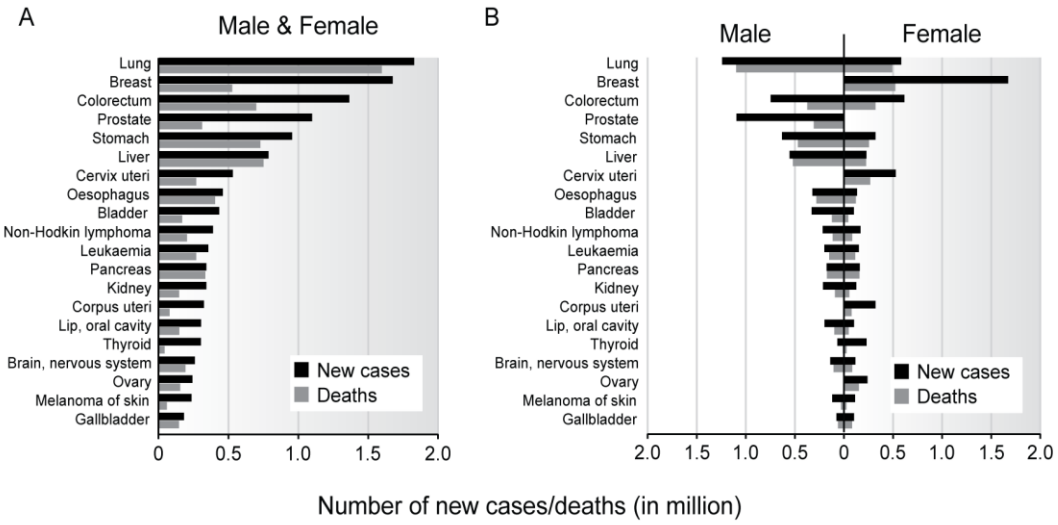

Figure 1: Numbers of new cases and deaths of the 20 most common cancers in 2012. (A) Male & female numbers combined; (B) Numbers separate for male and female. Data from (Ferlay J. et al., 2013).

As can be seen from Figure 1B, the types of cancer with the most new cases and deaths in 2012 further varied by gender. For instance, the most commonly diagnosed cancer type in females was breast cancer, followed by colorectal and lung cancer. In comparison, in the male world population, lung, prostate, and colorectal cancers were diagnosed most often.

According to the World Health Organization (WHO), the worldwide age-standardized cancer mortality rate has decreased by 6% between 2000 and 2012 (World Health Organization, 2015). It must be pointed out, however, that this average number is composed of significant regional, gender, and cancer type variations (Figure 2).

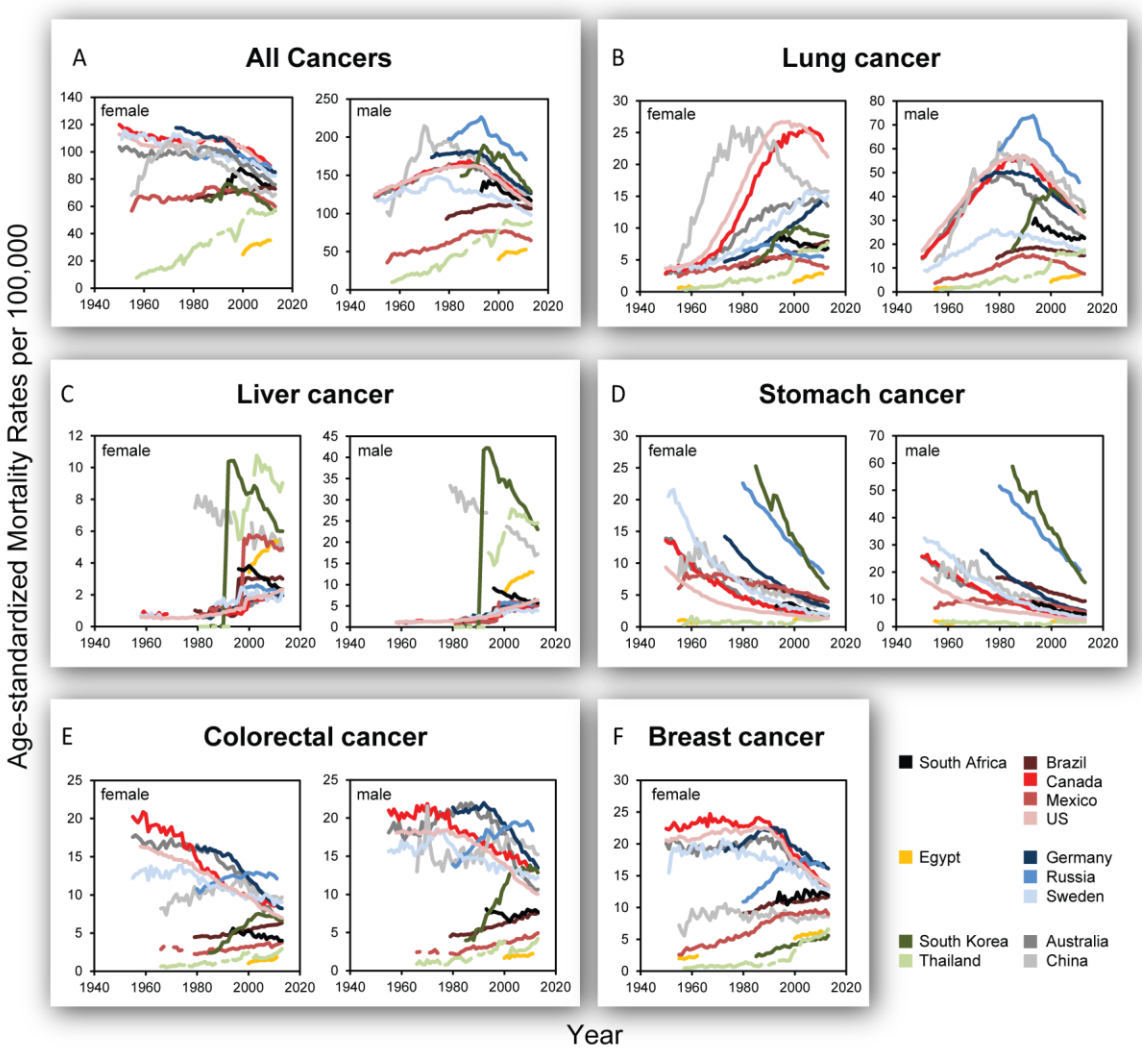

Figure 2: Age-standardized mortality rates over time. (A) All cancers, and the cancers with the highest worldwide mortality rates, in decreasing order: (B) lung cancer, (C) liver cancer, (D) stomach cancer, (E) colorectal cancer, and (F) breast cancer. Mortality rates show varying trends depending on region, gender, and cancer type.

For example, the largest overall improvement in cancer mortality by region during 2000 and 2012 was in the high-income OECD (Organisation for Economic Co-operation and Development) countries (e.g. the US, Canada, Western European countries, and Australia), due to significant reductions in lung cancer mortality in men, stomach and colorectal cancer in men and women, and breast cancer in women (World Health Organization, 2015). In contrast, mortality rates in South-East Asian countries such as Thailand increased. An example of opposing trends between the male and female population can be observed for lung cancer patients in Germany (Figure 2B), where the male population has shown a steady decrease in mortality since the 1980s, while the female mortality rate keeps increasing.

Factors affecting the cancer mortality rates

The trends of declining or increasing mortality rates are influenced by a variety of factors: improved prevention, reduced exposure and risk behaviors, as well as early detection, diagnosis, and treatment (World Health Organization, 2015).

Prevention is key, as has been suggested by an estimated 42% of cancers that are preventable (Islami et al., 2018), and as evidenced by the impact of reduced tobacco use [the single highest risk factor for cancer (Lim et al., 2012)] in high-income countries, resulting in a decline in worldwide lung cancer mortality (World Health Organization, 2015). Furthermore, a significant decrease in stomach cancer incidence and mortality worldwide has been attributed to reductions in salt intake, increased consumption of fruits and vegetables, and improved hygiene resulting in reduced infections caused by *Helicobacter pylori* (Ezzati and Riboli, 2012).

Another important factor to reduce exposure and risk behaviors and thus reduce cancer mortality rates is to implement proper legislation, such as raising taxes on tobacco and alcohol, and limiting exposure to environmental and occupational risk factors (World Health Organization, 2015).

Lastly, early detection, diagnosis, and treatment have been shown to positively impact mortality rates. For instance, the prognosis of early stage cancers has been shown to be

significantly improved when compared to later stage cancers, as evidenced by the 90% survival rate of localized, early stage CRC patients, compared to only 13% for patients with metastatic disease (American Cancer Society, 2016a). This is especially important considering that -- depending on the cancer type -- a substantial portion of patients have advanced stage cancer at the point of diagnosis. Whereas only 5% of female breast cancer patients are diagnosed with metastatic-stage cancer, uterine-, cervix-, colorectal-, stomach-, and lung-cancer patients show significantly higher percentages -- 13%, 19%, ~30%, and ~50-60%, respectively (American Cancer Society, 2016a). Furthermore, simultaneously increasing cancer incidence rates and decreasing mortality rates in high-income countries suggest improvements in health care (Global Burden of Disease Cancer Collaboration, 2015).

Economic burden and large-scale initiatives

In addition to the personal burden, cancer has a major global economic impact. Factoring in the costs related to prevention and treatment of cancer, the disability caused, as well as the economic value of lives lost, was approximately USD 1.16 trillion in 2010. Further considering the long-term costs to patients and their families increased the estimates to USD 2.5 trillion (Union for International Cancer Control, 2014).

To reduce and control the prevalence of preventable non-communicable diseases such as cancer, and thereby reduce the associated economic and personal burdens, large-scale organizations and initiatives such as the WHO's Global NCD Action Plan 2013-2020 (World Health Organization, 2013), the Union for International Cancer Control (UICC)'s World Cancer Declaration 2013 (Union for International Cancer Control, 2013), and Cancer Breakthroughs 2020 [previously called Cancer Moonshot 2020, (Lowy, 2017)] have been established to provide guidance for governments to implement preventative measures, improve early diagnosis and screening, strengthen healthcare systems, implement vaccination programs, and improve treatment and palliative care, as well as to provide funding and a collaborative structure to accelerate research findings with the goal of improved patient care. Additionally, research initiatives such as The Cancer Genome Atlas (TCGA), the US National Cancer Institute (NCI)'s Clinical Proteomic Tumor

Analysis Consortium (CPTAC), and the International Cancer Proteogenome Consortium (ICPC) were established to advance research findings in a collaborative fashion and thereby drive the development of more effective treatments.

1.1.3 *Causes of cancer*

It is well established that cancer is caused by the accumulation of genetic and epigenetic alterations such as mutations and rearrangements in genes that regulate cell survival and migration, giving cancer cells a growth advantage over normal cells (Sever and Brugge, 2015).

The causes for these alterations can be induced by environmental factors, inherited, or caused by random DNA replication errors. The contribution of each of these factors is a matter of debate. Until recently, it had been estimated that the majority (>90%) of cancers were linked to a variety of environmental and lifestyle-related risk factors, rather than inherited predispositions (Anand et al., 2008). It had been estimated that one third of all cancers were caused by five behavioral and dietary risks: high body mass index, low fruit and vegetable intake, lack of physical activity, tobacco use, and alcohol use (Ott et al., 2011). Another major risk factor is infections, mainly caused by *Helicobacter pylori*, human papillomavirus, and hepatitis B and C viruses, which are estimated to be linked to approximately 16% of all cancers globally (de Martel et al., 2012). Additional risk factors include carcinogens such as extracted (e.g. benzene) or mined substances (e.g. asbestos), synthetic chemicals (e.g. vinyl chloride), complex mixtures (e.g. coal tar), or various types of radiation (e.g. ultraviolet radiation) (U.S. Department of Health and Human Services, 2016).

However, a recent study that used mathematical modeling to determine how genetic mutations in cancer arise, concluded that across 69 countries and 17 cancer types an average of approximately 66% of cancer-driving mutations are caused by random DNA replication errors, whereas only 29% are due to the environment, and 5% are inherited (C. Tomasetti et al., 2017). This initiated a fierce debate, since the results could have a significant impact on decision makers regarding preventative measures (Ledford, 2017).

Genetic changes in cancer

The genes responsible for cancer development are called driver genes and can be grouped into proto-oncogenes and tumor suppressor genes. Proto-oncogenes are genes which are typically involved in controlled cell growth. Upon mutation, copy number alterations, rearrangements, or epigenetic alterations, these genes turn into oncogenes, resulting in uncontrolled activation. An example of a commonly mutated or amplified oncogene in a variety of cancers is *PIK3CA* which encodes the catalytic subunit p110α of the Class IA phosphatidylinositol-3-kinase (PI3K) and leads to increased PI3K/AKT signaling (Polivka and Janku, 2014; Shayesteh et al., 1999). In contrast, tumor suppressor genes are negative regulators of cell signaling processes and are typically responsible for decreasing cell division rates, DNA repair, or are involved in apoptotic processes. Examples of frequently mutated tumor suppressor genes include *TP53* which encodes the transcription factor p53, a key regulator of apoptosis, cell cycle arrest, DNA repair, and cell metabolism (Gurpinar and Vousden, 2015), and *APC* which encodes the adenomatous polyposis coli (APC) protein that is involved in Wnt signaling (Ciriello et al., 2013). When mutated, the tumor suppressor genes are unable to fulfill these tasks and allow the cancer cells to proliferate (Shlien et al., 2015). Interestingly, most mutations in cells are passenger rather than driver mutations. Whereas passenger mutations have little or no impact on the phenotype, driver mutations give the cancer cells their characteristic phenotypes. In fact, a mathematical model based on epidemiologic and genome-wide sequencing data in colorectal and lung cancer suggested that only three driver mutations are required to develop cancer (Cristian Tomasetti et al., 2015). Moreover, it has been estimated that each driver mutation gives cells only a very small, selective growth advantage that drives progression (~0.4%) which, over time, is sufficient to generate significant tumor growth (Bozic et al., 2010). Additionally, the accumulation of passenger mutations has been shown to slow down tumor growth and reduce metastatic progression (McFarland et al., 2017).

1.2 Cancer treatment

1.2.1 *Traditional treatment techniques*

The treatment of cancer patients today encompasses an array of different techniques, which are commonly applied simultaneously or sequentially. These techniques include surgical removal of early stage cancers, chemotherapy, radiation therapy, and hormone therapy. Targeted therapies such as immunotherapy or targeted cell signaling inhibitor therapies, often combined with chemotherapy, are aimed at patients with advanced disease. The choice of technique depends on a variety of factors, including the tumor location, tumor grade and stage, the health of the patient prior to treatment, whether the patient has received previous treatment, the existence of certain biomarkers such as mutations or proteins, and others (Miller et al., 2016).

Surgery

The oldest technique and still a primary method for early cancer treatment is surgery and serves different purposes, including cancer diagnosis, partial or complete tumor removal, determination of tumor location, assessment of cancer spread, restoration of a patient's bodily functions and appearance, as well as relief from side effects (National Cancer Institute, 2015). Besides removing tissues by scalpel, tissues can be removed via endoscopy, cryosurgery, or by means of laser cutting.

Chemotherapy

Chemotherapy describes the systemic or regional treatment of the patient with cytotoxic drugs, such as cyclophosphamide, administered either orally or via injection. These drugs interfere with cell division of rapidly dividing cells. The first chemotherapy treatment was established in 1942 (Christakis, 2011), and today it is often a first or second line of treatment across various cancers, often in combination with other treatments such as surgery, radiation therapy, targeted therapy, and also in high doses as part of stem cell transplantation (Miller et al., 2016). While chemotherapies in general result in improved

patient response rates, some studies show that these responses are not durable and thus do not result in improvements in progression free survival (PFS), for instance in patients with metastatic Merkel cell carcinoma (Iyer et al., 2016). Furthermore, combination chemotherapies have been shown to have no benefit over single-drug treatments in advanced stage metastatic breast-cancer patients (Sledge et al., 2003). In contrast, chemotherapy has been shown to improve overall survival in early-stage breast cancer patients, in particular in younger patients (Early Breast Cancer Trialists' Collaborative Group (EBCTCG), 2005), with combination therapies resulting in a significant improvement in overall survival. This emphasizes that early detection and treatment are key to harnessing the benefits of chemotherapy treatment.

Another drawback of chemotherapy treatments is potentially severe side effects due to their non-specific impact on normal cells, in particular blood-forming cells in the bone marrow, hair follicles, as well as cells in the mouth, digestive tract, and reproductive system. These effects result in a multitude of potential side effects such as hair loss, infection, fatigue, bloody stool, and others (American Cancer Society, 2016b). Moreover, the carcinogenic effects of cytotoxic drugs such as cyclophosphamide are a concern, especially regarding secretion of these drugs into the environment (Kummerer and Al-Ahmad, 2010). On a positive note, it has been shown that while high doses of chemotherapy drugs such as cyclophosphamide are responsible for tumor shrinkage due to their cytotoxic nature, and therefore can cause severe side effects, low doses resulted in selective T-cell depletion, resulting in enhanced anti-tumor effects against pre-existing tumors with less intense impact on the patient. This low-dose approach could therefore be useful when applied in conjunction with immunotherapies (Motoyoshi et al., 2006).

Radiotherapy

Another major type of cancer treatment is radiotherapy, often given in conjunction with chemotherapy and/or surgery. Radiotherapy is most commonly applied externally by irradiating the patient’s body parts or entire body with x-rays or proton beams (National Cancer Institute, 2018). In contrast, internal radiation therapy makes use of radioactive

substances placed in the patient's body or tumor for prolonged periods of time, with the goal of shrinking the tumor size or destroying all cancer cells. The radiation interferes with the DNA repair mechanism and is especially effective on quickly dividing cells such as tumor cells. However, radiation therapy can have short- and long-term side effects such as radiation-induced fibrosis (Straub et al., 2015). Furthermore, the impact of radiation on improving overall survival is modest, as has been shown recently for older rectal cancer patients in a neoadjuvant radiation setting, whereas younger patients indeed showed increased mortality compared to no radiation treatment (L. Wu et al., 2017). In addition, radiotherapy has been implicated with causing secondary cancers (Ng and Shuryak, 2015).

Hormone therapy

A form of targeted therapy includes hormone therapy (also termed endocrine therapy). It is used for the treatment of cancers whose growth is hormone-dependent and its goal is to reduce the chance of cancer recurrence, to slow or stop tumor growth, or to ease cancer symptoms. Hormone therapy aims at manipulating the patient's hormone production by administration of hormones or drugs which inhibit the production or activity of endogenous hormones, or by removing hormone-producing organs such as testis. Hormones, especially steroid hormones, are powerful drivers of gene expression in certain cancer cells (Zarghami et al., 1997). Therefore, altering hormone levels can cause a reduction in tumor growth or even cause cell death.

A common example of hormone therapy is androgen-deprivation therapy (ADT) for aggressive prostate cancer, which has been shown to increase the overall survival when combined with radiotherapy, as compared to radiotherapy alone d (D'Amico et al., 2008). However, hormone therapies such as ADT can have significant side effects including decreased bone mineral density, weight gain, anemia, and others (Nguyen et al., 2015). Another example is the treatment of breast cancer by ovarian ablation (Prowell and Davidson, 2004) or the selective estrogen receptor (ER) modulator tamoxifen, a prodrug for an ER inhibitor, which has been shown to improve overall survival significantly in

ER-positive patients (Early Breast Cancer Trialists' Collaborative Group (EBCTCG), 2005).

1.2.2 *Novel, targeted treatment techniques in the era of precision medicine*

While treatments such as surgery, chemotherapy, radiation therapy, and hormone therapy have been in use against cancer for many decades, their benefit in overall survival has been limited, in particular for advanced-stage cancers. Moreover, chemotherapy and radiation therapy are rather unspecific.

In contrast, targeted therapies are the hallmark of precision medicine whose goal is to identify specific molecular traits of the patient's tumors and the tumor microenvironment which can be targeted and interfered with by suitable inhibitors.

This approach holds the promise to complement or even replace previous treatment strategies by new ways of attacking the tumor cells, by influencing the tumor microenvironment, or by improving the patient's immune response, while being more effective and less harmful than current techniques.

Cell signaling pathway inhibitors

A relatively new field of cancer treatment is the use of drugs interfering with the signaling of cancer cells. Broadly, these types of drugs can be categorized as monoclonal antibodies and small-molecule kinase inhibitors (SMKI). Whereas SMKIs are able to penetrate the cell membrane, and therefore are used to interfere with cell signaling pathways inside the cell, monoclonal antibodies are not able to penetrate the cell membrane and target molecules on the cell surface (Esteva, 2004). The purpose of cell-signaling pathway inhibitors is to directly kill the target cell or to initiate its destruction, and they are used based on the premise that the target proteins are druggable, are often overexpressed, e.g. epidermal growth factor receptor 2 (HER2) (Piccart-Gebhart et al., 2005), or are constitutively activated, such as epidermal growth factor receptor (EGFR) with the T790M mutation (Janne et al., 2015).

Monoclonal antibodies

The first FDA-approved monoclonal antibodies used for targeted anti-cancer therapies were introduced in the late 1990s and early 2000s. Examples include trastuzumab (Herceptin) (U.S. Food and Drug Administration, 1998), cetuximab (Erbitux) (U.S. Food and Drug Administration, 2004a), and bevacizumab (Avastin) (U.S. food and Drug Administration, 2004b). While the first generation of monoclonal antibody therapeutics were of murine origin, later generation antibodies were fully humanized or chimeric to overcome side effects caused by immunogenicity issues (Rebello et al., 1999).

As of this writing, 70 antibody therapeutics used for cancer and other diseases such as asthma have been FDA-approved between 1986 and 2018, six of which had marketing discontinued or were withdrawn. Ten additional monoclonal antibodies are currently under FDA review (The Antibody Society, 2018). The rate of new approvals has been fairly steady in recent years with 6, 9, 6, and 10 approvals during 2014 through 2017 (Kaplon and Reichert, 2018), demonstrating the hope that the medical field and pharmaceutical industry place on this kind of treatment.

Therapeutic monoclonal antibodies are generated to recognize and specifically bind to tumor-associated antigens on the surface of cancer cells or immune cells, which can result in a variety of mechanisms of action. One possibility is the flagging of cancer cells with the therapeutic antibodies, thereby aiding in phagocytosis (Overdijk et al., 2015), antibody-dependent cell-mediated cytoxicity (Wang et al., 2015), or receptor-mediated endocytosis (Ritchie et al., 2013). Another mechanism of action is to block cell growth by interfering with the binding of cell-surface receptors to their ligands, which aims at preventing proliferative cellular signaling. For example, Feng et al. showed that anti-EGFR antibodies increase the susceptibility of CRC-cancer stem cells to chemotherapy-induced apoptosis by affecting autophagy (Feng et al., 2016). In addition, angiogenesis inhibitors such as the VEGF-inhibitor bevacizumab interfere with cancer-cell proliferation by preventing blood-vessel formation and thereby decrease the nutrient supply to the tumor (Ferrara et al., 2004).

Another application of monoclonal antibodies is antibody-drug conjugates to carry cytotoxic or radioactive moieties (Thomas et al., 2016). Here the antibody functions as

the drug-delivery system to the cancer cells, where the toxic compounds get concentrated locally, which results in higher potency and lower systemic side effects. Two monoclonal antibodies using this concept and which received FDA-approval in 2012 and 2011 respectively are ado-trastuzumab emtansine (T-DM1) for the treatment of breast cancer, and brentuximab vedotin for the treatment of Hodgkin lymphoma and ALL (The Antibody Society, 2018).

More recently, monoclonal antibodies were found to be very effective as immunotherapy agents by blocking immune-checkpoint pathways between cancer cells and immune cells (Alexander, 2016). Rather than interfering with *internal* cancer-cell signaling pathways, these therapies aim to disable the inhibitory effect of cancer cells on T-cells, thereby enhancing the antitumor immune response. The first monoclonal antibody of this kind was the cytotoxic T-lymphocyte-associated protein 4 (CTLA-4) inhibitor ipilimumab which received FDA approval in 2011 and has since been the standard of care for advanced melanoma patients (U.S. Food and Drug Administration, 2011). Since then, monoclonal antibodies targeting the proteins programmed cell-death protein 1 (PD-1), found on T-cells, and programmed death-ligand 1 (PD-L1), found on cancer cells, have been approved for various cancers (Alsaab et al., 2017). In addition to CTLA-4, PD-1, and PD-L1, many additional potential immune checkpoint targets exist and are currently under investigation (Khalil et al., 2016).

Immunotherapies have certain advantages over approaches which block cell-signaling pathway members in that they aim to improve the activity of immune cells, rather than killing cancer cells directly. This makes immunotherapies more generic and less dependent on the cancer type. Additionally, the buildup of immunological memory helps to prevent disease recurrence as well as against the evolution of therapy-resistant malignant cancer clones, as evidenced by the durability of long-term survival in treated patients (Schadendorf et al., 2015).

Small molecule kinase inhibitors

Just like monoclonal antibodies, SMKIs are intended to specifically bind to target proteins and interfere with cell-signaling processes of cancer cells. Due to their small size (in the range of typically 300-600 Da (P. Wu et al., 2016)), they can enter the intracellular space and impact cell-signaling pathways downstream from cell-surface receptors.

Most SMKIs are reversible rather than irreversible adenosine triphosphate (ATP) competitive inhibitors and can be grouped into different categories depending on the mechanism used to keep ATP from binding to the kinase ATP-binding pocket. Type I inhibitors bind to the adenine binding site of the ATP pocket, type II inhibitors bind to both the ATP-binding pocket and an adjacent allosteric pocket, and type III inhibitors occupy only an allosteric pocket adjacent to the ATP-binding pocket (P. Wu et al., 2016). This blockade of ATP-binding prevents the activation of downstream signaling pathways, resulting in activation of apoptotic mechanisms, as has been shown for the inhibition of EGFR with gefitinib (Costa et al., 2007).

The first SMKI for treating cancer to receive FDA-approval was imatinib (Gleevec, Novartis), a selective BCR-Abl tyrosine kinase inhibitor and today's standard of care as the first-line treatment for CML patients (U.S. Food and Drug Administration, 2001). It was found to result in durable responses and prolonged event-free and progression-free survival (Kantarjian et al., 2002). As of the beginning of 2017, a total of 35 SMKIs had been approved for clinical use, with 31 being approved for cancer treatment (Berndt et al., 2017). While the approval rate for new small-molecule kinase inhibitors had been significantly lower than for monoclonal antibodies, with an average of only one new approval per year between 2001 and 2010, the approval rate has now increased significantly, with 19 new small molecule kinase inhibitors approved between 2011 and 2015 (P. Wu et al., 2016).

CAR-T-cell therapy

Chimeric antigen receptor (CAR)-T-cell therapy is a type of adoptive T-cell therapy that uses *ex-vivo* manipulation of T-cells to transfer genes encoding synthetic CARs which

recognize specific tumor-associated antigens such as CD19. CD19 is ubiquitously expressed on different types of differentiated B cells, including pro-B cells and memory B cells (Brentjens et al., 2007). Therefore, this type of treatment is of particular interest for the treatment of leukemias and lymphomas, and has shown great success in relapsed and/or refractory pediatric and adult B-cell acute lymphoblastic leukemia (B-ALL) with complete remission in 27/30 children and adults treated with CD-19-directed CAR T-cells (Maude et al., 2014). While CAR-T-cell therapy has been highly successful in hematologic cancers, its application to solid tumors has only had modest success thus far, most likely due to heterogeneous antigen expression, immunosuppressive networks in the tumor microenvironment, and limited tissue penetration of the engineered T-cells into solid tumors (Mirzaei et al., 2017).

Advances and challenges of targeted therapies

One major advantage of targeted therapies is the concept of tailoring the treatment plan towards molecular features to improve the probability of success and result in improved benefits for patients. This concept holds true for the blockade of cancer cell signaling molecules via monoclonal antibodies (Swain et al., 2015), SMKIs (Grothey et al., 2013; Janne et al., 2015), or immunotherapy approaches (Robert et al., 2015) which -- compared to placebo or standard approaches such as chemotherapy or hormone therapy -- have been shown in several studies to result in improved patient response and overall survival, while only mediocre results were achieved in other studies (Leighl et al., 2010; Van Cutsem et al., 2007).

In addition, combination approaches have been shown to significantly improve patient responses compared to monotherapy. For example, metastatic CRC patients treated with the monoclonal antibody cetuximab in combination with chemotherapy showed a higher rate of response (23 vs 11%) and significantly greater median time to progression (4.1 vs 1.5 months) when compared to chemotherapy alone (Cunningham et al., 2004). Another example is the combination of the BRAF inhibitor dabrafenib and the mitogen-activated protein kinase kinase (MEK) inhibitor trametinib, which resulted in improved progression-free survival (9.4 vs 5.8 months) and an increased rate of complete or partial

response (76 vs 54%) compared to monotherapy in BRAF V600-positive metastatic melanoma patients (Keith T. Flaherty et al., 2012b). The same positive trend has been shown for immunotherapies, where the combination of the anti-PD1 antibody nivolumab and the anti-CTLA-4 antibody ipilimumab for the treatment of patients with advanced melanoma resulted in improved overall 3-year survival rates of 58%, compared to 52% and 34% for the nivolumab and ipilimumab monotherapy trial arms (Wolchok et al., 2017).

Despite patient stratification based on molecular features, a major challenge of therapies involving blockade of cell signaling pathways in cancer cells is the high percentage of patients developing or harbouring resistance to treatment, resulting in no treatment response or a short duration of treatment. For instance, while the treatment of advanced melanoma patients with V600E or V600K BRAF mutation with the MEK inhibitor trametinib resulted in improved rates of progression-free and overall survival when compared to chemotherapy, the median progression-free survival was only 4.8 months for trametinib (and 1.5 months in the chemotherapy group), which were not long-lasting therapeutic benefits (K. T. Flaherty et al., 2012a).

Innate and acquired resistance to targeted treatment can have a variety of causes. For instance, a patient's tumor may harbour pathway-activating mutations downstream of the drug target, therefore rending the drug ineffective. Another reason could be the limited ability of the drug to bind to its target, for example due to poor tissue penetration (Trédan et al., 2007). Furthermore, inhibiting a molecule involved in cell signaling may not be sufficient to block signal transduction due to the complexity of cell signaling networks, which can involve negative feedback loops and activation of alternative signaling pathways (Carracedo et al., 2008; Phuchareon et al., 2015). This hypothesis is supported by the increased efficacy of therapies that combine multiple drugs, as discussed above.

Additionally, clinical trials that test novel inhibitors stratify patients based on a limited number (usually one) of mainly genetic predictive markers, such as mutational status or gene amplification, or protein-expression markers (McArthur et al., 2014; Murthy et al., 2014), potentially missing other important biomarkers crucial for treatment success. An additional problem of using genomic markers alone is that the genome only provides a

blueprint for proteins which, at best, allows a prediction of how cell signaling may be impaired, whereas signal transduction events are carried out by proteins – the functional units of the cell. Due to the increased complexity and dynamics of the proteome over the genome it is difficult to link a phenotype to the genotype, and discrepancies between the genome and proteome have been reported (L. Li et al., 2014; Mertins et al., 2016; B. Zhang et al., 2014). Factors contributing to the diversity of the proteome are alternative splicing events leading to isoform expression (Chen and Manley, 2009), cell-type and time-dependent expression patterns (Dove, 1999), subcellular localization, post-translational modifications (PTMs) such as phosphorylation, acetylation, ubiquitination, nitrosylation, sumoylation or oxidation, protein-protein interactions, varying turnover rates (Larance and Lomond, 2015), and a large cellular dynamic range of seven orders of magnitude in tissues (Zubarev, 2013). Additionally, proteins may be post-transcriptionally downregulated by the binding of miRNAs to mRNAs, thereby causing translational repression and degradation (Wilczynska and Bushell, 2015). For example, miR-21 has been shown to downregulate the tumor suppressors, programmed cell death protein 4 (Pdcd4) (Asangani et al., 2007) and phosphatase and tensin homolog (PTEN) (J.-g. Zhang et al., 2010). The regulatory complexity of gene expression and protein translation is likely responsible for the poor correlation of genomic, transcriptomic, and proteomic data, which suggests the need for integrated analysis of different -omics datasets to characterize tumors with higher confidence (Ciriello et al., 2013; Gygi et al., 1999; Teixidó et al., 2014).

Another factor contributing to low or no response to targeted therapeutics is intra- and inter-tumor heterogeneity (Blanco-Calvo et al., 2015; Fisher et al., 2013; Marusyk and Polyak, 2010). According to the trunk-branch model developed by Gerlinger et al., a cell population which initially has only one driver gene mutation leads to the emergence of sub-clones with specific additional passenger and driver mutations over time (Gerlinger et al., 2012), thereby increasing the probability of containing sub-populations within the tumor mass that are resistant to a specific therapy. Targeted treatments may therefore cause selection pressures in favor of these resistant sub-clones (Greaves and Maley, 2012). In addition to genetic mechanisms that lead to heterogeneity within tumors,

molecular mechanisms of generating non-genetic heterogeneity via the dynamic adaptation processes of signal transduction networks have been described as well (Kolch et al., 2015). Furthermore, interactions between tumors and their microenvironments have been linked to innate resistance to targeted anti-cancer drugs (Straussman et al., 2012).

Another important aspect to consider is that inhibitors targeting cancer cells have the potential to negatively affect the immune response, and thereby reduce the body's ability to fight cancer cells. For instance, Protein Kinase B (AKT) has been shown to be essential for differentiation of CD8+ T-cells into memory cells (Rogel et al., 2017). Thus, inhibition of AKT could interfere with long-lasting immunity.

1.3 Biomarkers to guide therapy

Clinical biomarkers are crucial for the concept of precision medicine. In general, a biomarker can be defined as a "characteristic that is objectively measured and evaluated as an indicator of normal biologic processes, pathogenic processes, or pharmacologic responses to a therapeutic intervention" (Atkinson et al., 2001). Additionally, biomarkers should exhibit a strong correlation with a particular disease or disease state to allow the differentiation between similar physiological states (Jain, 2010). Today, the term biomarker typically denotes "molecular biomarkers", rather than physical measurements such as body temperature. In the paradigm of precision cancer treatment, testing for molecular biomarkers, including mutation and expression analysis in signaling-pathway related genes, mRNAs, and proteins is increasingly used for diagnosis, treatment selection, therapy monitoring, assessment of drug safety and target engagement, prognosis, as well as during drug development as a companion diagnostic (de Gramont et al., 2015). For the sake of the patient, biofluids such as blood plasma or urine are sample sources preferred to more invasive sources, such as cerebrospinal fluid or tissue biopsies.

1.3.1 *Positive impact of biomarkers on drug development*

Drugs evaluated in clinical trials for various indications (including oncology, hematology, metabolic disorders, and more) that stratified patients based on selected genetic and protein biomarkers resulted in a 3-fold higher FDA approval rate (25.9%) compared to those that did not rely on biomarkers (8.4%), thus demonstrating the positive impact of biomarker-driven patient stratification (Biotechnology Innovation Organization, 2016). Importantly, however, of all the disease conditions evaluated, oncology drugs were the least likely to receive FDA approval, with an approval rate of only 5.1% (compared to 26.1% for the most likely group, hematology), indicating the need for more suitable cancer-related biomarkers.

Despite the positive impact of biomarkers on drug development and clinical trial outcomes, currently only a very limited number of targeted agents with demonstrated activity and an effective predictive biomarker are FDA-approved (Moy et al., 2007; U.S. Food and Drug Administration, 2015). In fact, only 16/167 FDA-approved oncology drugs are linked to companion diagnostic testing (Dracopoli and Boguski, 2017), possibly due to several considerations when combining drug development with companion diagnostics, including the added complexity of clinical-trial design, additional costs for development and implementation of the diagnostic assay, as well as an increased demand on patients to provide biopsies for the discovery and development of diagnostic tests. Nonetheless, these numbers show both the benefit of biomarkers and the fact that they are currently still underused.

1.3.2 *Biomarker discovery*

Historically, biomarkers were found as by-products of hypothesis-driven research related to elucidating disease mechanisms. However, over the past few decades, the advancement of powerful, high-throughput, and highly multiplexed technologies for the analysis of various types of molecules resulted in a transition towards discovery-based biomarker identification (McDermott et al., 2013). In these discovery studies, molecules are analyzed without prior assumptions, and research hypotheses are often generated in a

data-driven fashion after the analysis (Goossens et al., 2015). Furthermore, discovery experiments are mostly untargeted and fall into different "–omic" domains, including genomics, transcriptomics, metabolomics, and proteomics. To find new potential biomarkers, these approaches compare different conditions, such as healthy and unhealthy, for molecular differences.

The key techniques used in genomics and transcriptomics discovery efforts are DNA microarrays (Albertson and Pinkel, 2003) and next-generation sequencing (NGS) to detect alterations in the DNA sequence, such as single-nucleotide polymorphisms (SNPs) or rearrangements, as well as gene expression profiles (via RNA sequencing, RNA-seq) (Reis-Filho, 2009). NGS is very powerful in that it can be used for whole genome, whole-exome sequencing, splice variant analysis, and more, at a lower cost than the previous gold standard, Sanger sequencing, and at faster processing times due to highly paralleled analysis.

The search for novel protein biomarkers is typically performed by untargeted liquid chromatography-tandem mass spectrometry (LC-MS/MS)-based shotgun proteomics platforms which allow relative quantitation of protein expression (including PTMs) to assess different conditions for up- or down-regulated proteins on a global scale from single samples. Frequently-used quantitation techniques include label-free quantitation (Cox et al., 2014), chemical labeling such as isobaric tags for relative and absolute quantification (iTRAQ) (Mertins et al., 2012; Wiese et al., 2007), or metabolic labeling approaches such as stable isotope labeling in cell cultures (SILAC) (Ong et al., 2002). Shotgun proteomics experiments typically follow a bottom-up approach involving proteolytic digestion of proteins into peptides, followed by LC-separation and analysis on a mass spectrometer, in most cases an orbitrap mass analyzer (Aebersold and Mann, 2016). To increase the depth of analysis of PTMs, enrichment techniques have been developed to selectively enrich the sample in entire sub-proteomes such as the phosphoproteome (Fila and Honys, 2012). Data is commonly acquired in a data-dependent (DDA) fashion, which means that the mass spectrometer will record a full scan MS^1 mass spectrum, followed by selecting peaks based on pre-defined parameters, such as the ten most intense peaks, and fragmenting the molecules that correspond to the mass-

to-charge (*m/z*) ratios of the corresponding peaks. The fragment information is then recorded in an MS^2 mass spectrum. An example of shotgun proteomics applied to cancer research is the work of Atrih et al., who identified and quantified 1761 proteins from resected renal cell carcinoma and non-cancer renal tissues using a shotgun approach, and who found 596 of these to be differentially expressed between cancer and non-cancer tissues (A. Atrih et al., 2014). Another example is the work by De Marchi et al. who used an orbitrap-MS discovery approach to find a 4-protein signature predicting the outcome of tamoxifen treatment in recurrent breast cancer (De Marchi et al., 2016).

To discover clinically actionable biomarkers, and to decipher the molecular complexity involved in the development of cancer, over the past decade, large-scale collaborative efforts such as TCGA (Tomczak et al., 2015), CPTAC (M. J. Ellis et al., 2013), and the Therapeutically Applicable Research to Generate Effective Treatments (TARGET) initiative (Adamson et al., 2014) began to systematically determine the genomic, transcriptomic, and proteomic alterations of large sample cohorts of various tumor types, with the ultimate goal of creating catalogues of commonly dysregulated molecules. The data has been made publicly available to the research community to mine the data, generate and test hypotheses, and to follow up and validate the sub-sets of aberrations discovered on additional analytical platforms (Tomczak et al., 2015). An example of how TCGA data is being used is the study by Ciriello et al., who determined from 12 tumor types that mutations and copy number changes were the most frequent types of genetic alterations (Ciriello et al., 2013).

1.3.3 *Biomarker validation and clinical implementation*

Once potential biomarkers have been identified, the biomarker candidates are typically transferred to a clinically applicable assay platform, followed by analytical and clinical validation. This transfer is necessary because the techniques used for discovery work are less suitable as clinical assays for a variety of reasons. One obstacle is the difficulty of standardizing measurements between laboratories which can lead to reproducibility issues. Another problem is the fairly large sample amounts required for many discovery

experiments, in the range of >500 µg total protein per proteomic analysis (Sean J. Humphrey et al., 2015b). Also, discovery approaches require significant expertise and are too complex for routine clinical use. Additionally, proteomic shotgun experiments require extensive sample fractionation to reduce the complexity and maximize depth, making shotgun proteomics a low-throughput method, and therefore less ideal for verifying the biological meaning of potential biomarkers which requires the analysis of hundreds of samples (Boja and Rodriguez, 2012). It is therefore not surprising that, as of this writing, the majority of FDA-approved companion-diagnostic tests (38 out of 40) are based on non-discovery methodologies, including real-time polymerase chain reaction (RT-PCR), immunohistochemistry (IHC)/immunocytochemistry (ICC), and fluorescence/ chromogenic in-situ hybridization FISH/CISH assays. Only 2 of the 40 approved companion diagnostics were based on NGS, and -- currently -- none are based on MS analysis (U.S. Food and Drug Administration, 2018).

1.3.4 *Protein assay methodologies for clinical signaling pathway analysis*

The main clinical protein assay types are immunoassays such as enzyme-linked immunosorbent assay (ELISA) and IHC. While IHC provides spatial resolution, both IHC and ELISA immunoassays are well-established, easy to use, and are highly sensitive. In addition, they do not require complex instrumentation, and trained personnel can achieve high throughput due to parallelization (Cross and Hornshaw, 2016). However, these techniques heavily rely on the specificity of the antibody which has been shown to be problematic in a few scenarios. First, antigens may fail to recognize antigens due to unexpected or unknown PTM patterns. This has been shown with unexpected PD-L1 glycosylation patterns which interfered with the IHC-based quantitation, resulting in underestimated PD-L1 expression levels (Morales-Betanzos et al., 2017). Additionally, cross-reactivity of the antibody to non-target species can result in falsely elevated readouts. Furthermore, interferences by autoantibodies have been reported (Hoofnagle et al., 2008). Moreover, very high protein concentrations can result in a saturation effect, called the Hook effect, which results in falsely low antigen levels being determined. Due

to these issues, results using different assay platforms and between laboratories may differ (Rawlins and Roberts, 2004).

Two mass spectrometry-based methodologies which show great promise to overcome the drawbacks of immunoassays and IHC are multiple reaction monitoring (MRM) and immuno-matrix assisted laser desorption/ionization (iMALDI). Both techniques show great specificity due to the assignment of mass-to-charge (*m/z*) ratios to molecules, therefore overcoming any potential issues of non-specific antibodies.

MRM has become a powerful tool for quantifying proteins in biological and clinical samples in a targeted manner (Adonna et al., 2009; Kuzyk et al., 2009). Its high multiplexing capability of quantitating 10s to hundreds of proteins per run, its accuracy and precision due to the use of stable isotope-labeled standard (SIS) peptides with a linear response over several orders of magnitude, as well as its low sample consumption make this technique a promising tool for protein biomarker verification and validation purposes (Elliott et al., 2009; Parker et al., 2010). The reproducibility of this technology has been demonstrated in inter-laboratory studies, which indicate that -- with standardized procedures and reagents -- MRM results generated in different laboratories can be used for comparative analyses (Abbatiello et al., 2015; Adonna et al., 2009). In addition to analyzing unmodified proteins, MRM has been successfully used to target PTMs as well, including phosphorylation using Ti^{4+}- immobilized metal affinity chromatography (IMAC) enrichment (de Graaf et al., 2015) or glycosylation (Kim et al., 2012). Besides directly targeting the modified peptides, MRM has been coupled to approaches which use enzymes to *remove* specific PTMs, such as phosphatase approaches which allow the quantitation of phosphorylation stoichiometries (PS) (Domanski et al., 2010; R. H. Wu et al., 2011), or quantitation of glycan composition following enzymatic removal (H. Zhang et al., 2012). This is particularly useful for analyzing multiply modified peptides because their direct analysis would be challenging due to different *m/z* ratios, whereas removal of the PTMs results in a single mass to analyze. The disadvantage, however, is the loss of information regarding the exact sequence positions of the PTMs.

While MRM provides high sensitivity – typically low femtomole amounts of peptide on column -- this may not be high enough for low-abundance targets (Weiss et al., 2014). To

overcome this issue, two enrichment methods using anti-peptide antibodies have been developed, Stable Isotope Standards and Capture by Anti-Peptide Antibodies (SISCAPA) (Anderson et al., 2004), originally designed for use with extraction and electrospray LC-MS detection, and immuno-MALDI (iMALDI), developed by Dr. Borchers in 2003 and designed for MALDI detection without prior elution, as described in the following section (Raska et al., 2002; Raska et al., 2003). SISCAPA has also been shown to be suitable for the analysis for peptides carrying PTMs, such as phosphorylation (Whiteaker et al., 2015) or acetylation (Xu et al., 2015).

Although, once developed, LC-MRM assays are straightforward and can be standardized with partial automation of both the sample preparation and data analysis, clinical implementation as a routine protein analysis tool is challenging. Even with well-trained personnel the LC-MS system is not particularly robust compared to analytical systems such as photometric analyzers. Furthermore, even though multiplexing is a major advantage for MRM, sample throughput is low, especially when long LC gradients are used. However, this can be overcome by pre-enrichment of peptides prior to injection into the mass spectrometer and depends on the instrumentation, the number and nature of targets, and the complexity of the samples. A technology that holds the promise to overcome disadvantages of both currently used clinical technologies such as immunoassays and IHC, as well as potential clinical methods such as MRM, is iMALDI.

1.3.5 *Immuno-MALDI (iMALDI)*

iMALDI is a highly sensitive, targeted mass spectrometric (MS) technique for the quantitation of proteins on the peptide level. It combines the advantages of immunoassays with the specificity of MS by coupling affinity enrichment to MALDI time-of-flight (TOF) MS analysis. Due to its high sensitivity, the iMALDI technique is very suitable for the analysis of low-abundance targets which I hypothesized would make this methodology very suitable for the analysis of signaling-pathway activity. Furthermore, MALDI instrumentation is very robust with rapid acquisition times of only a few seconds per sample. Moreover, iMALDI can be performed on cost-effective

benchtop MALDI-TOF mass spectrometers such as the Bruker BioTyper, the Shimadzu AXIMA microorganism identification system, and the BioMerieux VITEK 2, which are already in clinical use for microbial identification and have been cleared by the FDA.

The iMALDI methodology was introduced by the Borchers lab more than 15 years ago (Raska et al., 2003; Warren et al., 2004), and has since been used in various applications, including the quantitation of epidermal growth factor receptor (EGFR) from breast tumor cell lysate and biopsy samples (Jian Jiang et al., 2007b), detection of *F. tularensis* spiked into buffer and human plasma (J. Jiang et al., 2007a), quantitation of Angiotensin I to determine plasma renin activity (PRA) (Camenzind et al., 2013; Reid et al., 2010) and multiplexed quantitation of Angiotensin I and II (Mason et al., 2012). Furthermore, a comparison of iMALDI and other affinity-MS techniques has been published recently (H. Li et al., 2017).

A general overview of the iMALDI workflow is shown in Figure 3. As in other bottom-up proteomics workflows, a protein sample such as cell lysate or blood plasma is digested by a suitable protease (e.g. trypsin), although this step is not necessary if the target analyte is an endogenous peptide. In the next step, a SIS peptide with identical sequence to the target peptide, but labeled with a heavy amino acid, is spiked into the sample as an internal standard at a known concentration. The physicochemical characteristics of the SIS peptide are the same as the endogenous (END) target peptide, but the SIS peptide signal can be differentiated from the endogenous peptide in the mass spectrum due to the incorporation of heavy isotopes (^{13}C, ^{15}N) in the SIS peptide. Anti-peptide antibodies coupled to magnetic beads are then added to enrich the target peptides. After enrichment, the bead-antibody-peptide complexes are washed and then directly spotted onto a MALDI target plate, *without* prior elution, thereby limiting loss of the analyte during the elution step. This is in contrast to SISCAPA, which elutes the peptides directly following the washing procedure, followed by injection into the mass spectrometer. Acidic MALDI matrix is then applied onto the dried spots. This leads to the elution of the target peptides and co-crystallization with the matrix molecules. Next, dried MALDI spots are subjected

to MALDI analysis. The resulting END-SIS signal intensity ratio then allows calculation of the endogenous peptide concentration.

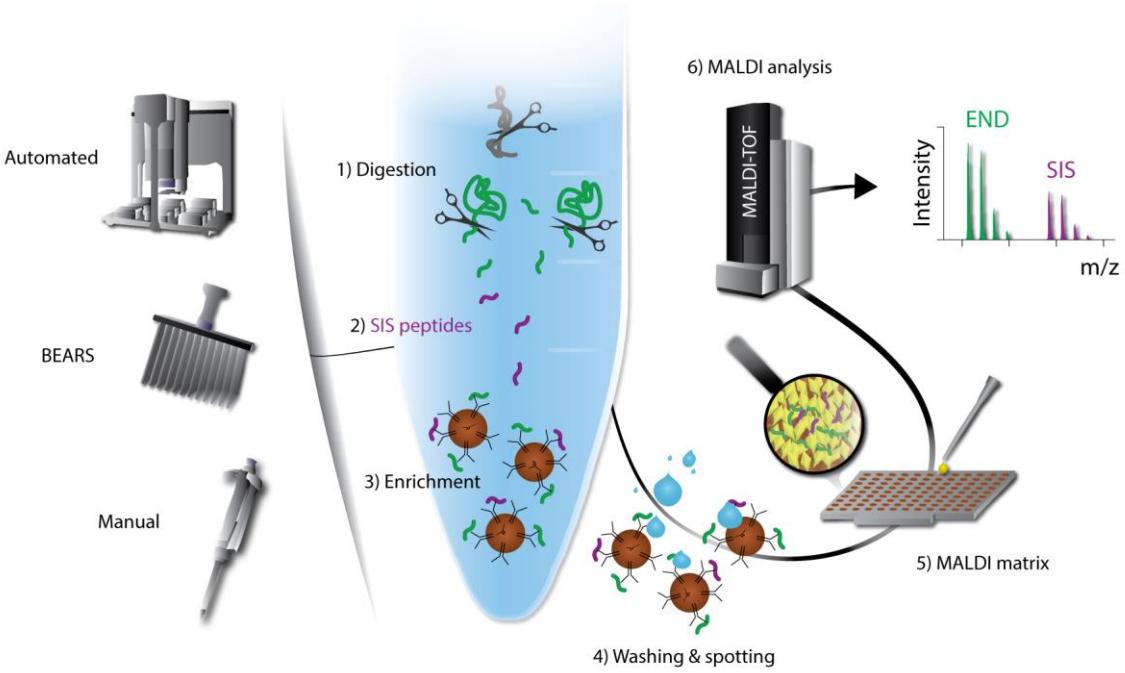

Figure 3: iMALDI workflow. 1) Proteolytic digestion. 2) Addition of SIS peptides. 3) Addition of antibody-coupled magnetic beads. 4) Washing and spotting of the washed bead-antibody-peptide complexes onto a MALDI plate. 5) Application of MALDI matrix. 6) MALDI analysis. END = endogenous peptide; SIS = stable isotope-labelled standard peptide; BEARS = Bead-Extractor Assisted Ready-to-Use Reagent System

1.3.6 *The PI3K/AKT/mTOR pathway*

The signaling pathway targeted in this thesis project is the PI3K/AKT/mTOR cell signaling pathway, a major regulator of organismal growth and survival in response to growth factors, hormones, cytokines and nutrients. It has been shown to be one of the most commonly dysregulated pathways in cancer (Ciriello et al., 2013; Engelman et al., 2006) and is therefore a key target for therapeutic inhibition (Fruman and Rommel, 2014). Several new inhibitors targeting members of this pathway are in clinical trials,

including PI3K, mechanistic target of rapamycin (mTOR), AKT, and dual PI3K/mTOR inhibitors (Polivka and Janku, 2014).

An overview of key regulatory proteins involved in this pathway is shown in Figure 4. The pathway is triggered by ligand binding to receptor tyrosine kinases (RTKs) or G protein-coupled receptors (GPCRs) followed by activation of the lipid kinase PI3K at the plasma membrane (Janku et al., 2018). Class IA PI3Ks are heterodimers consisting of a p85 regulatory domain and a catalytic domain (p110α, p110β, p110δ) and are activated by RTK molecules, whereas class IB PI3Ks consist of a p101 or p84 regulatory subunit and a p110γ catalytic domain and are activated by GPCRs (Engelman et al., 2006). Of the different PI3K isoforms, the *PIK3CA* gene encoding the p110α is most frequently altered in various cancers, including mutations in 26-41% of breast cancers and gene amplifications in 38-47% of squamous lung cancers, resulting in a gain of function (Janku et al., 2018).

Upon RTK-ligand binding, RTK molecules undergo a conformational change allowing homo- or heterodimerization with other RTK molecules. This dimerization leads to autophosphorylation of tyrosine residues on the intracellular kinase domain providing docking sites for signaling molecules or adaptor proteins. For instance, EGFR is directly recognized by class IA PI3K p85 regulatory subunits (Ullrich and Schlessinger, 1990), whereas other RTKs such as ErbB2/HER2 require the recruitment of adaptor proteins, e.g. GAB1 (GRB2-associated binder), which in turn allow binding of p85. Binding of the PI3K regulatory subunit then triggers activation of the associated catalytic domain.

In contrast to RTKs, GPCR-ligand binding results in the recruitment of the heterotrimeric G-protein complex (Gαβγ) to the GPCR, exchange of GDP for GTP at the Gα subunit, and release of the Gα and Gβγ subunits. The class IB PI3K regulatory domain (p84 or p101) directly binds to the GPCR Gβγ subunit, thereby activating p110γ-PI3K (Guillermet-Guibert et al., 2008). Other mechanisms of GPCR-related pathway activation involve RTK and integrin transactivation (Law et al., 2016; Walsh et al., 2008).

Upon activation of PI3K, the PI3K catalytic domain phosphorylates the 3'-hydroxyl group of the inositol ring of phosphatidylinositol-4,5-bisphosphate (PIP_2), thus generating phosphatidylinositol-3,4,5-trisphosphate (PIP_3), a second messenger lipid that recruits a

subset of pleckstrin homology (PH) domain containing cytosolic proteins to the plasma membrane, including AKT and 3-phosphoinositide-dependent protein kinase 1 (PDK1).

A major negative regulator of the conversion of PIP_2 to PIP_3 and frequently aberrated in many cancers is the phosphatase PTEN. Loss of function mutations in the *PTEN* gene has been found to occur at high rates in endometrial cancer (65%) and glioblastoma (31-41%) patients (Janku et al., 2018).

At the plasma membrane, PDK1, like AKT a member of the AGC kinase family, phosphorylates T308 in the activation loop of AKT leading to partial activation (Alessi et al., 1997). Additionally, mammalian target of rapamycin complex 2 (mTORC2) phosphorylates the conserved AKT residue S473 within a hydrophobic motif C-terminal to its kinase domain, resulting in full AKT kinase activation (Gao, 2014). Of note, the localization of mTORC2 at the plasma membrane has been shown to occur independent of PI3K or growth factors (Ebner et al., 2017).

Active AKT has more than 100 known substrates (B. D. Manning and Toker, 2017), and some of the most important ones will be discussed below. For instance, it directly phosphorylates the tuberous sclerosis protein 2 (TSC2) at residues S939, S1086/1088, T1422, and T1462 (Inoki et al., 2002; Brendan D. Manning et al., 2002). TSC2 is part of the TSC complex consisting of TSC1, TSC2 and Tre2-Bub2-Cdc16-1 domain family member 7 (TBC1D7) and contains a Rheb-GTPase activating protein (GAP) domain which is essential for inhibition of the small GTPase Rheb and mTORC1. Phosphorylation of TSC2 by AKT impairs the GAP activity of the TSC complex, allowing accumulation of the active form of Rheb, Rheb-GTP, which in turn activates mTORC1 at the lysosome. It was found that the phosphorylation of TSC2 does not affect the association between TSC1 and TSC2 (Brendan D. Manning et al., 2002), and that the GAP activity of TSC2 towards recombinant Rheb in vitro is not affected to a large extent (Cai et al., 2006). Instead it has been hypothesized that the scaffolding protein 14-3-3 binding to TSC2 phosphorylation sites could result in changes in its subcellular localization and/or disruption of its association with Rheb (Huang and Manning, 2009), thereby resulting in loss of the inhibitory effect of TSC2 on Rheb.

Another direct substrate of AKT is the BCL-2 family member BAD. Phosphorylation at S136 results in inhibition of apoptosis, thus promoting cell survival (Datta et al., 1997). Another major susbtrate of AKT is glycogen synthase kinase 3 (GSK3) which AKT phosphorylates at S21 (GSK3α) and S9 (GSK3β) resulting in inhibition of the kinase activity of GSK3 on its wide array of substrates (B. D. Manning and Toker, 2017). AKT further phosphorylates PRAS40, a negative regulator of mTORC1, at T246, resulting in activation of mTORC1 signaling (Kovacina et al., 2003).

Moreover, the factors FOXO1, FOXO3A and FOXO4, belonging to the family of Forkhead Box O (FoxO) transcription factors and impacting a diverse set of genes, get phosphorylated by AKT at distinct phosphorylation sites resulting in the generation of binding motifs for the 14-3-3 family of phospho-binding proteins, which facilitate the export from the nucleus into the cytosol (B. D. Manning and Toker, 2017).

At the lysosome, active Rheb allosterically binds to one of the components of mTORC1, mTOR, resulting in a conformational change and improvement in its catalytic function. The other two subunits of mTORC1 are mLST8 and RAPTOR, the latter of which is responsible for recruitment of mTORC1 to lysosomal membranes (Yang et al., 2017).

The activation of mTORC1 results in increased protein and lipid synthesis as well as increased autophagy which support cell growth and proliferation via the mTORC1 substrates eukaryotic translation initiation factor 4E (4E-BP1) and S6 kinase 1 (S6K1), both activated by RAPTOR recognizing Tor signaling sequence (TOS) motifs (Yang et al., 2017). To reduce the activity of the PI3K/AKT/mTOR pathway, active mTORC1 triggers a negative feedback loop resulting in a reduction in AKT activity.

Additionally, RTKs and GPCRs can activate RAS-RAF-MEK-ERK signaling, interlinked with PI3Ks via Ras-binding domains, where the adaptor proteins GRB2 and SOS mediate the signal transfer between RTK and Ras, and Ras activates PI3K (Egan et al., 1993). Similar to AKT, ERK has been shown to activate mTORC1 signaling via phosphorylation of TSC2, thereby allowing accumulation of active Rheb and activation of mTORC1 (Miyazaki and Takemasa, 2017).

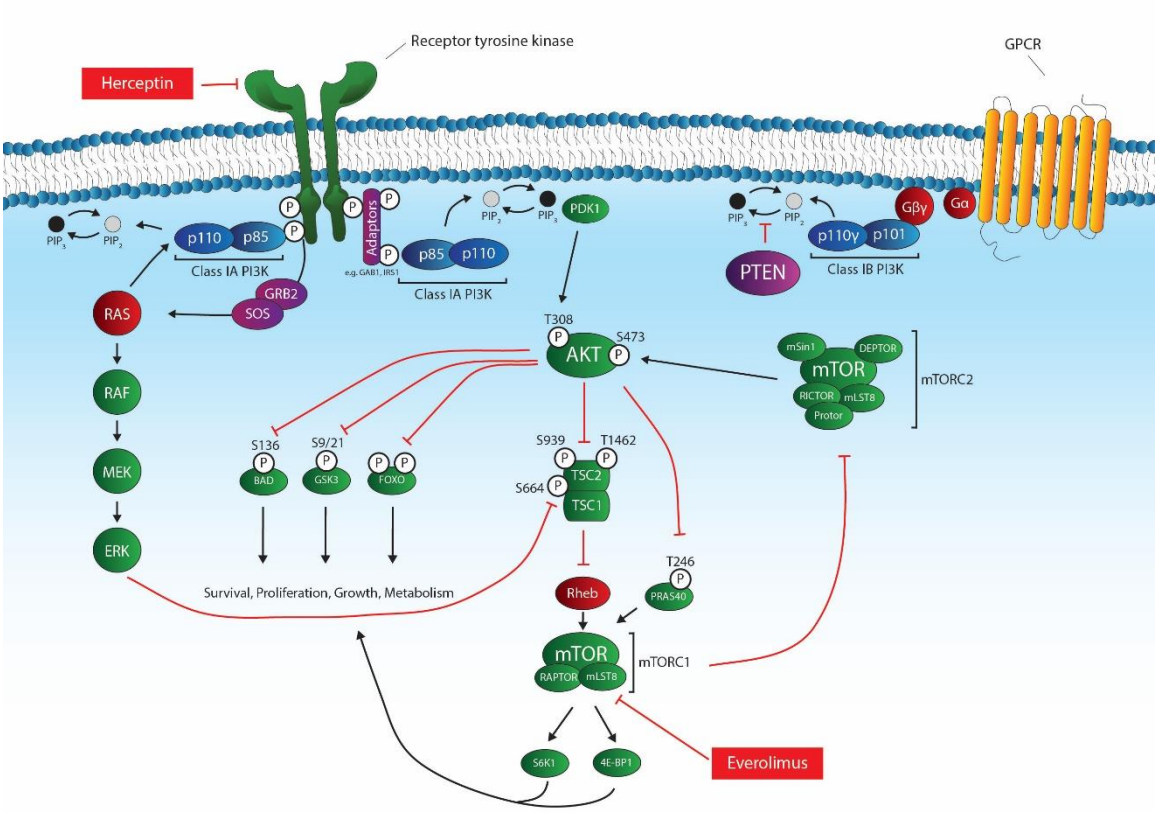

Figure 4: PI3K/AKT/mTOR signaling pathway. The pathway is initiated by ligands binding to RTKs or GPCRs. In the case of RTKs, class IA PI3K can bind either directly or via adaptor proteins such as GAB1 or IRS1, resulting in activation of its catalytic domain and conversion of PIP_2 to PIP_3. PIP_3 provides a docking site at the plasma membrane for PH domain containing proteins such as PDK1 and AKT. PDK1 phosphorylates AKT at the conserved residue T308, and mTORC2 phosphorylates AKT on residue S473. Active AKT phosphorylates a multitude of substrates, resulting in cell survival, proliferation, growth and increased metabolism. One of its downstream substrates is TSC2, which upon phosphorylation allows the formation of Rheb-GTP, thereby activating mTORC1. A closely related pathway is the RAS/RAF/MEK/ERK pathway, which is linked to the PI3K/AKT/mTOR pathway by the ability of Ras by binding to RTKs via the adaptor proteins GRB2 and SOS, followed by Ras-PI3K interaction.

1.3.7 *AKT*

In contrast to PI3K and PTEN, the serine/threonine kinase AKT, which consists of isoforms AKT1, AKT2, and AKT3, is rarely mutated in cancers (Janku et al., 2018). However, the kinase isoforms are of major interest due to their overexpression and over-activation in a variety of cancers (Cheng et al., 1996; Krześlak et al., 2011; Roy et al., 2002) and due their position downstream of PI3K and PTEN. Additionally, overactivated AKT isoforms have been associated with poor prognosis (Valkov et al., 2011; Zhu et al., 2015).

The AKT kinase is made up of the three isoforms which share approximately 80% amino acid sequence homology (Kumar and Madison, 2005) and which contain an N-terminal PH domain, a kinase domain, a linker region which connects the PH and kinase domains, and a C-terminal regulatory domain (Figure 5). The PH domain is responsible for binding to PIP_3 at the plasma membrane which results in alteration of the protein conformation, enabling the phosphorylation of key phosphorylation sites at T308, T309, and T305 in the kinase domain, as well as the C-terminal S473, S474, and S472 residues, which are part of the regulatory domain of AKT1, AKT2, and AK3, respectively (Fabi and Asselin, 2014). The C-terminal phosphorylation sites are crucial for full kinase activation. Recently, the phosphorylation sites S477/T479 in AKT1 and S478 in AKT2 have been implicated in kinase activation as well (Sean J. Humphrey et al., 2015b; Liu et al., 2014). Additionally, the conserved AKT1 Y176 residue (Y178 in AKT2) which is part of the catalytic domain has been shown to be phosphorylated by the non-tyrosine receptor kinase Ack1, resulting in translocation of AKT1/2 to the plasma membrane in a PIP_3-independent manner (Mahajan et al., 2010).

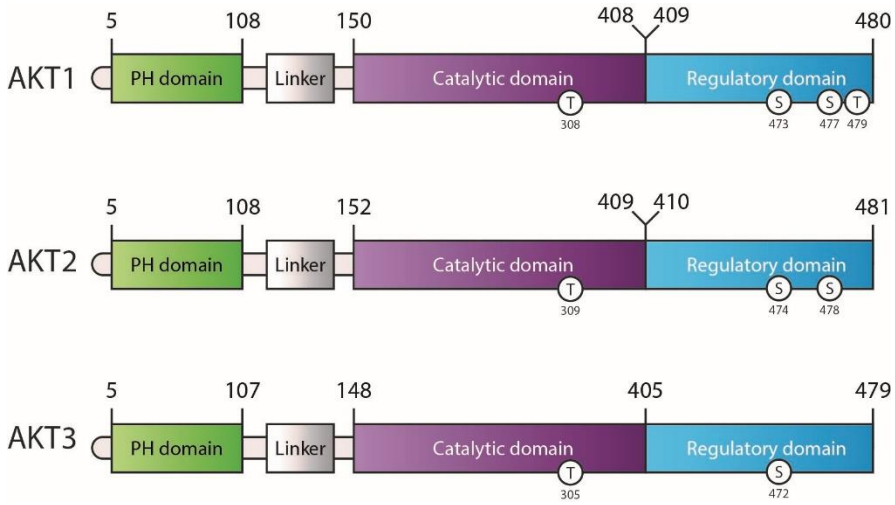

Figure 5: AKT isoforms with key phosphorylation sites and domain information obtained from the Uniprot database for isoform accession numbers P31749 (AKT1), P31751 (AKT2), and Q9Y243 (AKT3). The PH domain binds to PIP_3 at the plasma membrane.

The three isoforms have been shown to play non-redundant roles in lung cancer (Dobashi et al., 2015) and breast cancer (Riggio et al., 2017). Whereas AKT1 promotes cell proliferation through S6 and cyclin D1 upregulation, but inhibits cell migration and invasion through β1-integrin and focal adhesion kinase (FAK) downregulation, AKT2 was found to promote cell migration and invasion through the induction of F-actin and vimentin induction (Riggio et al., 2017). In the same study, Riggio et al. further determined that elevated AKT2 mRNA, but not AKT1 mRNA, was correlated with a worse prognosis for patients with invasive breast cancer. Additionally, the three isoforms were found to be localized in different cellular compartments (Santi and Lee, 2010), further suggesting specific roles for each isoform.

1.4 Research hypothesis and objectives

This thesis project assessed the hypothesis that there is a strong correlation between the PI3K/AKT/mTOR signaling-pathway activity, as measured by the phosphorylation status of key phosphorylation sites, and patient response to targeted treatment. To test this

hypothesis, the work presented here had two objectives: first, to develop and validate automated iMALDI assays to quantify the expression levels and PS of AKT1 and AKT2 from cancer tissues, and, second, to apply these assays to tissue samples of patient-derived mouse xenograft models extracted prior to and after drug treatment, and to correlate the pathway activity with the known outcomes.

The overall significance of this project was to develop a method to improve a patient's response to targeted therapies by more accurate patient pre-selection.

Chapter 2 focuses on the evaluation of iMALDI as a clinical tool. It shows that the iMALDI technique could be automated to generate sufficiently precise and high-throughput measurements to be of clinical utility.

In Chapter 3, the development and validation of the AKT1 and AKT2 iMALDI assays is presented.

In Chapter 4, the developed assays are applied to patient-derived mouse xenograft samples to test the project's hypothesis. The AKT1 and AKT2 iMALDI data obtained was compared to western blot and tumor size change data.

Finally, in Chapter 5, the limitations of the data and study as well as the future outlook are discussed.

Chapter 2: Evaluation of iMALDI as a clinical tool using the example of a plasma renin activity assay

Adapted from:

Popp, R. et al. An automated assay for the clinical measurement of plasma renin activity by immuno-MALDI (iMALDI). Biochimica et biophysica acta 1854, 547-558 (2015).

Contributions:

RP performed all of the iMALDI experiments and the data analysis, and wrote the manuscript. Grace van der Gugten performed all of the LC-MS/MS experiments.

2.1 Introduction

Routine diagnostic assays for various analytes are typically performed on high-throughput, highly robust photometric analyzers. To evaluate the suitability of the iMALDI approach for use in a clinical environment, a previously developed iMALDI assay for the determination of PRA (Camenzind et al., 2013; Reid et al., 2010) was chosen as an example.

PRA is a critical part of the aldosterone-renin ratio (ARR) which is used in screening patients for primary aldosteronism, a form of secondary hypertension (Funder et al., 2008). PRA assays quantify the rate at which renin, a member of the renin angiotensin aldosterone system (RAAS), converts angiotensinogen to angiotensin I (Ang I). In patients with primary aldosteronism, the RAAS is commonly dysregulated, resulting in low plasma renin activity. In the PRA assay, blood plasma is mixed with a suitable generation buffer that maintains a controlled pH (typically pH 6) to ensure consistent reaction kinetics, and which contains inhibitors such as ethylenediaminetetraacetic acid (EDTA) to prevent the angiotensin-converting enzyme (ACE) from further converting Ang I to Ang II. Camenzind et al. compared the fully manual iMALDI PRA assay to

clinically employed radioimmunoassay (RIA) and LC-MS/MS methods, and found excellent correlation with R^2 values of 0.94 and 0.95, respectively (Camenzind et al., 2013). To assess the potential of the iMALDI technique to be automated -- and therefore to allow high-throughput analysis with high precision and a minimum of human error -- prerequisites for clinical use -- the manual iMALDI PRA assay was automated, validated, and compared to a clinical LC-MS/MS method.

2.2 Materials and Methods

2.2.1 Chemicals, reagents and labware

Chemicals and reagents were obtained from Sigma Aldrich, Thermo Fisher Scientific, Fluka, and Roche Diagnostics. Protein G Dynabeads (2.8 µm) were purchased from Life Technologies. A commercially available anti-Ang I goat polyclonal antibody was purchased from Santa Cruz Biotechnologies (sc-7419).

2.2.2 Synthetic peptides

Light (NAT; DRVYIHPFHL) and stable isotope-labeled (SIS; DRVYIHPFHL) versions of Ang I were synthesized at the University of Victoria – Genome BC Proteomics Centre (Victoria, BC, Canada) using solid-phase peptide synthesis as previously described (Kuzyk et al., 2009). Both peptides differed by a mass of 10 Da (1295.7 and 1305.7 Da, respectively) due to incorporation of a heavy arginine (^{13}C, ^{15}N) in the SIS peptide. Accurate concentrations were determined by amino acid analysis (AAA), and purities of above 85% were found by capillary zone electrophoresis (CZE).

2.2.3 Plasma samples

Plasma samples from healthy control subjects were obtained from Bioreclamation (K2 EDTA plasma, Cat-#: HMPLEDTA2, pooled from five males and five females). Patient

plasma samples were selected from the routine primary aldosteronism screening program at St. Paul's Hospital, Vancouver. The plasma samples were collected in pre-chilled EDTA tubes, centrifuged at 4 °C, and frozen at -20 °C. Specimens were thawed for 5 min at room temperature (RT) and kept at 4 °C until fully thawed, followed by LC-MS/MS analysis. Samples were then refrozen and maintained at -80 °C until analyzed by iMALDI.

2.2.4 Automated iMALDI procedure

The following describes the iMALDI procedure automated on an Agilent Bravo liquid-handling robot for the analysis of 29 patient samples per batch. The procedure is based on the previously published iMALDI PRA comparison with RIA and LC-MS/MS (Camenzind et al., 2013), but with some newly-optimized parameters, such as a different generation buffer and modified Ang-I generation period to make the iMALDI method more comparable to the LC-MS/MS method. Furthermore, the calibration curve material was changed to chicken egg white albumin (CEWA) in 1×PBS, rather than 1×PBS/0.03% 3-[(3-Cholamidopropyl)dimethylammonio]-1-propanesulfonate (CHAPS), due to better automated liquid-handling performance.

Plasma and calibrator preparation

Plasma samples were thawed in a water bath at RT for five minutes and then immediately placed on ice until thawed. A 350-µL aliquot of each sample was transferred to a 1.1 mL deep-well plate and centrifuged for 10 min at 0 °C and 3000 × g. After centrifugation, a 350-µL aliquots of chicken egg-white albumin (CEWA)/1×PBS, used as the calibrator background material, were added to the same plate. In a next step, 250 µL of plasma supernatant and CEWA/1×PBS were mixed with 50 µL of Ang-I generation buffer (1M Tris/0.2 mM EDTA, 1 mM phenylmethane sulfonyl fluoride (PMSF), adjusted to pH 5.5 with acetic acid). The solutions were aliquoted into two new PCR plates, three replicates per plate, 34 µL per well.

Angiotensin I generation

One of the two plates was incubated at 37 °C for 3 hours to allow generation of Ang I due to endogenous renin activity. After the 3-hour incubation, the plate was placed on ice for 10 min to stop the renin activity. The second plate was stored at 4 °C for the entire 3 hours.

Antibody-bead coupling

Using a magnetic separator, Protein G Dynabeads were washed seven times with 25% acetonitrile (ACN)/ 75% [1× phosphate buffer saline + 0.015% CHAPS] (PBSC), and three times with PBSC to remove the Tween detergent present in the bead-storage buffer, which would interfere with the MALDI analysis. Afterwards, the anti-Ang I antibody and PBSC were added to the beads at a concentration of 0.2 µg antibody per 30 µg beads and incubated for 1 hour at RT while rotating at 8 rpm. Afterwards, the antibody-beads were washed three times with PBSC to remove any excess antibody, and were finally resuspended in PBSC.

Addition of peptide standards and enrichment

After the 3-hour Ang-I generation period, Ang I SIS peptide was added to each well as the internal standard (125 fmol per well). Then, Ang I NAT peptide was added to the CEWA/1×PBS wells at varying concentrations to create a calibration curve. Finally, 30 µg of beads carrying 0.2 µg anti-Ang I antibody were added to each well, and were incubated for 1 hour at 4 °C while rotating at 8 rpm.

Bead washing and spotting

After the 1-hour enrichment, the antibody-beads carrying the enriched target peptides were washed with three times with 70 µL of 25 mM ammonium bicarbonate buffer (AmBic), resuspended in 7 µL AmBic, and spotted onto four Bruker MSP BigAnchor 96 MALDI targets, arranged in a 384-well microtiter plate format. To arrange the four Bruker targets, which are 1/4 the size of a 384-well microtiter plate, a custom target holder was built. A USB-powered computer fan was used to facilitate the drying process.

Matrix spotting

After the beads were dry, 1 µL of an α-cyano-4-hydroxycinnamic acid (HCCA) MALDI matrix (containing 3 mg/mL HCCA, 1.8 mg/mL ammonium citrate, 70% ACN, and 0.1% TFA) was applied to each spot.

MALDI analysis

The MALDI spots were analyzed on a Bruker Microflex LRF instrument in both reflector and linear MALDI modes to identify the most suitable measurement mode. Bruker FlexControl 3.3 software was used to generate AutoXecute methods to automatically measure all spots. One thousand shots were summed for each spot, at a fixed laser intensity with matrix suppression set to 700 Da, 15 laser shots per raster spot, and a laser frequency of 60 Hz). The resulting mass spectra were analyzed using FlexAnalysis 3.4 scripts that performed automatic baseline subtraction, smoothing, and internal calibration based on the SIS peaks.

PRA calculation

The NAT/SIS intensity ratios of each mass spectrum were calculated. Next, a calibration curve was created from the calibrator samples, a forward linear regression curve was generated in Microsoft Excel, and this curve was used to convert the NAT/SIS ratios of

each sample to peptide concentrations. The sample PRA values were then calculated by quantifying the endogenous Ang I concentrations from each sample's 4 °C and 37 °C aliquots, which is the amount generated during the controlled 3-hour Ang I generation step at pH 6. This amount was then divided by the plasma volume (28.3 µL) and the 3-hour generation (10,800 seconds) according to the following equation:

$$PRA = \frac{Ang\ I\ generated}{Ang\ I\ generation\ period}\ in\ ng/L/s$$

2.2.5 iMALDI validation experiments

Linear range

The linear range of the automated iMALDI PRA assay was assessed by analyzing healthy human control plasma (n = 3) spiked with varying Ang I SIS peptide (4.9, 9.8, 19.5, 39.1, 78.1, 313, 625, 1250 and 2500 fmol/well) and constant Ang I NAT (125 fmol/well).

Precision testing

Intra- and interday precision testing was performed on low-, medium-, and high-PRA patient plasma pools. These were generated from plasma samples with known PRA values as determined by LC-MS/MS (provided by St. Paul's Hospital) and in accordance with pre-specified PRA ranges (Alderman et al., 2004). The pooled samples were aliquoted and stored at -80 °C until the day of analysis. Intraday precision was tested on five replicates of each PRA pool on one day. Interday precision was tested on one replicate of each plasma pool on five consecutive days.

Method comparison: iMALDI vs. LC-MS/MS for 188 patient samples

To compare my analytical results to a clinical method for PRA determination, the iMALDI assay was compared to the results of an LC-MS/MS assay performed at St. Paul's Hospital for 188 patient samples. Scatter and difference plots were generated with the free software cp-R for clinical laboratory method comparisons (Holmes, 2015).

Comparison of manual and automated sample preparation

The manual and automated iMALDI sample-preparation procedures were compared by preparing 13 replicates of healthy human control plasma and a calibration curve both manually and using the liquid handling system. The parameters assessed were processing time and analytical precision.

2.2.6 LC-MS/MS procedure

The LC-MS/MS procedure was performed as published elsewhere (Van der Gugten and Holmes, 2016).

2.3 Results and Discussion

2.3.1 iMALDI validation experiments

Linear range

The limit of detection (LOD) of the iMALDI PRA assay, which was defined as the lowest concentration that yielded an average signal-to-noise (S/N) ratio of 3, was determined to be 4.9 fmol/capture in the reflector mode, and 9.8 fmol/capture in the linear mode. Since 28.3 µL plasma and a 3-hour generation period were used, these concentrations correspond to PRA values of 0.02 ng/L/s and 0.04 ng/L/s.

Following the FDA guidelines for bioanalytical method validation (U.S. Food and Drug Administration, 2013), the linear range of the assay was determined using the following criteria: the lower limit of quantitation (LLOQ) was defined as the lowest concentration at which the variability of the replicates was <20%, with an intensity of at least 5 times that of the blank. To be within the linear range, all other points needed to show variability of <15%. In addition, the percent difference of the average SIS/NAT ratios was to be within ±20% at the LLOQ, and ±15% for the higher concentrations.

Using the above criteria, the linear range was determined to be 19.5–1250 fmol/capture (0.08 – 5.3 ng/L/s) in the reflector mode, and 9.8 – 1250 fmol/capture (0.04 – 5.3 ng/L/s) in the linear mode (Figure 6).

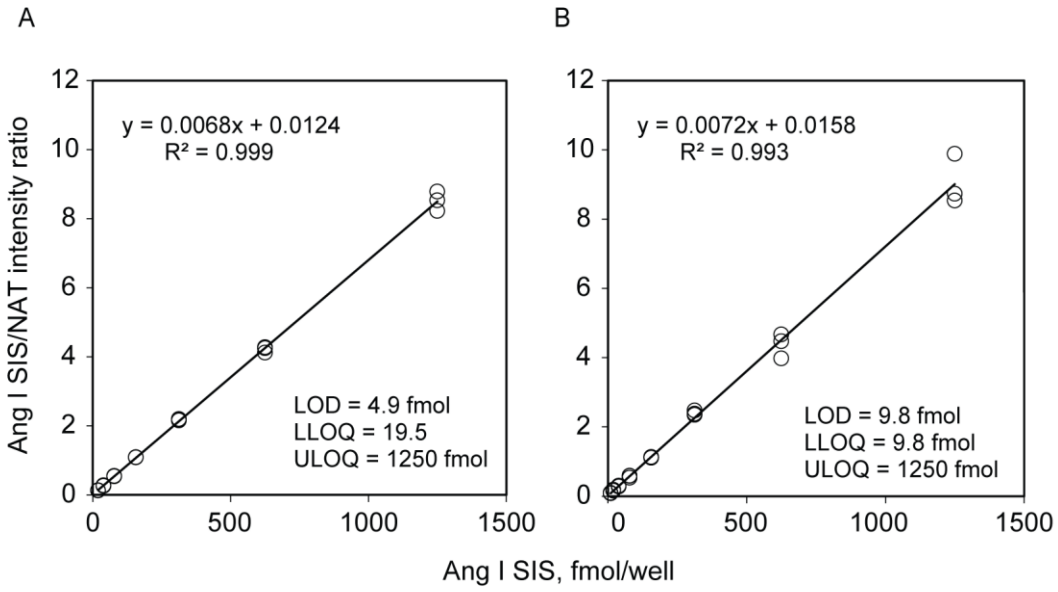

Figure 6: Linear ranges of the iMALDI PRA assay for the (A) reflector and (B) linear MALDI modes.

Thus, the linear mode allows quantification of slightly lower Ang I concentrations than the reflector mode. The sensitivity is suitable for clinical utility and comparable to published LC-MS/MS methods which achieve an LLOQ of 0.04 ng/L/s, with a 6.5 hour Ang I generation period (Carter et al., 2012). Furthermore, the iMALDI assay sensitivity

is higher than the established PRA cut-off value of 0.18 ng/L/s for low-PRA patients (Sealey et al., 2005), and is in agreement with the Endocrine Society's Clinical Practice Guidelines, which recommend a minimum sensitivity of 0.06 – 0.08 ng/L/s (Funder et al., 2008). Furthermore, the regression line slopes for the reflector and linear MALDI modes were very comparable, indicating similar response ratios for both measurement modes.

The linear ranges of both measurement modes allow accurate distinction between low - (<0.18 ng/L/s), medium- (0.18 – 1.25 ng/L/s) and high- (>1.25 ng/L/s) PRA patient samples (Alderman et al., 2004), and therefore cover the clinically relevant ranges of all PRA samples.

Precision testing

The precision of the PRA values determined for low-, medium- and high-PRA plasma pools is shown in Figure 7.

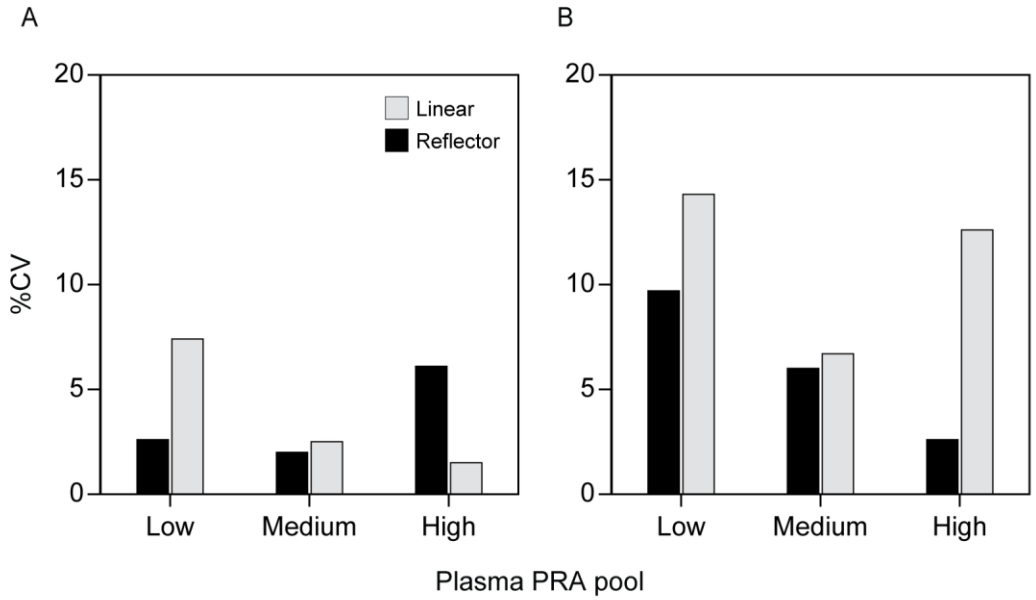

Figure 7: (A) Intraday and (B) interday precision testing on low-, medium-, and high-PRA plasma pools.

The intraday results (Figure 7A) showed CVs of <8% for the reflector mode, and <7% in linear mode, with CVs as low as 2.0 % in the reflector mode for the medium PRA pool, and 1.5% in the linear mode for the high PRA pool. As expected, the interday results (Figure 7A) were slightly higher than the intraday results. However, the reflector mode still showed CVs of ≤10%, and the linear mode resulted in CVs of ≤14%.

In conclusion, all of the CVs were below 15%, thus meeting the recommendations for clinical assays (U.S. Food and Drug Administration, 2013).

Method comparison: iMALDI vs. LC-MS/MS

To demonstrate that the iMALDI PRA assay yields comparable results to a clinically utilized PRA assay, iMALDI was directly compared to an LC-MS/MS procedure that is routinely used for patient screening at St. Paul's Hospital in Vancouver, by analyzing aliquots of the same 188 patient plasma samples (Figure 8).

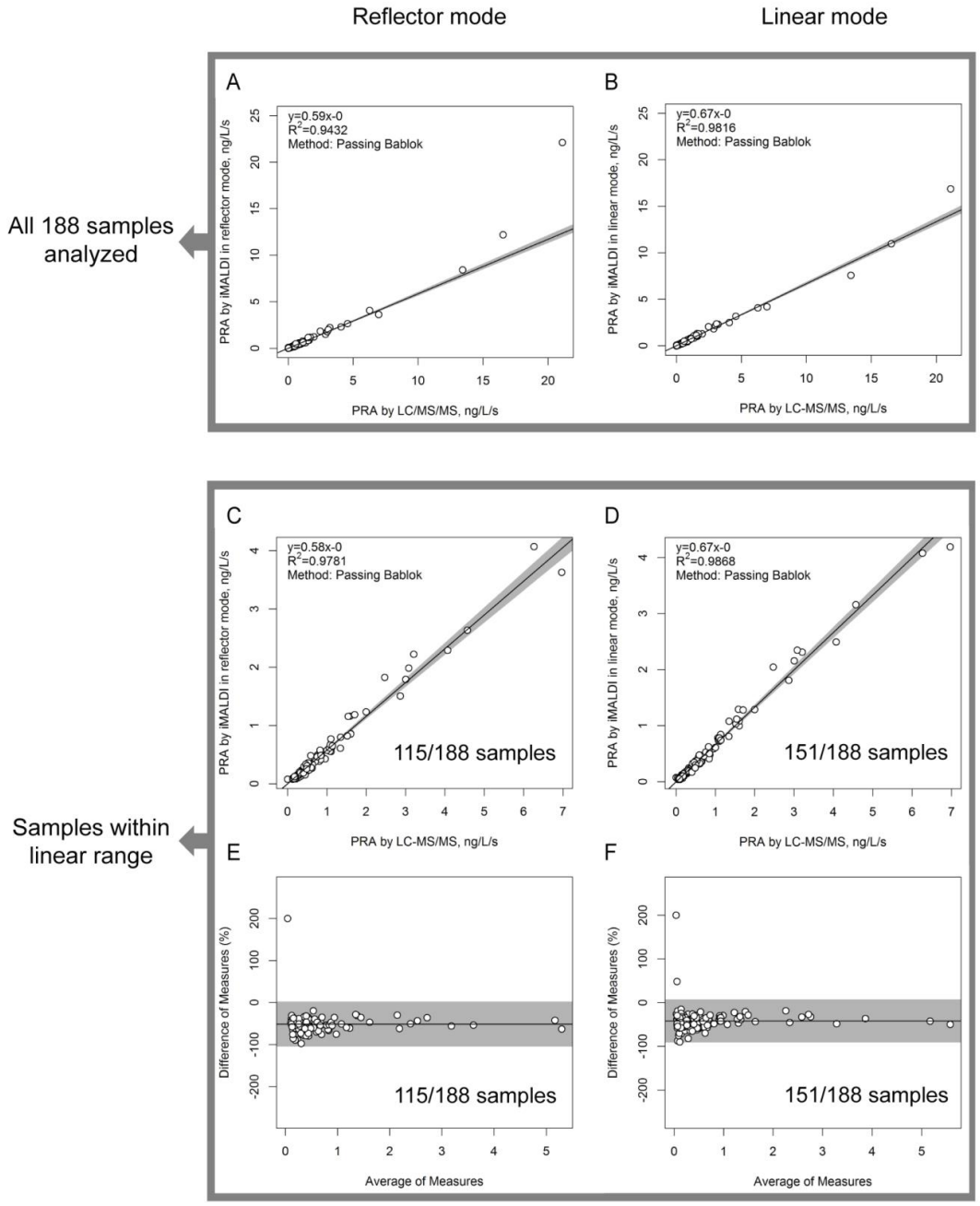

Figure 8: iMALDI vs. LC-MS/MS method comparison results of PRA values for 188 clinical patient samples. Passing Bablok regression results of all 188 patient samples measured in (A) reflector mode and (B) linear mode. Regression results of all samples within the linear range of the iMALDI PRA assay for (C) reflector mode and (D) linear mode. Difference plots for the samples within the linear range of the iMALDI PRA assay for (E) reflector mode and (F) linear mode.

Figure 8A and Figure 8B show the Passing Bablok regression results for all 188 patient samples measured in the reflector and linear MALDI modes, and Figure 8C and Figure 8D show the correlation results for all samples within the linear ranges for the reflector and linear MALDI modes. The R^2 values were 0.94 and 0.98, indicating excellent correlation between the iMALDI and LC-MS/MS assays. The slopes of 0.59 and 0.67, however, deviated from the expected slope of 1. Since the LC-MS/MS method runs quality control samples to ensure accurate results, these findings are most likely caused by a systematic calibration error of the iMALDI method. Another explanation could be that the two measurement techniques (iMALDI vs. LC-MS/MS) are two fundamentally different techniques, each with different means of analyte separation, and varying electronics such as detectors, which could lead to the observed systematic difference. This finding could be addressed by performing iMALDI accuracy studies in the future. Alternatively, a new reference range could be determined for the iMALDI assay, as is commonly done for laboratory developed tests (LDTs) for clinical use (Katayev et al., 2010).

Comparison of manual and automated sample preparation

To assess how the automated iMALDI sample preparation compares to the manual sample preparation in terms of precision and duration for each individual step, 13 plasma replicates and a calibration curve were prepared.

Figure 9 shows the PRA values and corresponding CVs. The automated and manual sample preparation, followed by analysis in the reflector (Figure 9A) and linear (Figure 9B) MALDI modes, resulted in comparable PRA values of approximately 0.23 - 0.26 ng/L/s. The automated sample preparation further resulted in comparable precision as the manual sample preparation with CVs of 3.0% and 2.8%, respectively. I therefore hypothesize that the minimally higher average PRA value with automated sample preparation (0.230 ng/L/s) compared to the manual sample preparation (0.256 ng/L/s) could be due to the calibration of pipettes used for manual liquid transfers being slightly different from the Agilent Bravo calibration. Analysis in the linear mode resulted in

slightly better precision for the automated sample preparation as compared to the manual sample preparation (CVs of 5.8% and 8.7%, respectively).

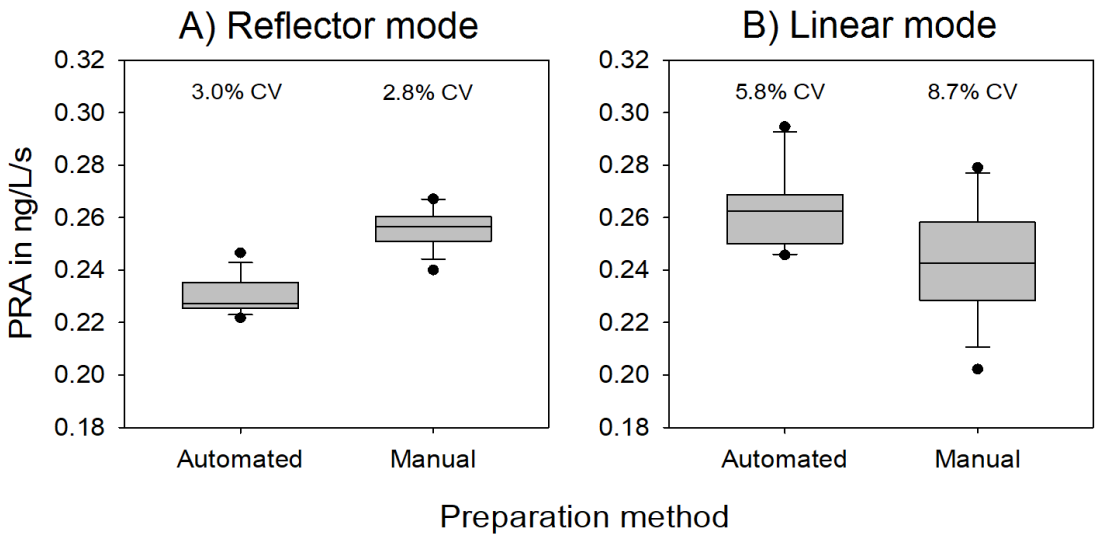

Figure 9: Comparison of automated and manual sample preparation for 13 replicates of generic human plasma by iMALDI in (A) reflector mode and (B) linear mode.

The manual and automated sample preparation was further compared for the steps “plasma preparation”, “bead and standard transfers”, “bead washing and spotting”, and “matrix spotting” (Figure 10). The automated sample preparation is significantly faster than the manual sample preparation for all steps and reduced the plasma preparation step from 11 min to 4 min, the bead and standard transfer step from 27 min to 12 min, the bead washing and spotting step from 46 min to 15 min, and the matrix spotting step from 22 min to 3 min. This increase in speed is especially important for longer steps such as the bead washing and spotting step, which is time sensitive due to the antibody-antigen kinetics, and matrix spotting, which requires much focus on the part of the technician and can lead to human error.

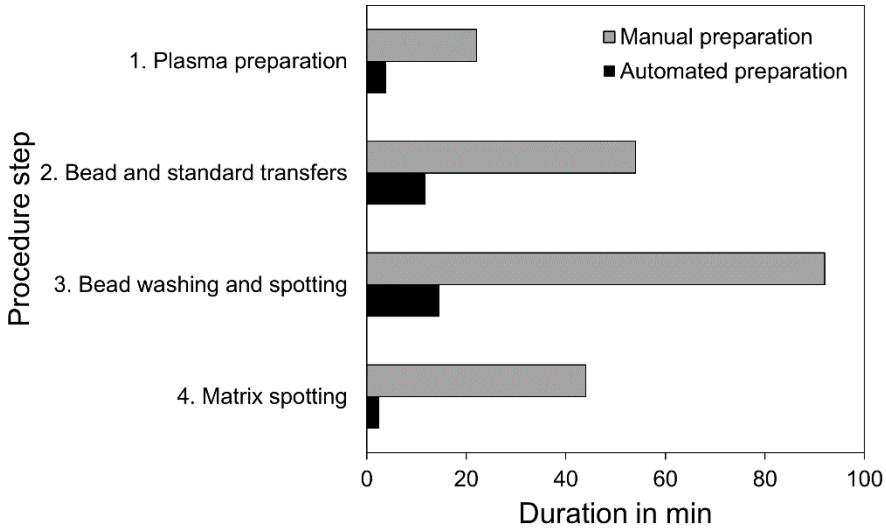

Figure 10: Comparison of manual and automated iMALDI sample preparation for the steps "plasma preparation", "bead and standard transfers", "bead washing and spotting", and "matrix spotting".

Throughput comparison

The sample preparation times for iMALDI and LC-MS/MS prior to MS analysis are very comparable. However, one of the big advantages of MALDI is the rapid analysis time per spot ranging from approximately 5 – 15 seconds, while LC-MS/MS methods typically require chromatographic separation of at least several minutes prior to injection into the mass spectrometer. In case of the LC-MS/MS PRA assay, a 6-min injection time per sample or calibrant was used (Van der Gugten and Holmes, 2016). This rapid analysis time shows the great potential of iMALDI as a high-throughput method for large-scale routine clinical analysis or for biomarker validation studies.

2.4 Conclusion

The results of this chapter demonstrate that all liquid handling steps of the iMALDI technique can be automated, which, like the manual sample preparation, results in excellent precision. However, the automation results in significantly faster sample preparation, less chance of human error, as well as significantly higher throughput. Taken together, these PRA assay results suggest that iMALDI is suitable for use as a clinical technique.

Chapter 3: Development and validation of iMALDI assays for quantifying the expression levels and phosphorylation stoichiometry of AKT1 and AKT2

Part of this chapter has already been published. This initial paper introduced the quantification of the AKT1 and AKT2 expression levels and included the analytical assay validation. A second paper is currently in preparation and will include the quantification of PS as well as comparisons of flash-frozen and FFPE samples, and validation of the methodology with matching normal and adjacent tumor tissue from the same tumors.

(1) Popp, R., Li, H., LeBlanc, A., et al. Immuno-MALDI (iMALDI) for quantifying AKT1 and AKT2 in breast and colorectal cancer cell lines and tumors. Analytical Chemistry 89, 10592-10600 (2017).

3.1 Introduction

After the demonstration in chapter 2 that iMALDI showed the characteristics of a methodology suitable for clinical use, my next goal was to expand its application to cell signaling pathway analysis in tumor tissues with the ultimate goal of answering the hypothesis whether there is a significant correlation between the PI3K/AKT/mTOR cell signaling pathway activity and tumor response to targeted treatment. To achieve this, the iMALDI approach was coupled to a phosphatase-based phosphopeptide quantitation approach (iMALDI-PPQ), which had been described before (Domanski et al., 2010).

I chose the PI3K/AKT/mTOR pathway due to it being one of the most commonly dysregulated cell signaling pathways in cancer (Fruman and Rommel, 2014). The initial assay development focussed on the following proteins as proxies for pathway activation: epidermal growth factor receptor (EGFR), vascular endothelial growth factor receptor 2 (VEGFR2), AKT1, and AKT2. However, due to difficulties in signal generation for EGFR and VEGFR2 -- due in part to unsuitable tryptic surrogate peptides for quantitation

-- this thesis work ultimately focussed on AKT1 and AKT2. While rarely mutated in cancer, these two homologues were of interest due to their position in the PI3K/AKT/mTOR pathway downstream of PI3K and PTEN, the two most commonly mutated proteins of this pathway in cancer (Ciriello et al., 2013), and due to the distinct roles of AKT1 and AKT2 in cancer development (Riggio et al., 2017). Specifically, I chose to target the C-terminal tryptic AKT1 and AKT2 peptides (^{466}RPHFPQFSYSASGTA^{480}, and ^{468}THFPQFSYSASIRE^{481}) due to their involvement in full kinase activation (Sean J. Humphrey et al., 2015b; Liu et al., 2014), their suitable size for MALDI analysis, and their lack of oxidizable amino acids.

The first part of this chapter is focused on assay development, including assessment of antibody performance, establishing key digestion parameters (such as finding a suitable denaturant that is compatible with iMALDI), digestion and dephosphorylation times, protease and phosphatase concentrations, as well as optimization of the sensitivity of the assay.

In a second step, the AKT1 and AKT2 assays were validated analytically, which included testing for linear range, accuracy, interferences, the impact of PS on digestion efficiency, and establishing a cut-off value for determining the PS based on measurement error.

Another objective was to compare the assay performance in flash-frozen and FFPE tissues. FFPE tissues were of particular interest due to their high prevalence in pathology (Magdeldin and Yamamoto, 2012), their use in companion diagnostic assays (Qiagen, 2012), the availability of clinical-outcome data in many cases, and therefore their enormous potential for use in retrospective studies.

Finally, the assays were evaluated for their suitability in detecting small differences in tissues. For this, normal tissues and adjacent tumor tissues were compared.

3.2 Materials and Methods

3.2.1 *Peptides*

Light peptides (NAT), singly stable isotope-labeled standard (SIS) peptides and doubly-isotope-labeled peptides (SIS^2) of the AKT1 (^{466}RPHFPQFSYSASGTA^{480}) and AKT2 (^{468}THFPQFSYSASIRE^{481}) sequences were synthesized at the University of Victoria – Genome BC Proteomics Centre (Victoria, BC, Canada) using solid-phase peptide synthesis, as previously described (Kuzyk et al., 2009), or ordered from SynPeptide (Beijing, China) and purified in-house upon arrival using high performance liquid chromatography (HPLC) (see Table 1). Experiments early in the assay development process showed that the AKT2 peptide was not cleaved at the R^{480} residue by trypsin (data not shown). The AKT1 and AKT2 SIS and SIS^2 peptides differ from the corresponding NAT peptides by 10 and 20 Da due to their incorporation of stable isotope-coded arginine and phenylalanine residues (^{13}C, ^{15}N). After synthesis and/or purification, the lyophilized peptides were resuspended in 30% ACN/0.1% formic acid (FA) and stored as stock solutions at -80 °C. The purities of the peptides were >86%, as determined by CZE. The peptide concentrations were determined by AAA.

In addition, “flanked” AKT1 and AKT2 peptides were ordered from SynPeptide (Beijing, China). These peptides were the tryptic C-terminal peptides, but extended on their N-terminus by 4 amino acids from the original protein sequence. NAT and SIS versions of these longer “winged” peptides, as well as NAT versions with singly phosphorylated serine and threonine residues, were generated. Each additional phosphoryl group resulted in a peptide mass increase of 80 Da.

Table 1: Overview of synthetic peptides generated for this thesis project. Bold, underlined R and F residues indicate heavy amino acids, and [pS] or [pT] indicate phosphorylated serine and threonine residues

Description	Peptide sequence	Monoisotopic mass of $[M+H]^+$	
		Monoisotopic	Average
AKT1 NAT	^{466}RPHFPQFSYSASGTA^{480}	1652.78	1653.77
AKT1 SIS	^{466}**R**PHFPQFSYSASGTA^{480}	1662.79	1663.78
AKT1 SIS^2	^{466}**R**PH**F**PQFSYSASGTA^{480}	1672.80	1673.79
AKT1 NAT (pS-473)	^{466}RPHFPQF[pS]YSASGTA^{480}	1732.75	1733.79
AKT1 SIS (pS-473)	^{466}**R**PHFPQF[pS]YSASGTA^{480}	1742.76	1743.71
AKT1 Flanked NAT	^{462}DSERRPHFPQFSYSASGTA^{480}	2139.98	2141.28
AKT1 Flanked SIS	^{462}DSER**R**PHFPQFSYSASGTA^{480}	2149.99	2151.21
AKT1 Flanked NAT (pS-473)	^{462}DSERRPHFPQF[pS]YSASGTA^{480}	2219.95	2221.26
AKT1 Flanked NAT (pS-474)	^{462}DSERRPHFPQFSY[pS]ASGTA^{480}	2219.95	2221.26
AKT1 Flanked NAT (pS-477)	^{462}DSERRPHFPQFSYSA[pS]GTA^{480}	2219.95	2221.26
AKT1 Flanked NAT (pT-479)	^{462}DSERRPHFPQFSYSASG[pT]A^{480}	2219.95	2221.26
AKT2 NAT	^{468}THFPQFSYSASIRE^{481}	1669.80	1670.83
AKT2 SIS	^{468}THFPQFSYSASI**R**E^{481}	1679.81	1680.76
AKT2 SIS^2	^{468}TH**F**PQFSYSASI**R**E^{481}	1689.81	1690.82
AKT2 NAT (pS-474)	^{468}THFPQF[pS]YSASIRE^{481}	1749.76	1750.81
AKT2 SIS (pS-474)	^{468}THFPQF[pS]YSASI**R**E^{481}	1759.77	1760.74
AKT2 Flanked NAT	^{464}LDQRTHFPQFSYSASIRE^{481}	2182.07	2183.40
AKT2 Flanked SIS	^{464}LDQRTHFPQFSYSASI**R**E^{481}	2192.08	2193.33
AKT2 Flanked NAT (pS-474)	^{464}LDQRTHFPQF[pS]YSASIRE^{481}	2262.03	2263.38
AKT2 Flanked NAT (pS-476)	^{464}LDQRTHFPQFSY[pS]ASIRE^{481}	2262.03	2263.38
AKT2 Flanked NAT (pS-478)	^{464}LDQRTHFPQFSYSA[pS]IRE^{481}	2262.03	2263.38

3.2.2 *Recombinant AKT1 and AKT2*

Recombinant full length human AKT1 (ab116412) and AKT2 (ab79798) were purchased from Abcam (Cambridge, UK).

3.2.3 *Antibodies*

Polyclonal rabbit anti-AKT1 and anti-AKT2 antibodies against the sequences CRPHFPQFSYSASGTA and CTHFPQFSYSASIR were generated by my collaborators at the Natural and Medical Sciences Institute (NMI, University of Tübingen, Germany), as described previously (Hoeppe et al., 2011).

3.2.4 *E. coli cells and cancer cell lines*

BL21 E. coli cells

BL21 *E. coli* cells were grown and provided by Karl Makepeace (a graduate student at the University of Victoria). The cells were grown overnight at 37 °C while shaking at 180 rpm, followed by pelleting and resuspension of the cells in PBS (pH 7.2).

SW480 cancer cells

SW480 human colon adenocarcinoma whole-cell lysate was purchased from Abcam (ab3957).

HCT116 colorectal cancer cells

HCT116 colorectal cancer cells were provided by Dr. Oliver Pötz of the Natural and Medical Sciences Institute (NMI) at the University of Tübingen, Germany. An aliquot containing $5x10^6$ cells of the HCT116 colorectal carcinoma cell line was plated in a 75-cm^2 cell culture flask (Greiner) and cultured in Dulbecco's Modified Eagle Medium (PAA Laboratories) supplemented with 2 mM glutamine (PAA Laboratories) and 10% fetal calf serum (PAA Laboratories), at 5% CO_2 atmosphere and at 37 °C. When the cells reached a density of 70%, they were rinsed with pre-chilled PBS. Cells were harvested using a rubber policeman and pelleted at 500 × g and 4 °C.

MDA-MB-231 breast cancer cell lysates

The MDA-MB-231 breast cancer cell lysates were provided by Dr. Adriana Aguilar-Mahecha from the Jewish General Hospital (JGH), Montreal. MDA-MB-231 were obtained from the American Type Culture Collection (ATCC) and grown at the JGH, Montreal, in 10% Roswell Park Memorial Institute (RPMI) media in the presence of 5% CO_2 at 37 °C. Cells were starved overnight and cultured in the presence of 0.25% fetal bovine serum (FBS). The next day, cells were incubated with 10 ng/mL human recombinant EGF (Invitrogen) in 0.25% FBS for 10 min at 37 °C. Cells were harvested at 80% confluence for protein extraction.

3.2.5 *Flash frozen and FFPE tissues*

All tissue samples (flash frozen tissue lysates and FFPE cores) were provided by Dr. Adriana Aguilera-Mahecha of the JGH.

Tissue quality assessment

All tissues -- as haemotoxylin and eosin (H&E) slides -- were assessed by a pathologist at the JGH to determine tumor cellularity, necrosis and boundaries of tumor and normal tissues (see Appendix Table 1 and Appendix Figure 1). Total pAKT expression was confirmed by IHC.

Flash frozen tissues

Primary surgical and biopsy breast-tumor samples were obtained from the JGH breast-cancer tissue repository. Colorectal liver metastasis tissues were provided by the JGH as well. Patients consented to the collection and use of their samples for research purposes (Ethics protocol 05-006).

HCT116 mouse-tumor xenografts were generated by implanting 1×10^6 HCT116 colorectal cancer cells into the flanks of immuno-compromised BALB/C nude mice (Charles River). After tumor growth, the tumor tissue was collected and flash frozen.

Frozen tumor tissues were transferred to a pre-chilled 10-cm plate and protein extraction was performed. The tissues were homogenized using the Precellys® Evolution at 4500 - 5500 rpm for 10 - 20 seconds.

FFPE cores

After pathology assessment, tumor cores were extracted from the FFPE blocks matching the flash-frozen tissues. Additionally, cores of adjacent normal tissue were extracted. The cores were shipped to Victoria at room temperature, followed by lysate preparation as described below.

3.2.6 *Protein extraction from tissues*

Flash-frozen tissues

The following describes the cell-lysis protocol used for cell lines and flash-frozen tissues. I extracted proteins from the HCT116 cell line and the *E. coli* cells. Flash-frozen tissues and MDA-MB-231 cells were lysed by Cathy Lan at the JGH, and the lysates were shipped frozen to Victoria.

The cell-containing media was transferred to a centrifuge tube, followed by centrifugation at 4 °C for 5 min at 2,348 × g. The resulting pellet was washed three times with 2 mL cold 1×PBS. In between washes, the cells were centrifuged at 4 °C for 1 min at 13,523 × g. After the last wash, 300 µL of ice-cold T-PER tissue-protein extraction reagent (Thermo Fisher Scientific, Catalog number: 78510), containing 1× Halt phosphatase inhibitor (Catalog number: 78428) and 1× Halt protease inhibitor (Catalog number: 78430). Cell lysis was performed by sonication with 10 short pulses of 1 second/pulse. The lysate was placed on ice for 30 seconds, and the sonication step was repeated two more times. The tube was then centrifuged for 5 min at 4 °C at 9,391 × g.

The supernatant was split into two new microfuge tubes, of which one contained 50 µL for bicinchoninic acid (BCA) analysis. Both tubes were stored at -80 °C until analysis.

FFPE tissue cores

FFPE tumor and adjacent normal tissue cores of approximately 1×5 mm in size were extracted from FFPE blocks and stored at room temperature. Deparaffinization and rehydration was performed by RP as described by (Becker and Schott, 2011), with the exception that xylene substitute (Sigma Aldrich, A5597) was used instead of xylene. Mortar and pestle were used during the deparaffinization and rehydration steps to homogenize the tissues. Following deparaffinization and rehydration, proteins were extracted by pipetting 150 µL of extraction buffer [50 mM TrisHCl, pH 8.1, 2% sodium deoxycholate (DOC; w/V), 10 mM TCEP, 1× Halt protease, and phosphatase inhibitor] to the pellets, and mixed by vortexing. Tubes were incubated on ice for 5 min, followed by incubation on a Thermomixer at 99 °C for 20 min at 500 rpm, and subsequent incubation at 80 °C for 2h at 750 rpm. After the incubation, the tubes were placed on ice for 1 min, and then centrifuged for 15 min at 14,000 × g at 4 °C. The supernatant containing the extracted proteins was transferred to a new 1.5-mL microfuge tube and stored at -80 °C until analysis.

3.2.7 *Total protein quantitation*

Protein concentrations of cell and tissue lysates were determined by reducing agent-compatible BCA assay, following the manufacturer's protocol (Thermo Fisher Scientific, 23250).

3.2.8 *General iMALDI-PPQ workflow*

The following describes the general workflow for the quantitation of expression levels and PS of target proteins based on proteotypic peptides from cell lysates using a combination of iMALDI and a phosphatase-based phosphopeptide quantitation (PPQ) approach (Domanski et al., 2010).

In the first step of the PPQ protocol, cell lysate proteins were digested using a suitable protease, such as trypsin, followed by the addition of non-phosphorylated SIS versions of the target peptides at known concentrations. Next, the sample was split into two aliquots, of which one was treated with phosphatase to remove any peptide phosphoryl groups. Afterwards, antibodies specific for the non-phosphorylated target peptides and coupled to magnetic beads were added for peptide enrichment. Next, the bead-antibody-peptide complexes were washed and directly spotted onto a MALDI target plate. After the spots were dry, an acidic HCCA-MALDI matrix was added to elute the peptides from the antibody-beads. The peptides co-crystallize with the matrix molecules. MALDI analysis results in NAT/SIS intensity ratios which were used to quantify the non-phosphorylated target peptides in both sample aliquots (with and without phosphatase treatment). The difference between these two quantities were then used to calculate the PS of the target peptides.

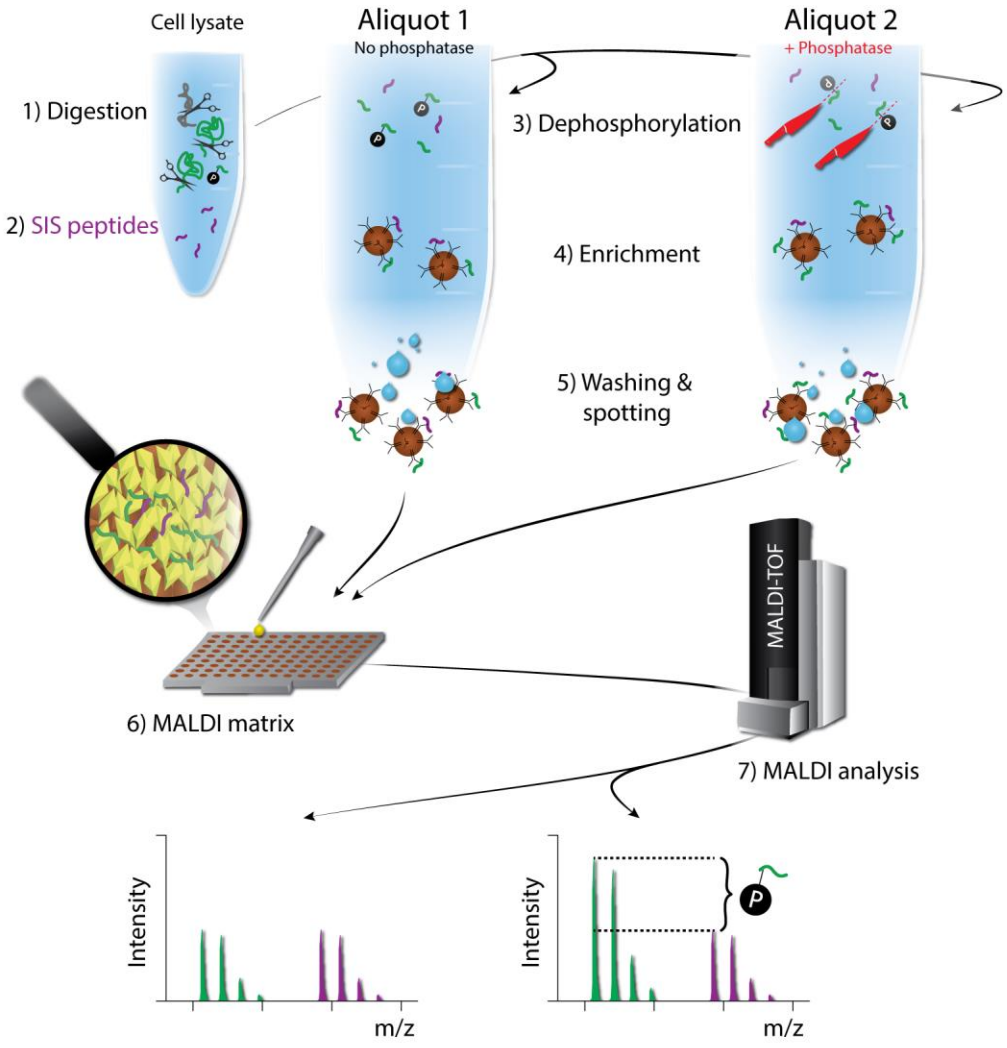

Figure 11: Schematic representation of the iMALDI-PPQ workflow. (1) Digestion of cell lysate with a protease such as trypsin. (2) Addition of SIS peptides. (3) Splitting of digested sample into two aliquots. Alkaline phosphatase is spiked into one aliquot (P+) to dephosphorylate all peptides. The second aliquot does not receive any phosphatase (P-). (4) Enrichment of the non-phosphorylated target peptides by antibodies coupled to magnetic beads. (5) Washing of bead-antibody-peptide complexes and spotting of the beads onto a MALDI target plate. (6) Addition of acidic MALDI matrix to the dry spots elutes the peptides and allows co-crystallization with the matrix molecules. (7) MALDI analysis and data evaluation.

3.2.9 *Automated optimized iMALDI-PPQ workflow for AKT1 and AKT2*

The automated iMALDI-PPQ workflow evolved over the duration of this thesis project and I changed various parameters based on new findings. For simplicity, the following describes the optimized, final, automated iMALDI-PPQ workflow. Experiments that used parameters different from this workflow will have those changes stated in the corresponding method sections. All major liquid-handling steps were automated on an Agilent Bravo liquid-handling robot, equipped with 96-channel LT head, a gripper designed for gripping microtiter plates, a 96-chimney tip wash station and an Agilent orbital shaking station. The assay layout allows the quantitation of expression levels and PS of AKT1 and AKT2 for 24 samples per batch.

Digestion

Cell line or tissue lysates (up to 24) and *E. coli* cell lysate (used as matrix for the calibration curve) were thawed on ice and diluted with sample-dilution buffer (20 mM TrisHCl, pH 8.1, 0.015% CHAPS) to a concentration of 0.1 µg/µL. Next, 450 µL of diluted sample and *E. coli* lysates were transferred to a deep-well plate (the Sample Source Plate). The Agilent Bravo was then used to aliquot 100 µL of each diluted sample and *E. coli* lysate into two new deep well plates (Sample Digestion Plate, Calibration Plate), resulting in 10 µg total protein per well. Next, 10 µL of denaturation mix [10% sodium deoxycholate, 200 mM TrisHCl, pH 8.1, and 0.74 mM tris(2-carboxyethyl)phosphine (TCEP)] were added to each well and the plates were incubated at 60 °C for 30 min. Afterwards, the plates were cooled to RT for 10 min. Next, 10 µL of 0.74 mM iodoacetamide (IAA) were added to each well and the plates were incubated at RT in the dark for 30 min. In the next step, 10 µL of 0.74 mM dithiothreitol (DTT) were added to each sample and incubated for 1 min at RT. Next, 10 µL of 2 µg/µL trypsin solution, prepared in 1 mM HCl, was added to each well and incubated at 37 °C for 60 min. Afterwards, the plates were placed on ice for 10 min, followed by the addition of 10 µL of 0.06 µg/µL Tosyl-L-lysyl-chloromethane hydrochloride (TLCK; prepared in 1 mM HCl), and incubated for 1 min at RT.

Addition of NAT and SIS standards

AKT1 and AKT2 NAT and SIS standard peptides were prepared by diluting the 10 pmol/µL stock solutions with Tris-buffered saline/CHAPS (TBSC: 200 mM TrisHCl, pH 8.1, 140 mM NaCl, 0.015% CHAPS). The diluted standards were stored at -20 °C and thawed on ice on the day of analysis.

After digestion, the samples were spiked with either 10 µL AKT1 or AKT2 SIS standards, resulting in 2 fmol SIS peptide/well.

A 10-µL aliquot of the AKT1 or AKT2 SIS standard (2 fmol/well), and 10 µL of the AKT1 or the AKT2 NAT standard was added to the *E. coli* wells,, resulting in 0.3, 0.6, 1.3, 2.5, 5, 10, and 20 fmol NAT peptides per well.

Dephosphorylation

Next, 10 µL of alkaline phosphatase, diluted with TBSC to a concentration of 2 U/µL, was added to half of the digested AKT1 and half of the digested AKT2 sample aliquots. The sample plate was then incubated for 2 hours at 37 °C. After the dephosphorylation step, the plate was placed on ice for 10 minutes.

Preparation of magnetic beads

Using a magnetic separator, Protein G Dynabeads were washed 7 times with 25% ACN/PBSC, and 3 times with PBSC, followed by addition of PBSC and either anti-AKT1 or anti-AKT2 antibodies at a ratio of 0.2 µg antibody per 30 µg beads. The extensive washing of the beads was necessary to remove the Tween detergent which was in the bead storage buffer and which would otherwise interfere with the MALDI analysis. The beads and antibodies were incubated for 1 hour at RT while rotating at 8 rpm. Afterwards, the antibody-beads were washed three times with PBSC and resuspended to give a solution containing 0.2 µg antibody linked to 30 µg beads per 10 µL PBSC.

Peptide enrichment

Next, 10 µL of resuspended magnetic beads coupled to anti-AKT1 or anti-AKT2 antibodies were added to the calibrator and sample wells, followed by incubation of the two plates at RT for 1 hour while shaking at 1200 rpm. Each well contained 30 µg of beads linked to 0.2 µg of antibody.

Bead washing and spotting onto MALDI plates

The bead washing procedure required three different wash buffers, which were aliquoted by the Bravo into the four 96-well quadrants of a 384-well microplate (Greiner) from the reservoir plates (Axygen Scientific): (1) 15% ACN/PBSC, (2) 15% ACN/5 mM ammonium bicarbonate (AmBic), and (3) 5 mM AmBic. After the affinity-enrichment step, the digest plate was placed on the Bravo, to which two types of magnets had been added: a DynaMag-96 side-skirted magnet, which pull the beads to the well sides, and a VP771 rpm magnet (VP Scientific), which pulls the beads to the bottom of a PCR (Eppendorf) plate. During this procedure, the sample solution was discarded and the beads were washed in the 1.1-mL deep-well plate with 100 µL of wash buffer, starting with one wash of 15% ACN/PBSC and a second wash with 15% ACN/5 mM aqueous AmBic (v:v); the orbital shaker was used for resuspending the beads. After a third wash, this time with 15% ACN/5 mM aqueous AmBic (v:v), the beads were resuspended and transferred to a new 150 µL PCR plate. This allowed resuspension of the magnetic beads in a low volume (10 µL) of 5 mM AmBic prior to spotting the beads onto the MALDI plate. The 10-µL volume was required for successful resuspension of the magnetic beads, and this step could not be performed in a 1.1 mL deep-well plate due to the shape and size of the wells. The beads were then spotted onto four disposable 96-spot µFocus Microflex MALDI plates (Hudson Surface Technology), using a custom-made plate adapter (Milroy Engineering Ltd., Victoria, BC) which allowed the four MALDI plates to be arranged in a microplate format. A small USB-powered fan was used to facilitate drying of the MALDI spots.

Application of MALDI matrix and washing of MALDI spots

After the MALDI spots were dry, the Agilent Bravo was used to transfer 1.5 μL of the HCCA MALDI matrix solution [3 mg/mL HCCA, 1.8 mg/mL ammonium citrate, 70% ACN, and 0.1% aqueous trifluoroacetic acid (TFA), prepared in a glass vial] from a 500-μL 96-deep-well plate (Axygen Scientific) to each sample spot. The acidic pH of the matrix solution eluted the peptides from the antibody beads, followed by co-crystallization of the peptides with the matrix molecules. After the matrix solution was dry, the Bravo was used to wash each sample spot for a total of three washes with 6 μL of 7 mM ammonium citrate. After each wash, 0.2 μL of wash buffer remained on each spot, which was allowed to dry prior to the next wash.

MALDI-TOF Analysis

MALDI-TOF analysis was performed on a Bruker Microflex LRF mass spectrometer. The μFocus MALDI plates were placed on a Microflex holder manufactured by Hudson Surface Technology. One mass spectrum per spot was acquired by summing 1000 shots in either the positive-ion linear mode or the positive-ion reflector mode, using a fixed laser intensity and a "random walk" pattern with 15 shots at each raster spot. The ion-suppression acquisition parameter was set to 1250 Da. The AutoXecute methods were generated in the Bruker FlexControl 3.3 software to automatically acquire data from the MALDI plates. After acquisition of the raw data, a FlexAnalysis 3.4 script was used for automatic smoothing, baseline subtraction, and internal calibration based on the SIS peaks. Mass spectra acquired in the reflector mode were internally calibrated using their monoisotopic mass-to-charge (*m/z*) values, while mass spectra obtained in the linear mode were calibrated by using the average *m/z* values because of the increased peak width which encompassed the entire isotopic envelope.

3.2.10 *Evaluation of the anti-AKT1 and anti-AKT2 peptide antibodies*

To assess the functionality of the anti-AKT1 and anti-AKT2 peptide antibodies, 50 fmol of AKT1 and AKT2 NAT and SIS peptides were captured from PBSC buffer, followed by MALDI analysis. Next, recombinant AKT1 and AKT2 proteins were digested overnight at a total protein:trypsin ratio of 20:1 in PBSC and 100 µg *E. coli* lysate protein per replicate, followed by iMALDI analysis.

3.2.11 *Optimization of the digestion conditions*

Denaturant

To find a denaturant compatible with the iMALDI workflow, urea, guanidine hydrochloride (GnHCl), sodium dodecyl sulphate (SDS), and DOC were compared. For this, AKT1 NAT peptide (500 fmol/well) was spiked into chicken egg white albumin in 1×PBS (CEWA/PBS) and pooled human plasma, followed by denaturation at room temperature with 7.2M urea, 5.3M GnHCl, 0.1% SDS, and 5% DOC for 5 min. The samples were then diluted with 25 mM AmBic to lower the denaturant concentrations, followed by reduction with TCEP, alkylation with IAA, addition of DTT to quench any residual IAA, and digested with trypsin overnight at 37 ºC. The denaturant concentrations at the point of digestion were 0.72M, 0.97M, 0.03%, and 1.13% for urea, GnHCl, SDS, and DOC, respectively, to ensure proper digestion and antibody-peptide binding. After the digestion, AKT1 SIS peptide (250 fmol/well) was added to each digested sample. The target peptides were enriched with anti-AKT1 antibody beads for 1 hour at room temperature, followed by washing and spotting of the beads onto a MALDI plate, and MALDI analysis.

Digestion time

A digestion time-course study was performed to determine the incubation time required to achieve consistent and reproducible digestion efficiency. For this, recombinant AKT1 and AKT2 proteins were spiked into 100 µg *E. coli* lysate per replicate, followed by

tryptic digestion for 0, 0.5, 1, 2, 4, 6, 16, and 21 hours at 37 ºC at a trypsin:total protein ratio of 1:5 (w/w). Three replicates were performed at each time point. After digestion, the samples were placed on ice for 10 min to slow the digestion reaction, and then stored at -80 °C. After thawing on ice, 50 fmol AKT1 SIS was added to each sample, followed by affinity-enrichment and MALDI analysis. The quantified peptide levels of each time point were compared to the 1-hour time point using Microsoft Excel's student t-test to determine if there was a significant difference.

Trypsin concentration

Tissue and cell lysates used in this project were generated by using lysis buffers that contained 1× Pierce Halt protease and phosphatase inhibitors. Due to varying total protein concentrations between samples, and the need to adjust each sample to the same final total protein concentration prior to digestion (0.1 µg/µL), the protease and phosphatase inhibitor concentration in each sample was different, thereby potentially resulting in varying digestion efficiency between samples, which would have compromised the comparability of results. Thus, to assess the effect of these varying inhibitor concentrations on the digestion efficiency, MDA-MB-231 parental cell lysate was diluted with PBSC and spiked with protease inhibitor to achieve final protease inhibitor concentrations that covered the expected inhibitor concentration range across the samples (0.04, 0.07, 0.10, and 0.40x). The samples were digested as described in section 3.2.9, but with varying trypsin:total protein ratios (1:5, 1:2, 1:1, or 2:1; w/w), and were analyzed for AKT1.

3.2.12 *Optimizing the dephosphorylation reaction*

Dephosphorylation time

In order to determine a dephosphorylation reaction time that resulted in complete dephosphorylation of the target peptides, MDA-MB-231 cell lysate was digested and spiked with 5 fmol/well of synthetic pS473-AKT1 NAT and non-phosphorylated AKT1

SIS peptide. The samples were then dephosphorylated for varying lengths of time (0, 15, 30, 60, and 120 min) at 37 °C using a phosphatase concentration of 60 U/well, followed by iMALDI analysis.

Alkaline phosphatase concentration

To determine a suitable alkaline phosphatase concentration that resulted in complete dephosphorylation, three sets of experiments were performed.

The first experiment compared the dephosphorylation efficiency for three different alkaline phosphatase lots (lots #1, #2, and #3) with the goal of investigating previously observed phosphatase lot-to-lot variability. For this, 10 fmol/well of pS473-AKT1 NAT and 2 fmol/well of non-phosphorylated SIS were spiked into an *E. coli* digest. Three lots of alkaline phosphatase were added at varying concentrations (5, 10, 20, 30, and 60 U/well) and were incubated at 37 °C for 2 hours, followed by iMALDI analysis.

The second experiment was performed to assess the effect of phosphate-containing and phosphate-free buffer systems on the dephosphorylation efficiency. Concentrations of 10 fmol/well pS473-AKT1 NAT and 2 fmol/well of non-phosphorylated SIS were spiked into either PBSC or TBSC, and incubated with varying concentrations of alkaline phosphatase lot #3 at 37 °C for 2 hours, followed by iMALDI analysis.

The third experiment assessed whether switching to a phosphate-free tris-buffer system would reduce the inhibition of the phosphatase reaction so that the phosphatase concentration in the sample could be decreased, and thereby overcoming lot-to-lot variability of the phosphatase. For this, the *E. coli* lysates were spiked with varying amounts of phosphatase inhibitor, followed by digestion, using only non-phosphate buffers. Next, 10 fmol/well pS473-AKT1 NAT and 2 fmol/well of non-phosphorylated SIS were added to the digests, followed by the addition of varying levels of alkaline phosphatase lot #3 (1, 5, 20, and 20 U/well), incubation at 37 °C for 2 hours, and subsequent iMALDI analysis.

3.2.13 *Assay validation*

Linear range

To determine the linear ranges of the AKT1 and AKT2 iMALDI assays, *E. coli* lysate was digested and spiked with a constant amount of SIS peptide (2 fmol/well) and varying SIS^2 peptide concentrations, ranging from 0.1 to 20 fmol/well, using the parameters described in section 3.2.9. After MALDI analysis, calibration curves were generated in R using weighted ($1/x$ and $1/x^2$) and non-weighted linear regression. The criteria suggested by the FDA Guidelines for Bioanalytical Method Validation were used to establish the linear ranges of the iMALDI assays (U.S. Food and Drug Administration, 2013).

Analytical accuracy

Analytical accuracy was assessed by spiking MDA-MB-231 breast cancer cell lysate digests with varying amounts of AKT1 and AKT2 SIS^2 (2, 4, and 8 fmol/well), and a constant amount of SIS (2 fmol/well). Calibration curves ($1/x^2$-weighted) were generated by spiking *E. coli* lysate digests with varying amounts of AKT1 and AKT2 SIS^2 and a constant amount of SIS, and were used to quantify the SIS^2 peptides spiked into the MDA-MB-231 cell lysate digests. The accuracy was determined by comparing the theoretical and quantified SIS^2 amounts.

Interference testing

Interference testing was performed by quantifying the endogenous AKT1 and AKT2 target peptides from MDA-MB-231 cell lysate, both parental and EGF-induced, which were diluted by varying dilution factors. The peptide concentrations determined were evaluated for a linear relationship with the dilution factors.

Impact of peptide phosphorylation status on digestion efficiency

To assess any potential inhibitory effects of having phosphorylation sites close to the tryptic cleavage site on the AKT1 and AKT2 target peptides, the tryptic target peptides were synthesized which were extended by four N-terminal amino acids from the original protein sequence, each with a single phosphorylated serine or threonine (see Table 1). Phosphorylated NAT peptides as well as non-phosphorylated SIS peptides were spiked into a surrogate protein background (0.1 µg/µL BSA in 0.05% T-PER buffer, 20 mM TrisHCl, pH 8.1, and 0.015% CHAPS). Next, the samples were either digested first (as described in section 3.2.9), followed by dephosphorylation for 2 hours at 37 °C with 60 U/well alkaline phosphatase, or vice versa. The NAT/SIS ratios from the two sample preparation approaches were compared.

Determining a phosphorylation stoichiometry cut-off value

The calculation of a peptide's PS involves two NAT/SIS intensity ratios derived from the sample aliquot that received alkaline-phosphatase treatment (P+), and the mock sample aliquot (P-). Each of the two NAT/SIS ratios contributes a certain error to the final result. Therefore, to ensure that the calculated PS is not simply composed of accumulated measurement errors, a cut-off value based on experimental measurements needed to be established.

The data used consisted of iMALDI measurements for AKT1 and AKT2 concentrations from cell line and tumor lysates, as well as calibration curve points, where three technical replicates were available (AKT1: n = 88; AKT2: n = 23). Technical replicates for this set of experiments were defined as aliquots of the same sample undergoing the entire sample preparation procedure. The CVs for each triplicate were used to calculate the PS cut-off (as described in section 3.3.5).

3.3 Results and Discussion

3.3.1 *Evaluation of anti-AKT1 and anti-AKT2 peptide antibodies*

The functionality of the anti-AKT1 and anti-AKT2 peptide antibodies was assessed by enriching the AKT1 and AKT2 NAT and SIS peptides spiked into PBSC (Figure 12A and B) and the endogenous peptides derived by tryptic digestion of recombinant AKT1 and AKT2 proteins in PBSC (Figure 12C and D) or spiked into 100 µg of *E. coli* lysate protein (Figure 12E and F). All mass spectra showed distinct peaks for the light (NAT or END) and SIS peptides with no interfering signals, thus demonstrating the suitability of the antibodies to capture the target peptides from a simple buffer system as well as from digested lysates. In addition, the experiment proved the effectiveness of the antibodies in retaining the target peptides during the washing procedure while removing non-specifically-bound compounds.

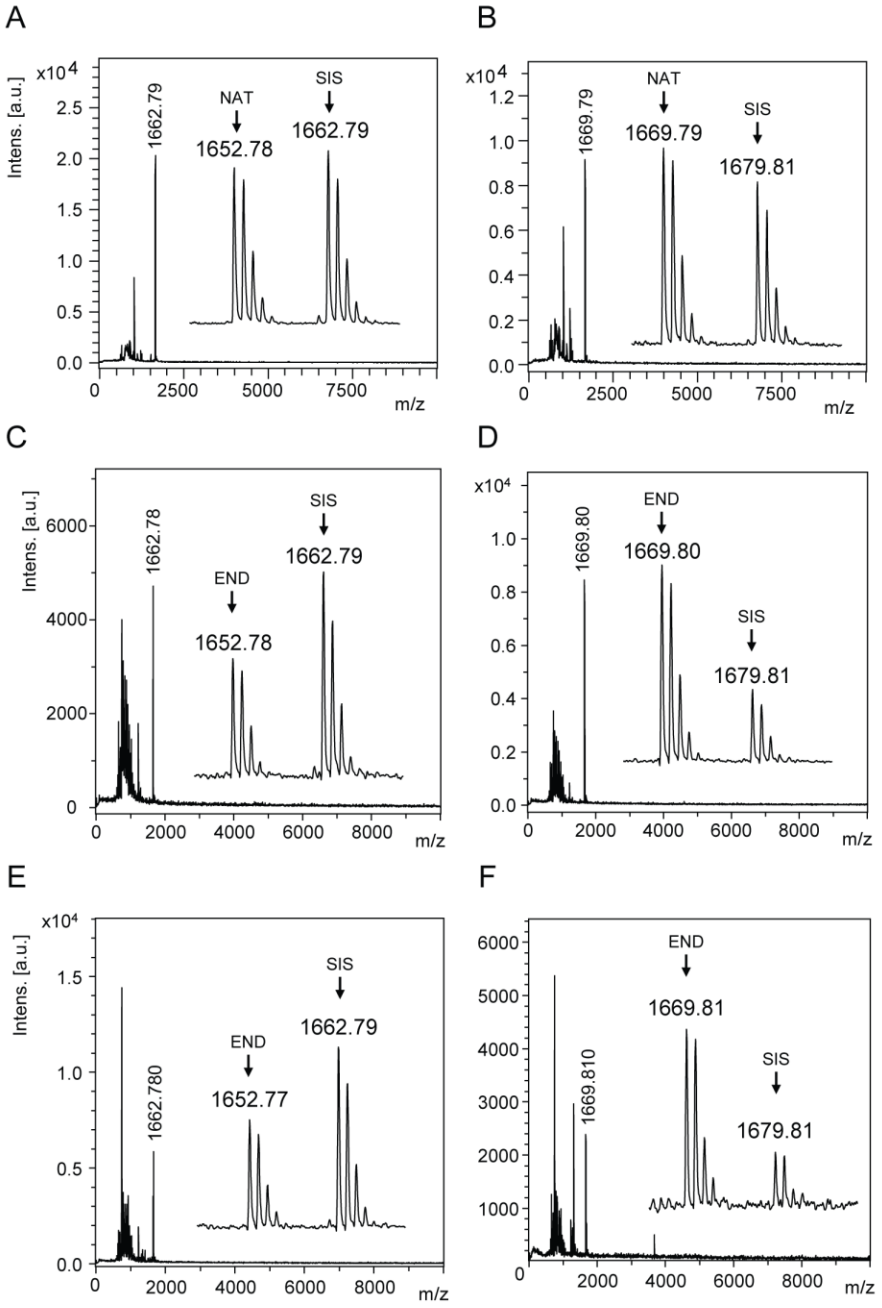

Figure 12: Mass spectra from the evaluation of anti-AKT1 and –AKT2 antibodies. Capture of (A) AKT1 and (B) AKT2 NAT and SIS peptides in PBSC buffer, and capture of digested recombinant AKT1 and AKT2 in (C, D) PBSC and (E, F) *E. coli* lysate, respectively. NAT = synthetic light peptide; END = endogenous peptide; SIS = heavy peptide.

3.3.2 *Optimizing digestion conditions*

Denaturant

Four denaturants commonly used in proteomic digestion procedures (DOC, GnHCl, SDS, and urea) were assessed for their suitability in the iMALDI workflow. The AKT1 NAT peptide was spiked into two background matrices of varying complexity (CEWA/PBS and human plasma), followed by denaturation with the four different denaturants, tryptic digestion, addition of AKT1 SIS, and enrichment using the iMALDI workflow.

The AKT1 NAT and SIS peptides were successfully enriched from the plasma digests (Figure 13A) and the CEWA/PBS digests (Figure 13B), using DOC-, GnHCl-, SDS, and urea-based denaturation protocols. The mass spectra acquired for the plasma digests using GnHCl, SDS and urea-based denaturation showed peaks from several non-specifically-bound compounds (Figure 13A). These were especially intense when using SDS. In contrast, use of the DOC denaturation protocol resulted in no observable non-specifically-bound components. For the CEWA/PBS digests (Figure 13B), low-intensity peaks from non-specific binding were observed with the SDS denaturant, whereas no peaks from non-specifically-bound compounds appeared in the DOC, GnHCl, or urea conditions. Furthermore, the isotopic peak patterns of the NAT and SIS peaks measured from the SDS and urea-based CEWA/PBS digests showed lower resolution than the peaks from the DOC- and GnHCl-denatured samples.

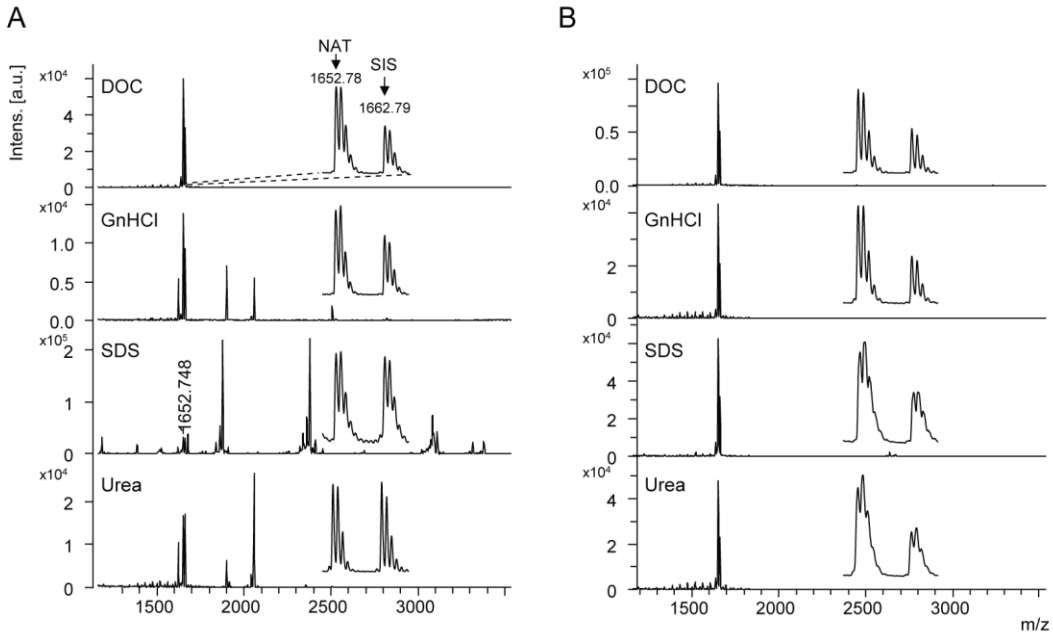

Figure 13: Mass spectra acquired for AKT1 NAT and SIS spiked and captured from (A) human plasma and (B) chicken egg white albumin in PBS (CEWA/PBS) digested with different denaturation protocols based on DOC, GnHCl, SDS, and urea.

Additional important aspects for a clinical assay are quantitative accuracy, reproducibility, and sensitivity. All four denaturation protocols resulted in comparable AKT1 NAT concentrations when captured from CEWA/PBS digests, with accuracies ranging from 94.8% for SDS to 106.4% for GnHCl (Figure 14A). However, for the plasma digests, only the DOC- and GnHCl-based denaturation protocols resulted in accuracies of >85%, while the SDS- and urea-based denaturation protocols resulted in accuracies of ~55%. This could be explained by the presence potential interferences arising from the plasma digests when using SDS or urea, as could be inferred from the elevated non-specific background as seen in Figure 13A. Furthermore, the DOC-based protocol resulted in the highest precision with CVs below 2% in both plasma and CEWA/PBS (Figure 14A). While the other three denaturants showed excellent precision in CEWA/PBS (with CVs below <5%), the CVs in plasma for GnHCl, SDS, and urea were 15.5%, 2.4%, and 6.4%, respectively.

In addition, the sensitivity, evaluated by the S/N ratio of the SIS peptide, was significantly higher when using the DOC-based denaturation protocol, for both plasma and CEWA/PBS (Figure 14B). For plasma, the average S/N achieved with the DOC protocol was 708, followed by 348, 214, and 57 for urea, GnHCl, and SDS, respectively. For the CEWA/PBS digests, the DOC protocol resulted in a S/N of 853, whereas S/N values of only 384, 527, and 502 were achieved for urea, GnHCl, and SDS, respectively.

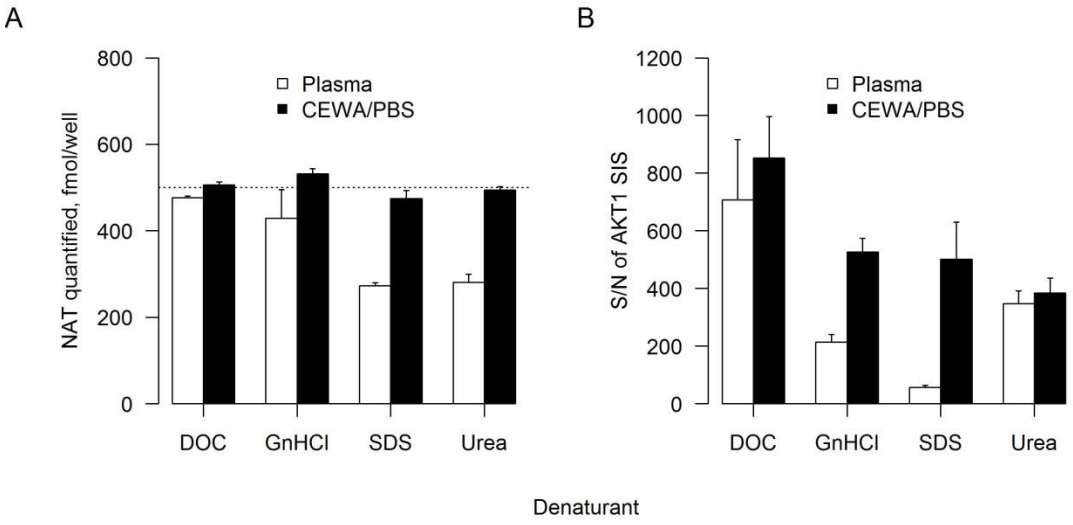

Figure 14: Denaturant comparison. (A) AKT1 NAT quantified and (B) S/N of AKT1 SIS. The dashed line marks the theoretical spike-concentration of 500 fmol/well.

In conclusion, DOC resulted in the lowest non-specific background, excellent isotopic resolution, highest accuracy, precision, and sensitivity, and was therefore determined to be the denaturant that was the most compatible with the iMALDI protocol.

Digestion time

The time-course digestion study of recombinant AKT1 and AKT2 spiked into 100 µg of *E. coli* lysate demonstrated consistent digestion between 0.5 and 6 h for AKT1, and between 0 and 16 h for AKT2, as indicated by comparable peptide amounts quantified (Figure 15A), precision of the triplicates within 15% (Figure 15B), and comparable

sensitivities (Figure 15C). The digestion observed at the 0-h time point can be explained by rapid digestion occurring right after addition of trypsin to the sample (prior to placing the sample on ice) and during the steps of the sample preparation at room temperature, such as the affinity-enrichment step. Interestingly, the AKT2 peptide appears to gradually degrade at digestion times above 4 hours (Figure 15A), with a significant difference at the 21-hour digestion compared to the 1-hour digestion point. This type of behaviour has previously been described in the literature (Proc et al., 2010), and the peptide-dependent variability in rates of generation of the target peptides via digestion, and degradation over time, is the main reason why digestion time-course studies should be performed for each target peptide during assay development.

In conclusion, based on these results, subsequent experiments were performed with a 1-hour digestion period.

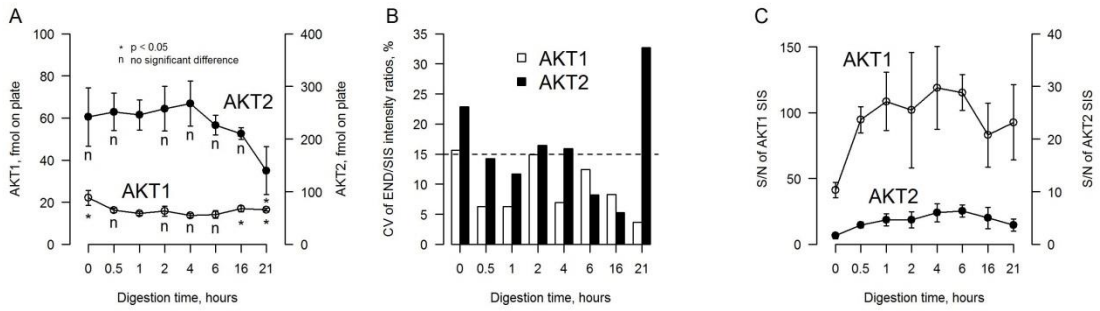

Figure 15: Time-course digestion study of recombinant AKT1 and AKT2 in 100 µg *E. coli* lysate at 37 ºC. (A) Peptide amounts quantified. (B) Precision of the triplicate END/SIS ratios. (C) S/N of the AKT1 SIS peaks.

Trypsin concentration

To further determine the amount of trypsin that was required for consistent digestion efficiency and which was independent of the protease inhibitor concentration, varying trypsin:total lysate protein ratios were compared over the range of expected protease-inhibitor concentrations in tissue-lysate samples. As can be seen in Figure 16A, a

trypsin:total protein ratio (w/w) of 2:1 was necessary to achieve consistent digestion efficiencies across all protease inhibitor concentrations tested. Furthermore, sensitivities were found to be comparable for all of the trypsin:total protein ratios tested (Figure 16B).

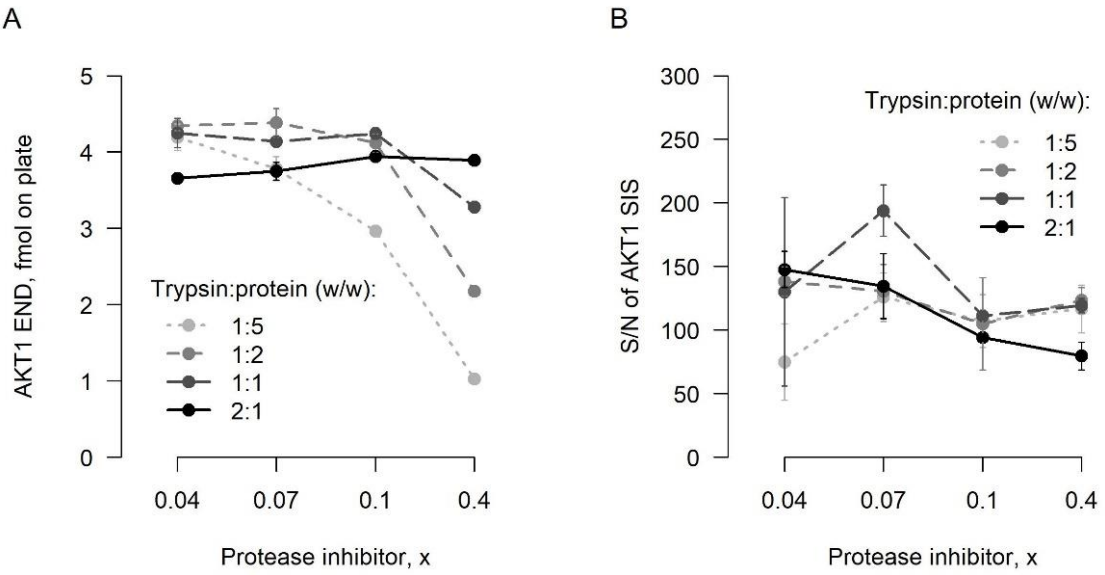

Figure 16: Impact of protease inhibitor and trypsin concentration on digestion efficiency.

In conclusion, a trypsin:total protein ratio of 2:1 was found to be required to ensure consistent digestion efficiency across all expected protease inhibitor concentrations.

3.3.3 *Optimizing dephosphorylation reaction*

Dephosphorylation time

In order to determine a dephosphorylation reaction time that ensured complete dephosphorylation of the target peptides, synthetic pS473-AKT1 NAT peptide was spiked into a MDA-MB-231 cell lysate digest and dephosphorylated for varying lengths of time using a phosphatase concentration of 60 U/well. The dephosphorylation reaction was approximately >95% complete at 60 min, but 120 min were required to completely dephosphorylate the target peptide (Figure 17). This reaction could be monitored by the formation of the non-phosphorylated peptide and the decrease in the signal for the

phosphorylated peptide. The observation of the phosphorylated peptide in the mass spectra was possible due to the cross-reactivity of the polyclonal anti-AKT1 antibody for both the phosphorylated and non-phosphorylated AKT1 peptide. However, the pS473-AKT1 NAT/SIS signal intensity ratio was lower than expected, which could possibly be explained by the lower enrichment and ionization efficiencies of the phosphorylated peptide compared to the non-phosphorylated peptide, This supports the use of a dephosphorylation approach, rather than targeting and directly measuring the concentration of the phosphorylated peptide. In conclusion, a 120-min dephosphorylation period was found to be optimal to achieve complete dephosphorylation.

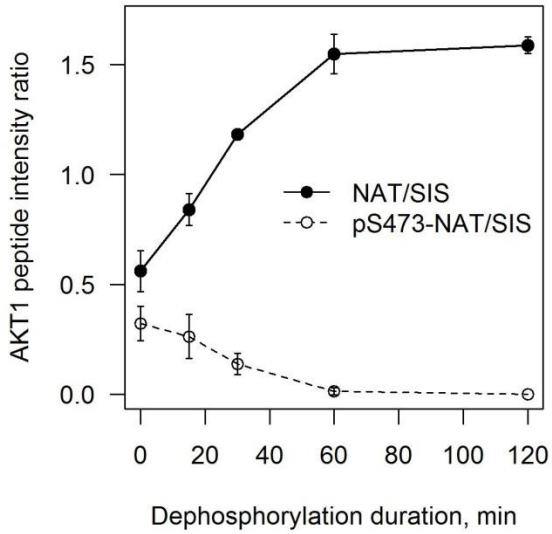

Figure 17: Assessment of the dephosphorylation time. The AKT1 NAT/SIS signal intensity ratio tracks the non-phosphorylated peptide, and the AKT1 pS473-NAT/SIS ratio follows the phosphorylated peptide.

Alkaline phosphatase concentration

From my initial titration experiments, which were performed to assess the alkaline phosphatase concentration necessary to completely dephosphorylate the target peptides, the ideal phosphatase concentration was found to be 60 U/well (data not shown).

However, switching to a different lot of phosphatase resulted in complete signal loss at 60 U/well. Therefore a comparison of the original phosphatase lot (lot #1), and two different lots (lots #2 and #3) was performed by dephosphorylating pS473-AKT1 NAT peptide spiked into *E. coli* lysate digests.

As can be seen from Figure 18A, all three phosphatase lots showed a clear trend of increasing non-phosphorylated AKT1 peptide concentrations with increasing phosphatase concentration, and therefore increasing the dephosphorylation efficiency, with a maximum being reached at 60 U/well for lot #1. For lots #2 and #3, no signal was observed at 60 U/well, confirming my previous observations. Furthermore, even at 30 U/well, the S/N was significantly lower for lots #2 and #3 when compared to lot #1 (Figure 18B). These findings indicate that phosphatase concentrations of less than 60 U/well would be needed to ensure the generation of sufficient signal, independent of the phosphatase lot, but that a lower alkaline phosphatase concentration would dephosphorylate the target peptides at less than 100% efficiency. Therefore, inhibition of the alkaline phosphatase by other reagents used in the sample preparation procedure had to be reduced.

One possibility to achieve this would have been to reduce the amount of phosphatase inhibitors in the sample. Because the amount of phosphatase inhibitors added to each sample was tied to the lysis protocol, it stayed constant at a concentration of 1×, so this variable could not be addressed, but the sample preparation protocol up to this point had been performed using a combination of tris- and phosphate-buffers. Therefore, the effect of completely eliminating the phosphate buffer -- an inhibitor of alkaline phosphatase -- until *after* the dephosphorylation step in the iMALDI protocol was examined.

As can be seen from Figure 18C, dephosphorylating the pS473- AKT1 NAT peptide in PBSC using the alkaline phosphatase lot #3 resulted in the previously observed trend of increasing concentrations of dephosphorylated peptide being generated with increasing phosphatase concentrations. However, when dephosphorylating in TBSC, which contained no phosphate that could inhibit the phosphatase, even at the lowest phosphatase concentration of 1U/well, significantly higher levels of non-phosphorylated AKT1 NAT could be quantified. This confirmed the assumption that switching from phosphate- to

tris-based dephosphorylation buffer could reduce the inhibitory effects on the alkaline phosphatase, and potentially allow a reduction in the phosphatase concentration while still achieving complete dephosphorylation. Additionally, both buffer systems resulted in comparable sensitivities, as measured by the S/N ratio of the AKT1 SIS signal, and a similar trend of decreasing sensitivity with increasing phosphatase concentrations (Figure 18D). Again, however, no signal could be generated at 60 U/well for phosphatase lot #3.

The final experiment assessed whether the phosphatase concentration could be reduced when switching to a phosphate-free buffer. As shown in Figure 18E, while phosphatase concentrations of 1, 5, and 10 U/well resulted in inhibited phosphatase activity, especially in the presence of high concentrations of phosphatase inhibitor, 20 U/well resulted in complete dephosphorylation for low, medium, and high phosphatase inhibitor-containing samples. While increasing phosphatase inhibitor concentrations appear to result in decreased sensitivity, especially for 10 and 20 U/well, the signal is still sufficient to allow switching from a phosphate-based to a tris-based buffer (Figure 18F).

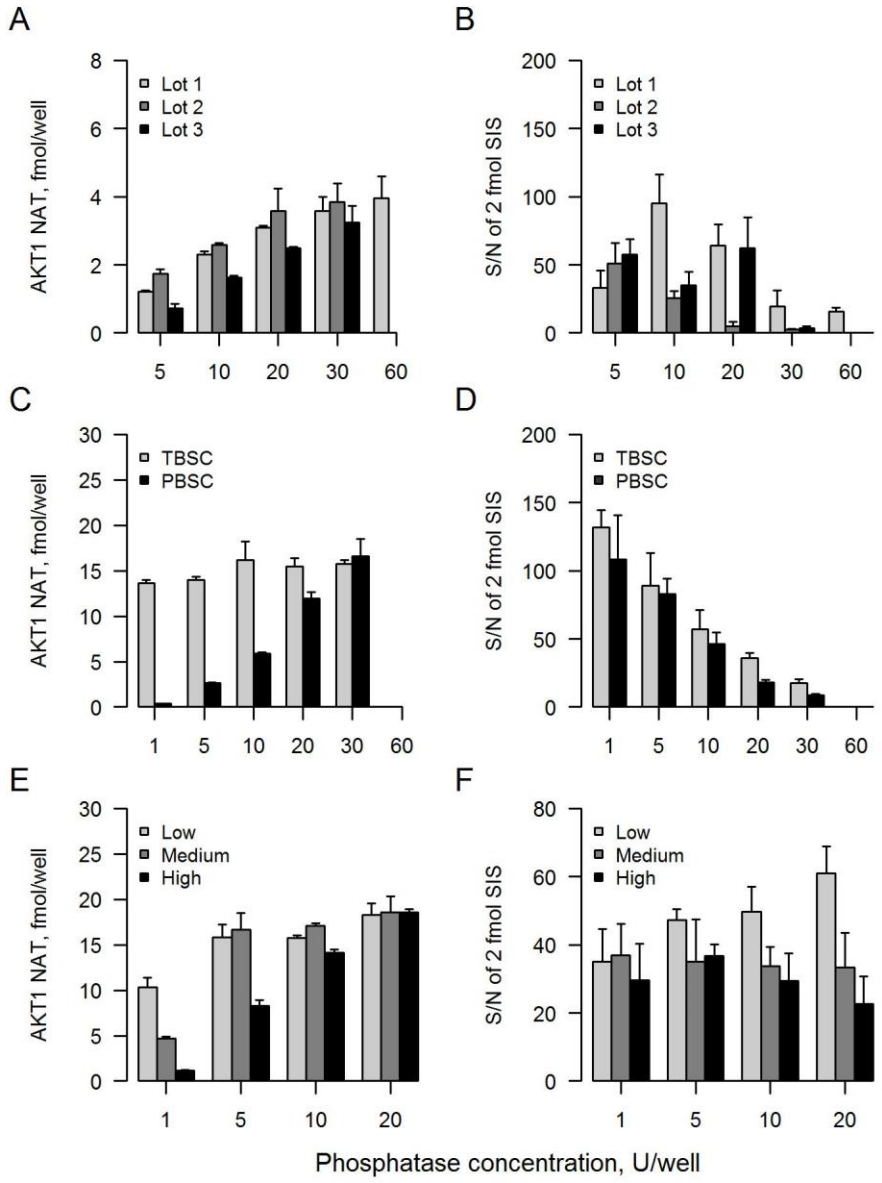

Figure 18: Optimization of the dephosphorylation reaction. (A, B) Comparison of three phosphatase lots. (C, D) Impact of a tris-based compared to phosphate-based buffer system on dephosphorylation efficiency. (E, F) Titration of the phosphatase concentration using the optimized reaction conditions. Graphs A, C and E show the quantified AKT1 concentrations and graphs B, D and F show the S/N ratios of the AKT1 SIS peaks.

In conclusion, switching from a phosphate- to a tris-based buffer system allowed me to overcome the observed phosphatase lot-to-lot variability issue.

3.3.4 *Sensitivity optimization*

To increase the assay sensitivity and thus to be able to reduce the amount of sample required, several parameters were evaluated, including the effect of different sample dilution buffers, adjusting the MALDI matrix composition, and different wash buffers prior to spotting the magnetic beads on the MALDI plate. However, these experiments resulted in only negligible improvements in sensitivity. In contrast, washing the dried MALDI spots after the matrix application step resulted in significant improvements in signal-to-noise ratios (Figure 19A). Of the three wash buffers studied, 7 mM ammonium citrate showed the largest signal increase -- approximately 20-fold, from an average S/N of 6 with no washing, to an average S/N of 130 when washed three times. H_2O and 7 mM ammonium citrate/0.1% TFA washes resulted in maximum S/N increases of 15- and 10-fold, respectively. The idea of washing MALDI spots to improve the sensitivity of peptide analysis has been reported in the literature previously, and it has been hypothesized that the signal improvement by washing of the MALDI spots is due to desalting and removal of impurities (Smirnov et al., 2004; Vorm et al., 1994).

Based on these findings, an automated spot-washing protocol was developed for the Agilent Bravo platform, which allows reproducible spot washing of up to 384 MALDI spots in approximately 30 min. The automated protocol was further assessed for the optimal wash buffer temperature and resting time on the MALDI spots (Figure 19B). The results showed an approximately 2-fold increase in S/N when using a room temperature wash buffer and a resting time of 5 seconds, compared to resting times of 0 or 3 seconds. In contrast, using a cold wash buffer at approximately 4 °C resulted in comparable S/N ratios for all time points.

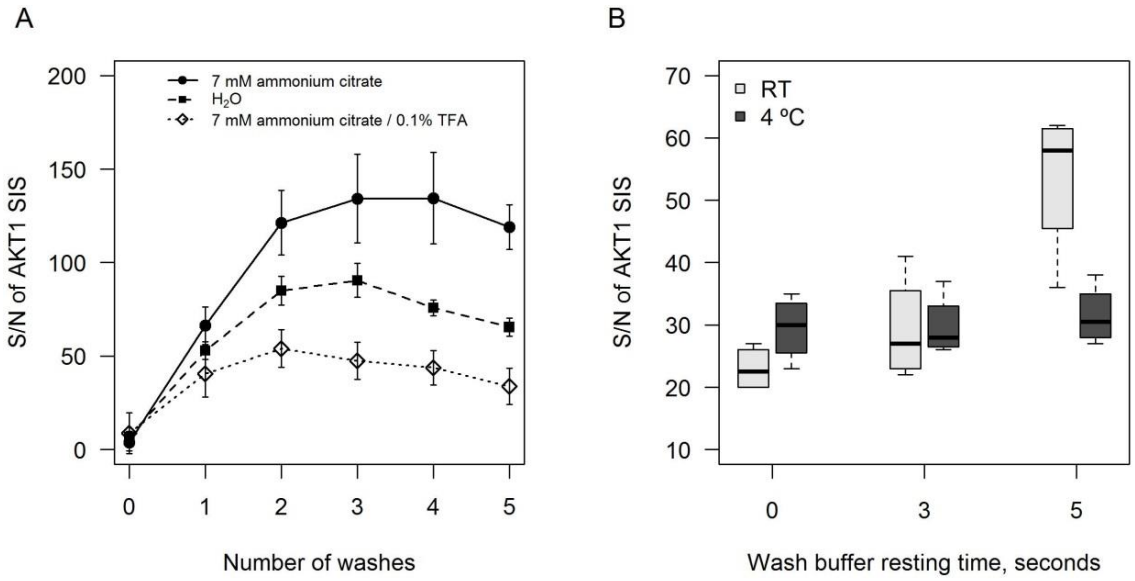

Figure 19: Impact of washing the MALDI spots on the sensitivity of the assay. (A) Comparison of wash buffers and number of washes, performed manually. (B) Assessment of wash buffer temperature and wash-buffer resting time on the MALDI spots, performed on an Agilent Bravo.

In conclusion, the sensitivity was increased when the MALDI spots were washed three times with 7 mM ammonium citrate at RT, with a resting time of 5 seconds. This allowed me to reduce the sample amount required for each capture from 100 µg total protein to 10 µg total protein.

3.3.5 *Assay validation*

Assay validation experiments were carried out using the final assay parameters, as described in section 3.2.9.

Linear range

The linear ranges of the AKT1 and AKT2 iMALDI assays were determined by spiking varying amounts of synthetic AKT1 and AKT2 SIS^2 peptides, and constant amounts of AKT1 and AKT2 SIS peptides (2 fmol/well) into digests of 10 µg of *E. coli* lysate. The resulting SIS^2/SIS intensity ratios were evaluated using weighted (1/x and $1/x^2$) or non-weighted linear regressions (Figure 20). The parameters assessed included the error of the mean concentrations (determined at each spiked concentration) to the regression line (Figure 20D-F), and the precision at each spiked-in concentration (Figure 20G), in accordance with the FDA guidelines (U.S. Food and Drug Administration, 2013).

All three weighting methods resulted in excellent R^2 values ranging from 0.985 to 0.998 (Figure 20A-C). In addition, the slopes of the linear regression lines were within ±10% of the expected slope of 1, with values of 0.98, 0.99 and 0.98 for AKT1, and 0.96, 0.95, and 0.91 for AKT2 for the non-weighted, 1/x-weighted and $1/x^2$-weighted regressions, respectively. These results indicated that intensity ratios can be used to confidently quantify peptide concentrations.

Based on a S/N cut-off of 3, the limits of detection (LODs) for AKT1 and AKT2 were determined to be 0.2 and 0.5 fmol/well, respectively. Furthermore, the percent error of the mean amounts quantified at each point from the regression lines were plotted in Figure 20D-F. All three weighting methods resulted in errors within ±15% for a concentration range of 0.5 – 20 fmol/well for the AKT1 peptide. For the AKT2 peptide, the 1/x- and $1/x^2$-weighted linear regressions (Figure 20E and F, respectively) resulted in a concentration range of 0.5 – 20 fmol/well, within an error tolerance of ±15%. In contrast, using a non-weighted linear regression approach resulted in a narrower range of 1 – 20 fmol/well (Figure 20D). Additionally, for both the AKT1 and AKT2 peptides, the CVs of all replicates between 0.2 and 20 fmol of peptide on the plate was below 15% (Figure 20G).

Taken together, when applying either 1/x- or $1/x^2$-weighted linear regression, the linear ranges for the AKT1 and AKT2 assays ranged from a lower limit of quantitation (LLOQ) of 0.5 fmol to an upper LOQ (ULOQ) of 20 fmol/well, corresponding to 2.8 – 111 pg/µg of lysate protein for AKT1 and 2.6 – 102 pg/µg of lysate for AKT2.

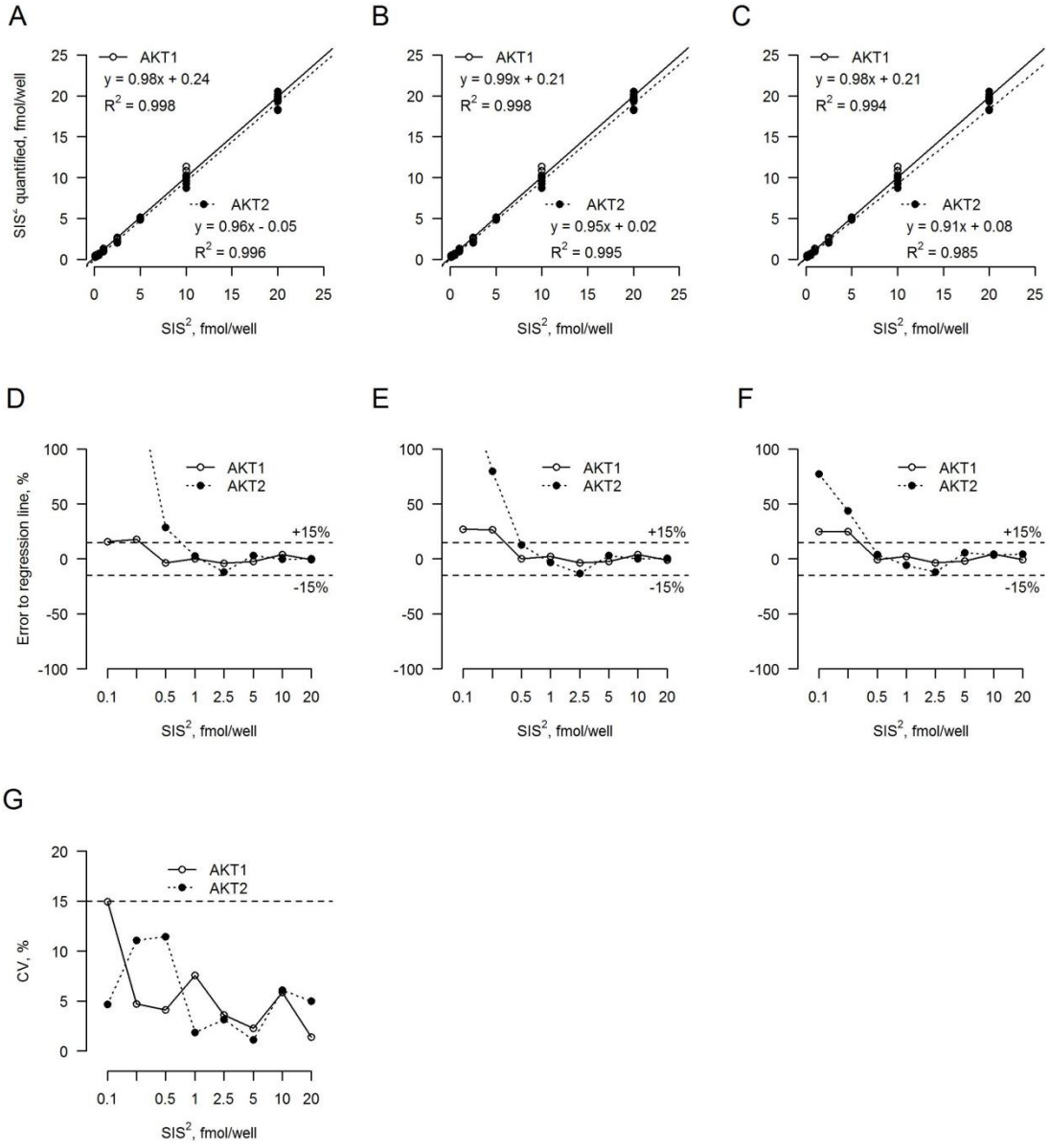

Figure 20: Linear range assessment. (A-C) Determination of the linear range of the assay. Regression lines for the AKT1 and AKT2 target peptides and (D-F) percent error of the mean concentrations to the regression lines, using either (A, D) no weighting, (B, E) 1/x weighting or (C, F) $1/x^2$ weighting. G) CVs for the technical replicates (n = 5) at each concentration.

The absolute sensitivity of the iMALDI assays is comparable to published approaches that combine immuno-enrichment with nano-LC/MS. For example, Whiteaker et al. (Whiteaker et al., 2015) and Patel et al. (Patel et al., 2015) achieved LOQs of ~2-8 fmol/mg using 500 µg total protein per analysis. Therefore, this corresponds to 1-4 fmol of AKT1 per replicate. The iMALDI assays presented here required only 10 µg of total protein, thereby achieving comparable sensitivity from significantly smaller sample amounts. This suggests that the iMALDI assays may be more suitable for the analysis of samples that yield only low sample amounts, such as needle core biopsies.

Analytical accuracy

The analytical accuracy of the developed iMALDI assays was assessed by spiking MDA-MB-231 breast-cancer cell-lysate digests with three levels of AKT1 and AKT2 SIS^2, and a constant level of SIS peptides. Calibration curves generated in digested *E. coli* lysate were used for quantification. Regression lines created with $1/x^2$ weighting for AKT1 (Figure 21A) and AKT2 (Figure 21B) showed excellent R^2 values of 1.00 and 0.99, and slopes of 1.03 and 1.07, respectively, demonstrating their suitability for quantifying the SIS^2 peptides in the MDA-MB-231 cell lysate digests. Accuracy values ranged from 87 and 98% (Figure 21C), thereby falling within the acceptable ranges of 100% ±15% as specified by the FDA Guidelines for Bioanalytical Method Validation (U.S. Food and Drug Administration, 2013).

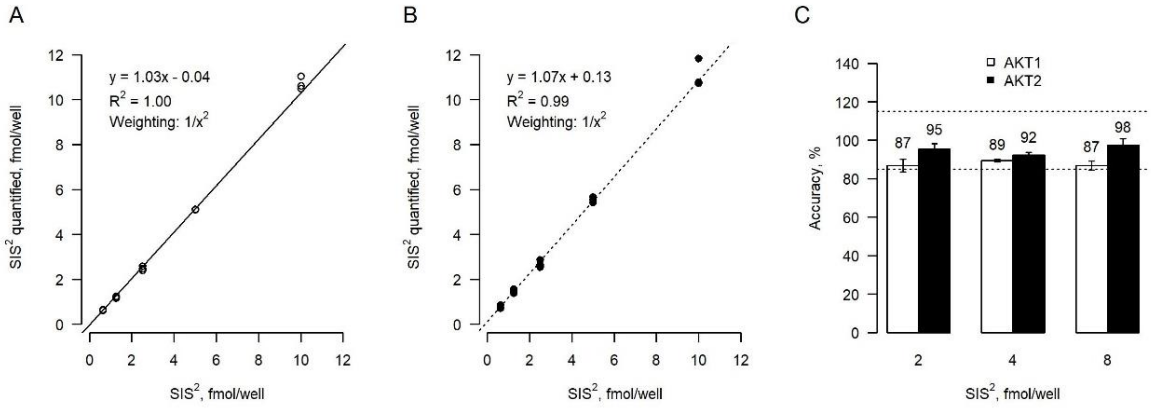

Figure 21: Determination of the analytical accuracy. Calibration curves for (A) AKT1 and (B) AKT2 were created using $1/x^2$-weighted linear regression. (C) Results for the analytical accuracy determined for SIS^2 peptides spiked at 2, 4 and 8 fmol/well into digested MDA-MB-231 cell lysate.

In conclusion, the analytical accuracy of the AKT1 and AKT2 iMALDI assays was found to meet the requirements for a clinically utilizable protein quantitation assay.

Interference testing

The levels of the endogenous AKT1 and AKT2 peptides quantified from serially diluted parental (Figure 22A) and EGF-induced (Figure 22B) MDA-MB-231 cell lysates, and the corresponding sample protein amounts analyzed show excellent correlation, with R^2 values above 0.99, indicating the absence of significant interference.

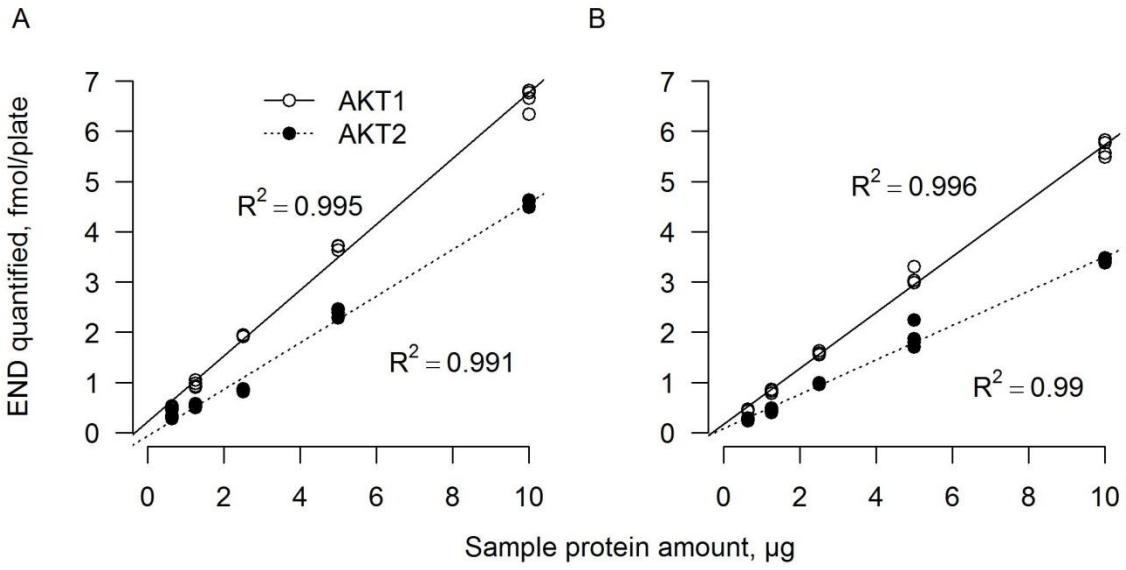

Figure 22: Interference testing in (A) parental and (B) EGF-induced MDA-MB-231 cell lysates.

Impact of phosphorylation status on digestion

Dickhut et al. reported that phosphorylation, in particular phosphorylation of serine and threonine residues in the proximity of a tryptic cleavage site in a protein, can reduce the digestion efficiency (Dickhut et al., 2014). To assess the potential impact of phosphorylated serine and threonine residues in AKT1 and AKT2 on the digestion efficiency, synthetic non-phosphorylated and singly phosphorylated targeted peptides, extended by 4 amino acids to the N-terminal side of the tryptic cleavage side (AKT1: DSERRPHFPQFSYSASGTA; AKT2: LDQRTHFPQFSYSASIRE), were treated in two ways: 1) digestion followed by dephosphorylation, or 2) dephosphorylation followed by digestion.

As expected, for both AKT1 and AKT2 peptides, there was no observable difference between digesting or dephosphorylating first when *none* of the peptide residues were phosphorylated (Figure 23). Interestingly, singly-phosphorylated peptides resulted in *elevated* quantities of the digested, non-phosphorylated target peptides when peptides with phosphorylated serine residues were digested prior to being dephosphorylated. This was observed for both the AKT1 and AKT2 peptides and demonstrated that these phosphorylated residues did not inhibit the tryptic digestion efficiency. The most likely reason for this was that the tryptic cleavage site is located at a distance where the phosphoryl group does not affect the tryptic activity. This is in agreement with the literature (Dickhut et al., 2014). Why dephosphorylation of the phosphorylated residues *prior* to digestion resulted in lower non-phosphorylated, digested peptide amounts, is currently unclear, and would require follow-up experiments. However, at this point, the initial question was answered, and it was shown that the phosphorylated serine and threonine residues did not result in reduced digestion efficiency of the targeted peptides.

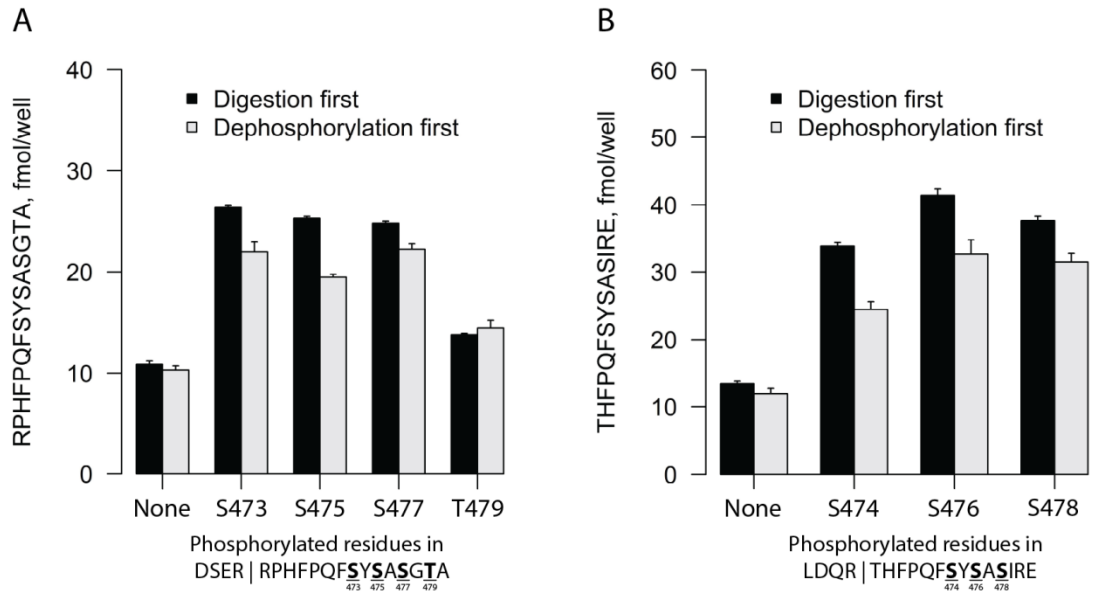

Figure 23: Impact of phosphorylation status on digestion efficiency. Quantified tryptic target peptide concentrations resulting from extended, tryptic target sequences with selected phosphorylated residues for (A) AKT1 and (B) AKT2. Samples were either digested prior to dephosphorylation, or vice versa.

Determining a phosphorylation stoichiometry cut-off value

To ensure confidence in the calculated PS, a cut-off value based on measurement errors was calculated. Determining the PS cut-off value for AKT1 and AKT2 was based on the assumption that the errors (*e*) were equal for both the concentration of the aliquot treated with phosphatase (*[P+]*) and for the concentration of the aliquot not treated with phosphatase (*[P-]*).

$$e_{[P+]} = e_{[P-]} \quad (1)$$

Based on this assumption, for the PS value to be due to actual phosphorylation, and not solely due to error, the difference of *[P+]* and *[P-]* must be larger than *2*e*, which is the desired cut-off value:

$$H_1 = [P+] - [P-] > 2e \quad (2)$$

Dividing by *[P+]* resulted in the following equation:

$$1 - \frac{[P-]}{[P+]} > 2 * \frac{e}{[P+]} \quad (3)$$

The term $\frac{e}{[P+]}$ can be calculated by dividing the standard deviation by the mean concentration of the replicates (in this case, triplicates) of the same sample, which results in the coefficient of variation.

Therefore, to determine the PS cut-off value, the maximum CV for 95% of the triplicate values was determined from 88 AKT1 and 23 AKT2 analyses (see Figure 24). The 95% value was chosen to ensure high confidence in the iMALDI PS result and to reduce the chance of false-positive results. The CVs were grouped into 1%-wide bins. For AKT1 and AKT2, 95% of the triplicate CVs were below 11% and 13%, respectively. Thus, the derived PS cut-off values were 22% for AKT1, and 26% for AKT2.

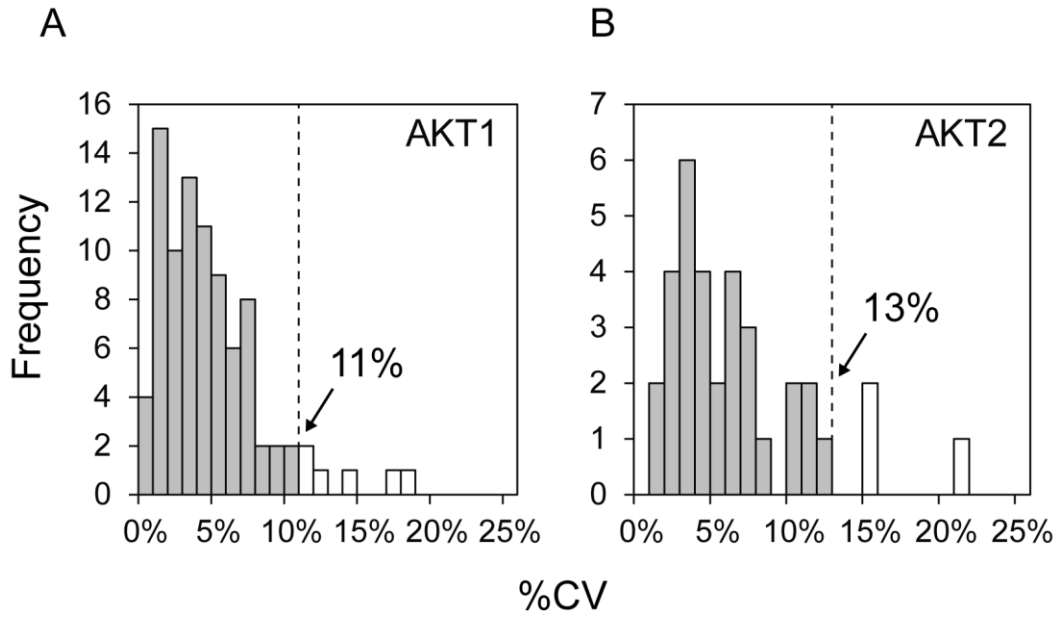

Figure 24: %CV distribution of triplicate values for (A) AKT1 (n = 88) and (B) AKT2 (n = 23). The sum of all gray bars represents 95% of all samples analyzed, whereas white bars indicate the remaining 5%.

While these cut-off values allow for the confident quantitation of phosphorylation stoichiometries, the majority of samples may show stoichiometries that are lower than these cut-offs. For instance, the analysis of the phosphoproteome in HeLa cells identified 38,229 phosphorylation sites and revealed high stoichiometries (>50%) only during the mitotic stage of the cell cycle. In contrast, during EGF-stimulation and without stimulation, most proteins showed low phosphorylation stoichiometries <25% (K. Sharma et al., 2014). Phosphoproteomic analysis of yeast further showed that approximately 50% of the 5,033 phosphorylation sites identified had stoichiometries below 20% (R. H. Wu et al., 2011). For AKT1 in particular, Atrih et al. quantified AKT1 pS473 phosphorylation stoichiometries using a targeted LC-MS/MS approach (Abdelmadjid Atrih et al., 2009). The authors determined that the AKT1 S473 PS in U-87 glioblastoma cells and was <2%, and <1% in resting T-cells. However, upon treatment with pervanadate (a potent tyrosine-phosphatase inhibitor), the T-cells showed AKT1 pS473 stoichiometry of 55%.

A potential methodology that could be applied to improve the sensitivity of the iMALDI measurements and thereby possibly improve the precision and thus lower the PS cut-off values is MALDI-Fourier-Transform/Ion Cyclotron Resonance (FT/ICR) MS which allows the accumulation of ions. While this approach could aid in a follow-up study to answer the hypothesis of this thesis project, FT/ICR MS is prohibitively expensive and complex for a clinical setting.

In conclusion, the iMALDI assays can be used to confidently calculate the PS values for AKT1 and AKT2 above 22% and 26%, respectively.

3.3.6 *Cell lines and flash frozen tumor samples*

Quantitation of AKT1 expression levels from 100 µg of total protein

In the early stages of the assay development, the suitability of the iMALDI protocol to detect endogenous target peptides from complex matrices was assessed by analyzing AKT1 from 100 µg of total-protein lysates of a breast-cancer cell line (MDA-MB-231, parental and EGF-induced), two colon-cancer cell lines (SW480 and HCT116), and two flash-frozen breast tumor samples (breast tumor samples T70-1 and T70-2, derived from the same tumor). Using the positive-ion reflector MALDI mode, the endogenous AKT1 target peptide was detected in all of the samples analyzed (Figure 25), with quantities ranging from 20 amol/µg (1.6 pg/µg) for breast tumor T70-1 and 458 amol/µg (25.5 pg/µg) for the parental MDA-MB-231 breast cancer cell line.

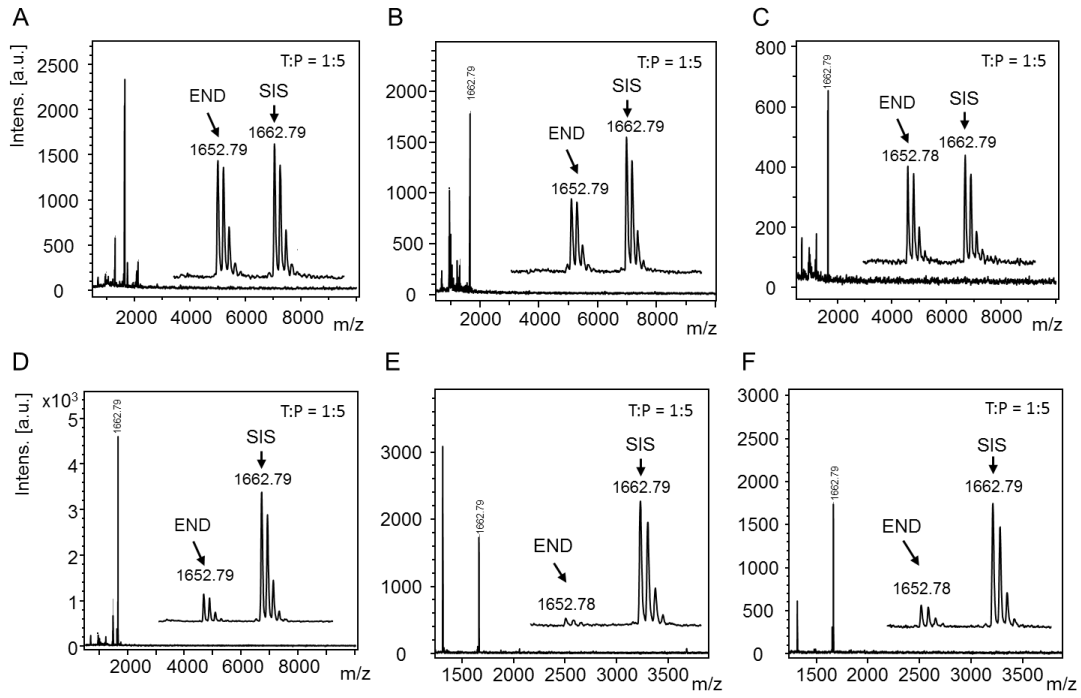

Figure 25: Mass spectra obtained from positive-ion reflector MALDI mode for cell lines and flash frozen tumor lysates analyzed for the endogenous AKT1 peptide RPHFPQFSYSASGTA using 100 µg total protein and 50 fmol/well AKT1 SIS per replicate. (A) Parental MDA-MB-231 breast-cancer cells, (B) EGF-induced MDA-MB-231 breast cancer cells, (C) SW480 colon cancer cells, (D) HCT116 colorectal-cancer cells, (E) breast tumor 70-1, and (F) breast tumor 70-2. Mass spectra were acquired by summing 1000 shots in positive reflector mode. T:P = trypsin:total protein ratio (w/w).

The total protein amount of 100 µg per replicate was in the same order of magnitude as other published MS-based quantitation methods that measure AKT1. For instance, Atrih et al. successfully analyzed AKT1 from 60 µg total protein of T-cells and a U-87 MG human primary glioblastoma cell line using a combination of SDS-PAGE, in-gel digestion and MRM analysis (Abdelmadjid Atrih et al., 2009). The same AKT1 target peptide used in the iMALDI assay was targeted (^{466}RPHFPQFSYSASGTA^{480}), which encompassed the key phosphorylation sites S473, S477, and T479. However, gel-based assays are impractical and too tedious for a clinical setting. Another example of AKT1 quantitation by MS is an immuno-MRM/parallel reaction monitoring (PRM) approach by

Patel et al., who quantified several PI3K/AKT/mTOR pathway members, including AKT1, from 500 µg of total protein from cancer cell lines (Patel et al., 2015). The feasibility of both approaches still has to be demonstrated for tissue samples. Furthermore, the Clinical Proteomic Tumor Analysis Consortium (CPTAC) assay portal lists two AKT1 assays (CPTAC-783 and CPTAC-784) and two AKT2 assays (CPTAC-788 and CPTAC-789) which are based on nano-liquid chromatography separation followed by PRM analysis (Office of Cancer Clinical Proteomics Research, 2017). These assays were validated in a pooled patient-derived xenograft (PDX) breast tumor digest matrix.

In summary, my experiments demonstrated that the developed iMALDI protocol is suitable for the quantitation of AKT1 from 100 µg of total protein from cancer cell lines and flash-frozen tumor samples. In theory, this would be sufficient for the analysis of needle-biopsy samples. For instance, my collaborators from the Jewish General Hospital in Montreal obtained 70-640 µg (median 139 µg) total protein from five biopsy protein extractions (data not shown). However, due to the limited amount of tissue available from small-core biopsies (approximately 2x10 mm) and the need to preserve approximately 2/3 of the material for DNA/RNA extraction for genomic/transcriptomic analysis, often only a small portion of a biopsy sample is available for protein analysis. Therefore, sensitivity optimization experiments were performed as described in section 3.3.4, with the goal of being able to reduce the sample amount required per analysis.

Quantitation of AKT1 and AKT2 expression levels from 10 µg of total protein per replicate

While the initial assay development was performed in positive-ion reflector MALDI mode for its higher resolution, the positive-ion linear MALDI mode was ultimately chosen due to its improved sensitivity and precision (data not shown). After this change and additional sensitivity optimization, namely MALDI spot wash optimization, , the feasibility of quantifying AKT1 and AKT2 expression levels from as low as 10 µg total protein per replicate was assessed. The samples for these experiments were breast-cancer

cell line MDA-MB-231, parental and EGF-induced, an HCT116 xenograft tumor, and three flash-frozen breast tumor samples.

Endogenous AKT1 and AKT2 was detected in all of the samples analyzed (Figure 26). Especially remarkable was the finding that in the breast tumor T-70-1 sample, shown in Figure 25E, the AKT1 END peptide was barely detectable, whereas with the procedure optimized for sensitivity, the AKT1 END peptide was clearly observable and quantifiable (Figure 26E), despite reducing the sample amount from 100 µg of total protein per replicate to 10 µg of total protein per replicate. The elevated abundances of the background peaks in the breast-tumor samples T70-1 and T70-2 (Figure 26E,F), as compared to the other mass spectra in Figure 26, was caused by the use of an elevated trypsin:total protein ratio of 2:1, which resulted in an increase in tryptic autolytic peptides which bound non-specifically to the magnetic beads. Nevertheless, no non-specific peaks interfering with the target peptides were observed. This observation demonstrated the significant advantage of using MS for distinguishing between target and non-target peptides, thereby reducing or even eliminating the chance of non-specificity and falsely-elevated peptide quantities. This is in contrast to other antibody-based methods where there is no MS detection, such as ELISA.

Another great advantage of coupling antibody-enrichment with MS is the ability to make use of cross-reactivity. For instance, the anti-AKT2 peptide antibody was found to be cross-reactive for the AKT1 peptide, as can be seen from the mass spectra in Figure 26G-J. While in the case of the AKT1 and AKT2 peptides used in this assay, two antibodies were chosen due to slightly overlapping AKT1 SIS and AKT2 NAT peptides in the mass spectrum and a lower binding efficiency of the AKT2 antibody for the cross-reactive AKT1 peptide, future targets could make use of this phenomenon by deliberately generating antibodies that are cross-reactive for more than one target peptide.

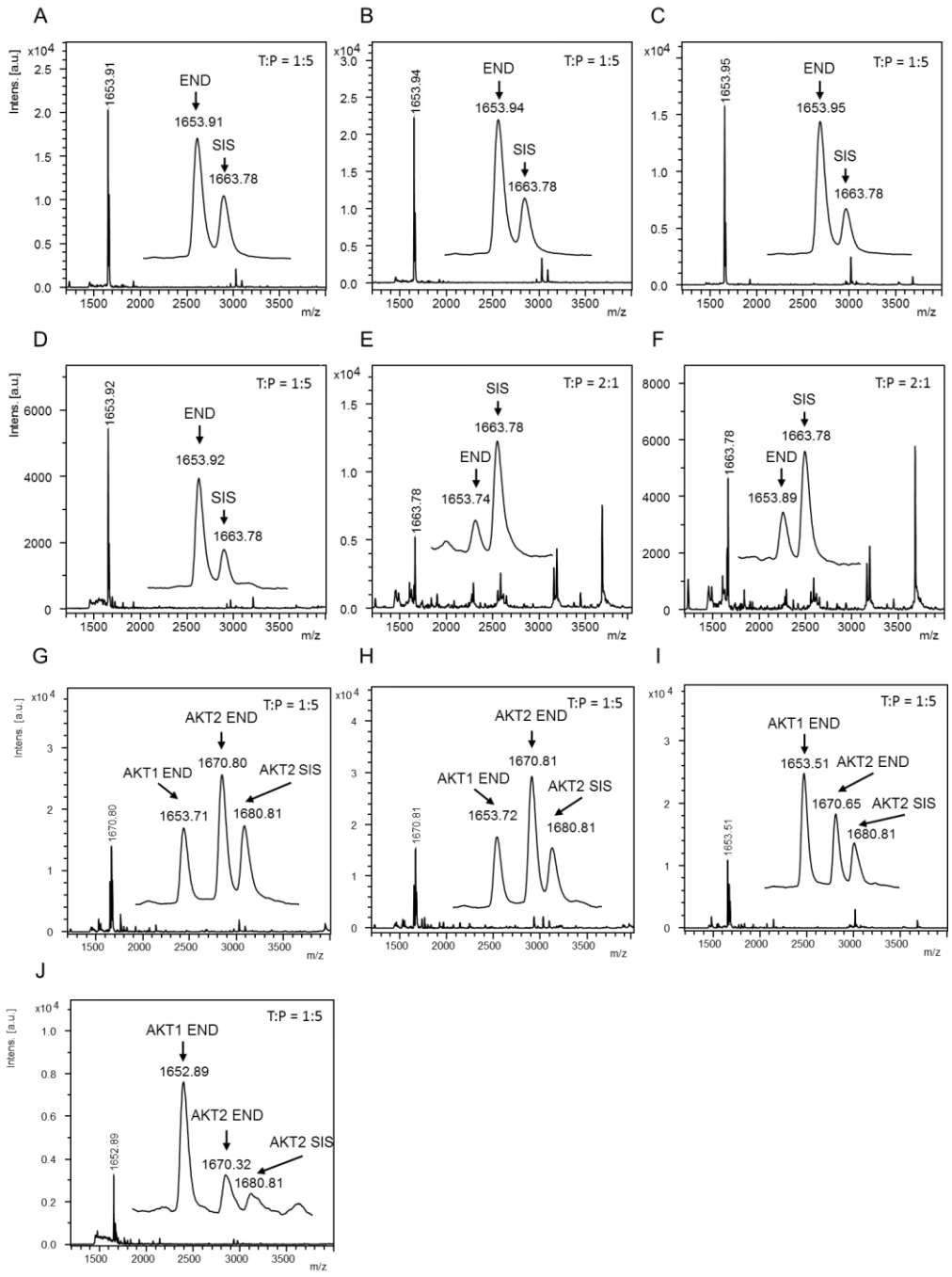

Figure 26: AKT1 and AKT2 quantified from 10 µg total protein cancer cell line and flash frozen tumor tissues. (A-F) Mass spectra showing the capture of endogenous AKT1 peptide RPHFPQFSYSASGTA at *~m/z* 1653.9 and the corresponding internally calibrated AKT1 SIS peptide (2 fmol/well) at *m/z* 1663.8, after digestion and enrichment from 10 µg of lysate protein per replicate. (A) MDA-MB-231 parental and (B) EGF-induced breast-cancer cell lysate, as well as flash-frozen tumor lysates from (C) HCT116 colorectal-cancer mouse

xenograft and (D-F) three different breast tumors, (D) T-607, (E) T70-1, and (F) T70-2. Digestions for spectra A-D were performed at a trypsin:protein (T:P) ratio of 1:5, whereas digestions for spectra E and F were performed at a T:P ratio of 2:1. (G-J) Mass spectra acquired from iMALDI analysis of AKT2 from 10 µg of (G) parental MDA-MB-231 breast cancer cells, (H) EGF-induced MDA-MB-231 breast-cancer cells, (I) HCT116 colorectal-cancer mouse xenograft tumor, and (J) a breast tumor.

Furthermore, the quantified values fell within the linear range (50-2000 amol/µg of total lysate protein) of the developed assays. The CVs for all samples were below 5%, except for tumor sample T70-1, due to an interference with the target AKT1 peak (Figure 27). The lowest AKT1 levels quantified were 51 and 93 amol/µg for the breast-tumor samples T70-1 and T70-2 (two samples from the same tumor tissue). The protein amount difference of approximately a factor of 2 could be explained by tumor heterogeneity. In contrast, the T-607 breast tumor and HCT116 colorectal cancer mouse xenograft tumor samples showed approximately 10-fold higher AKT1 levels -- approximately 600 amol/µg.

The AKT1 and AKT2 expression levels as determined by iMALDI were very comparable to literature values reported by Patel et al. who, as described above, used protein immuno-precipitation (IP) from 500 µg of A549 cell lysate followed by digestion and quantitation on a nano-LC/MRM-PRM-MS platform (Patel et al., 2015). The endogenous levels for AKT1 and AKT2 were in the range of 30-50 amol/µg. Considering that the protein yield after enrichment is highly dependent on the antibody and was determined by Patel et al. to be approximately 5% (Bhavin Patel et al., 2014), the iMALDI and nano-LC/MRM-MS values agree, demonstrating the comparability of the two approaches.

Additionally, commercially available AKT1 and AKT2 ELISA assays that list quantified AKT1 and AKT2 concentrations in their product descriptions showed comparable endogenous AKT1 levels from lysates of MCF7, HEK293, and HeLa cells [1525, 388, and 730 amol of AKT1/µg of lysate protein; human AKT1 ELISA kit (ab214023), Abcam, Inc.] and AKT2 levels from MCF7 lysate [875 amol of AKT2/µg of lysate protein; AKT2 ELISA kit (ab208986), Abcam, Inc.].

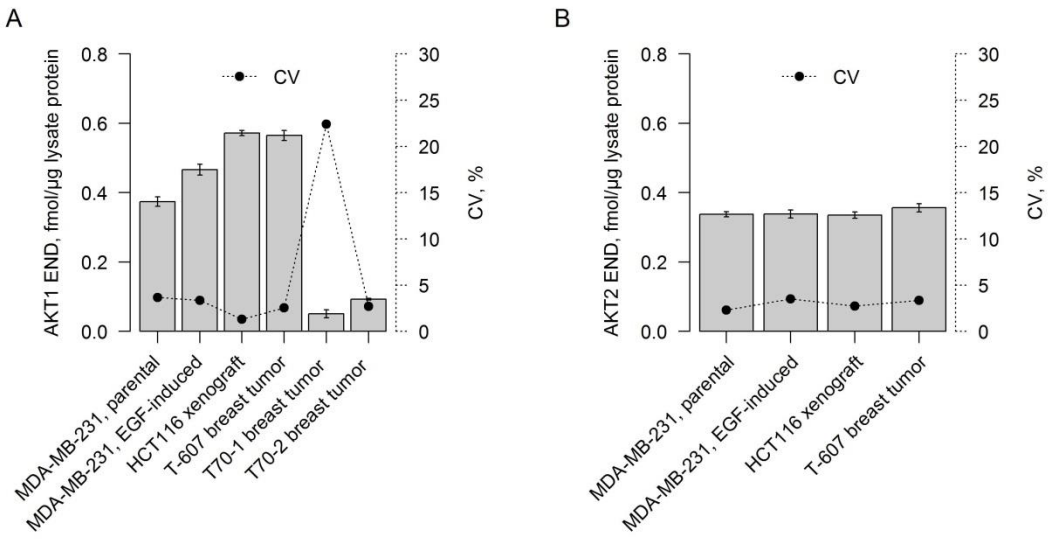

Figure 27: Endogenous (A) AKT1 and (B) AKT2 levels and intraday CVs from 10 µg lysate protein of breast cancer cell lines and tumor samples, as well as an HCT116 colorectal-cancer mouse xenograft tumor

AKT1 and AKT2 expression levels and phosphorylation stoichiometry from 10 µg total protein per replicate in cell lines and flash-frozen tumor samples

In the next step, the protein expression analysis was expanded to include PS analysis. To confirm the performance of the dephosphorylation step in actual cell lines and tumor samples, cell lysates of parental and EGF-induced MDA-MB-231 cells and 15 flash-frozen tumor lysates from breast biopsies, breast surgery, a CRC cell-line xenograft, and CRC liver-metastasis samples were analyzed (see Table 2).

Table 2: Overview of flash frozen tissue lysates for AKT1 and AKT2 expression and phosphorylation analysis

Type	Sample	Tumor cellularity	Necrosis
Breast biopsy	B-220	90%	NA
	B-294	90%	NA
	B-296	90%	NA
	B-298	75%	NA
	B-210	30%	60%
Breast surgery	T70-1	NA	NA
	T-607	NA	NA
	T-520	100%	0%
	T-425	90%	NA
CRC cell line xenograft	HCT116 XG	NA	NA
CRC liver metastasis, surgery	P-1098	70%	20%
	P-918	65%	25%
	P-532	25%	65%
	P-719 A1	NA	NA
	719	NA	NA

E. coli lysate spiked with pS473-AKT1 NAT, pS474-AKT2 NAT peptide, and AKT1 and AKT2 NAT peptides was used as a positive dephosphorylation control for the cell line experiments. For the tumor experiments, positive dephosphorylation controls were generated by spiking pS473-AKT1 NAT peptide into aliquots of HCT116 XG, T-607, and T70-1 samples.

The concentrations determined for AKT1 and AKT2 were comparable between the parental and EGF-induced MDA-MB-231 cell lysates, with AKT1 concentrations ranging from 0.40 to 0.47 fmol/µg (Figure 29A), and AKT2 values ranging from 0.20 to 0.26 fmol/µg (Figure 29B). Unexpectedly, the corresponding phosphorylation stoichiometries, calculated from the mean values of the phosphatase-treated (P+) and non-treated (P-) sample aliquots, ranged from only 0 to 3% (Figure 29C). Based on the western blot analysis performed at the JGH, the EGF-induced cell line sample should have shown elevated phosphorylation levels for both pS473-AKT1 and pS474-AKT2 (Appendix Figure 2A). However, the dephosphorylation control was positive (Figure 29C), thus demonstrating that the observed lack of phosphorylation in the cell lysates was not caused by a dysfunctional phosphatase.

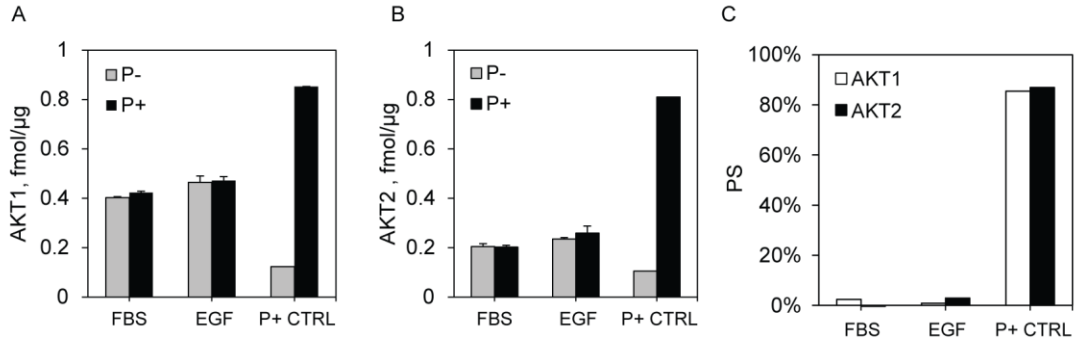

Figure 28: Expression levels and phosphorylation stoichiometry from MDA-MB-231 cells (parental and EGF-induced) using 10 µg lysate protein per replicate capture. Expression of (A) AKT1 and (B) AKT2. (C) Phosphorylation stoichiometries. FBS: no EGF-induction. EGF: EGF-induction. P+ CTRL: *E. coli* dephosphorylation control.

Next, to determine the concentration range of AKT1 and AKT2 expression in patient samples, and to further evaluate the measurement of PS, 15 flash-frozen tumor lysates were analyzed (Figure 29).

AKT1 was analyzed for all 15 samples, whereas AKT2 was analyzed in 7 out of 15 samples due to the limited sample amounts available. Of these seven samples, the AKT2 measurement in the T-425 sample (three technical replicates) resulted in no signal for either endogenous or the SIS peptide, indicating that potential matrix effects hindered the antibody-peptide binding.

As can be seen from Figure 29A, the AKT1 expression levels quantified ranged from 0.10 fmol/µg for T70-1 and 1.0 fmol/µg for B-298, covering a 10-fold concentration range. In contrast, AKT2 expression levels ranged from 0.13 fmol/µg for sample 719, to 0.56 fmol/µg for sample B-220, which corresponds to an approximately 4-fold concentration range (Figure 29C). All samples fell within the linear range of the assays of 0.05 – 2 fmol/µg, as determined in section 3.3.5. Interestingly, the six samples analyzed for both AKT1 and AKT2 expression showed a modest correlation, with an R^2 value of 0.57, and a slope of 0.59, indicating that, on average, the AKT2 measurements were lower than the corresponding AKT1 measurements (Figure 29C). Moreover, the iMALDI

expression values determined for AKT1 and AKT2 showed good correlation with the corresponding western-blot densitometry ratios of total AKT/loading control, derived from the western blot shown in Appendix Figure 2D, with R^2 values of 0.82 and 0.88, and slopes of 1.06 and 1.04 for AKT1 and AKT2, respectively (Figure 29G and H). This provides further evidence for the analytical accuracy of the iMALDI assays for quantifying AKT1 and AKT2.

Of all 15 samples, only the breast-biopsy sample T70-1 gave an AKT1 PS value above the cut-off (22%), with a value of 35% (Figure 29B). Two T70-1 sample aliquots were measured one month apart, resulting in the same 35% PS, which suggested that the phosphorylation was indeed elevated (data not shown). Additionally, as shown in Figure 29D, all of the AKT2 PS values for the six samples analyzed were below the corresponding PS cut-off (26%). To rule out potential matrix effects from the samples, synthetic pS473-AKT1 was spiked into aliquots of the tumor lysates of HCT116 XG, T-607, and T70-1, resulting in significantly elevated PS values (see Figure 29F). This confirmed that the observed low PS values were not due to matrix effects affecting the dephosphorylation efficiency. Furthermore, the corresponding western blot data (Appendix Figure 2), which assessed total AKT expression, total phospho-AKT expression at the conserved phosphorylation site S473/S474, or -- specifically -- the expression of pS473-AKT1 or pS474-AKT2, confirmed phosphorylated AKT1 and AKT2 in all of the tissue lysate samples. One possible explanation for why the iMALDI results only showed one sample with phosphorylation stoichiometry above the cut-off is that the western blot technique may be more sensitive in detecting the target phosphorylation sites than the iMALDI method. Furthermore, although the tissue lysates contained phosphatase inhibitors and were stored at -80 °C until analyzed, the phosphoryl group or groups on the target peptide could have been removed over time.

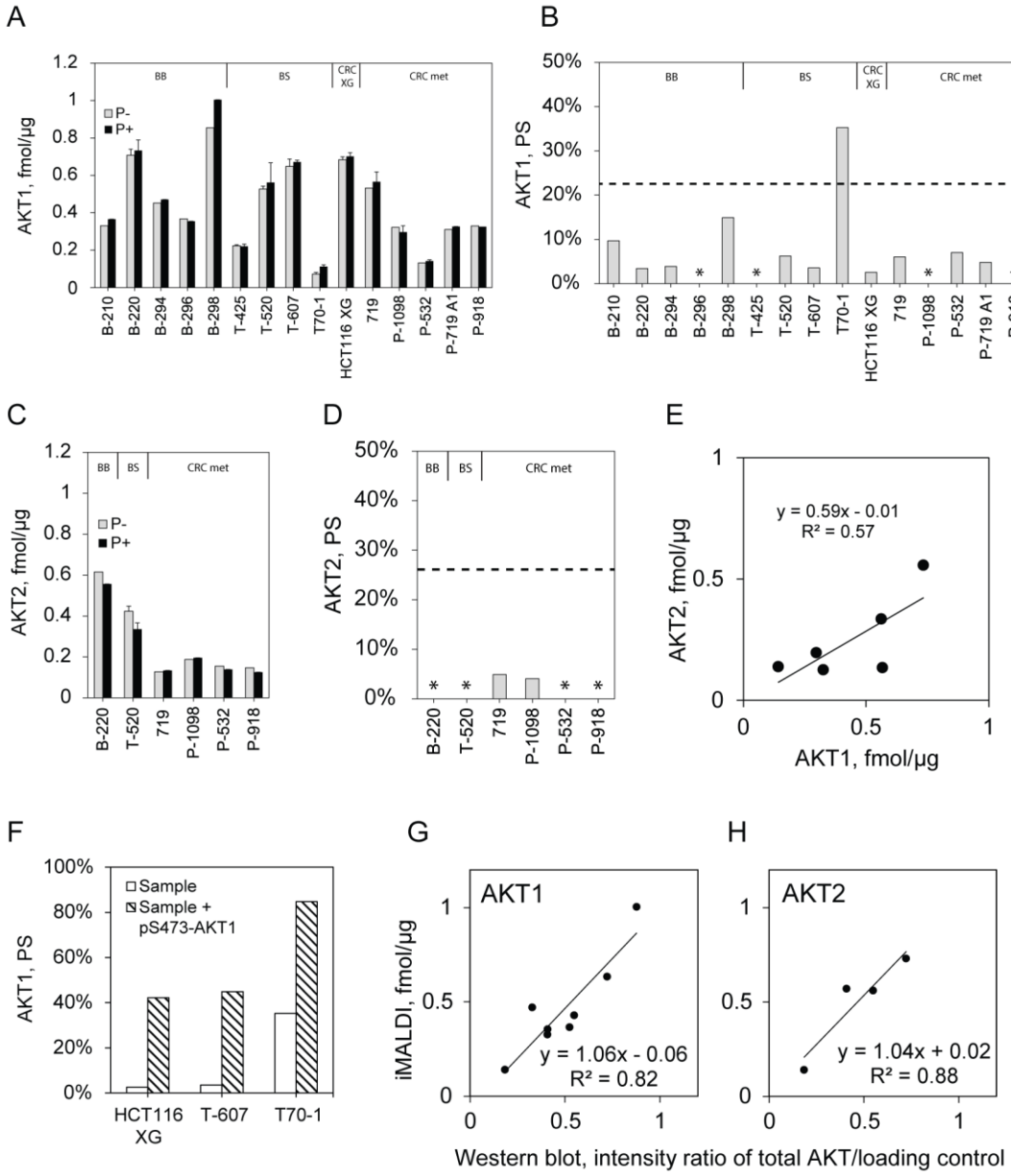

Figure 29: Results for AKT1 and AKT2 expression and PS analysis of 15 flash frozen tumor lysates by iMALDI. AKT1 (A) expression and (B) phosphorylation stoichiometry. AKT2 (C) expression and (D) phosphorylation stoichiometry. (E) Correlation of AKT1 and AKT2 expression values. (F) Positive dephosphorylation control results. (G, H) Correlation of western blot densitometry ratios with AKT1 and AKT2, respectively. *indicates negative PS values. The dashed lines indicates the PS cut-offs determined in section 3.3.5. BB = breast biopsy; BS = breast surgery; CRC XG = colorectal cancer cell line xenograft; CRC met = colorectal-cancer liver metastasis

In conclusion, a concentration range for expected AKT1 and AKT2 values has been established, and the capability of quantifying AKT1 and AKT2 from cell lines and flash-frozen tissue lysates has been demonstrated. Furthermore, the expression values determined by iMALDI assays showed good correlation with western blot data, whereas the phosphorylation stoichiometry determination by iMALDI at this point remains challenging and will need to be improved in the future.

3.3.7 *Comparison of matched flash-frozen and FFPE tissues*

Most of the tissue pathology specimens in clinics today are stored in an FFPE format. Using these samples for prospective and retrospective DNA, RNA or protein analyses is of great interest for both drug development and for precision medicine approaches (Kokkat et al., 2013). Therefore, being able to use iMALDI for the analysis of FFPE tissues would be of tremendous value. To assess this possibility, matched flash-frozen and FFPE tumor-tissue cores from breast biopsies, breast surgical tissues, and colorectal-cancer (CRC) tissues were provided by my collaborators at the JGH, where the tissues were quality assessed by a pathologist (Appendix Figure 1), and the expression of total AKT, total pAKT, as well as pS473-AKT1 and pS474-AKT2 were confirmed for the flash-frozen tissues by western blot analysis (see Appendix Figure 2).

Protein extraction from the FFPE tissue was performed as described in section 3.2.6. Three cores were used for each sample extraction. In total, 15 samples were provided as FFPE cores, consisting of 9 tumor samples and 6 matched normal tissue samples. As can be seen from Figure 30, the CRC liver-metastasis samples resulted in the largest protein amounts extracted, while the breast biopsy and breast surgery samples resulted in significantly lower protein yields. In particular, the protein extraction from two breast biopsy samples (B-294 and B-298) resulted in no detectable protein at all. Due to the varying protein yields, only 6 of the 9 matched FFPE and flash-frozen sample, and only 4 of the 6 tumor and adjacent normal tissues could be compared (see section 3.3.8).

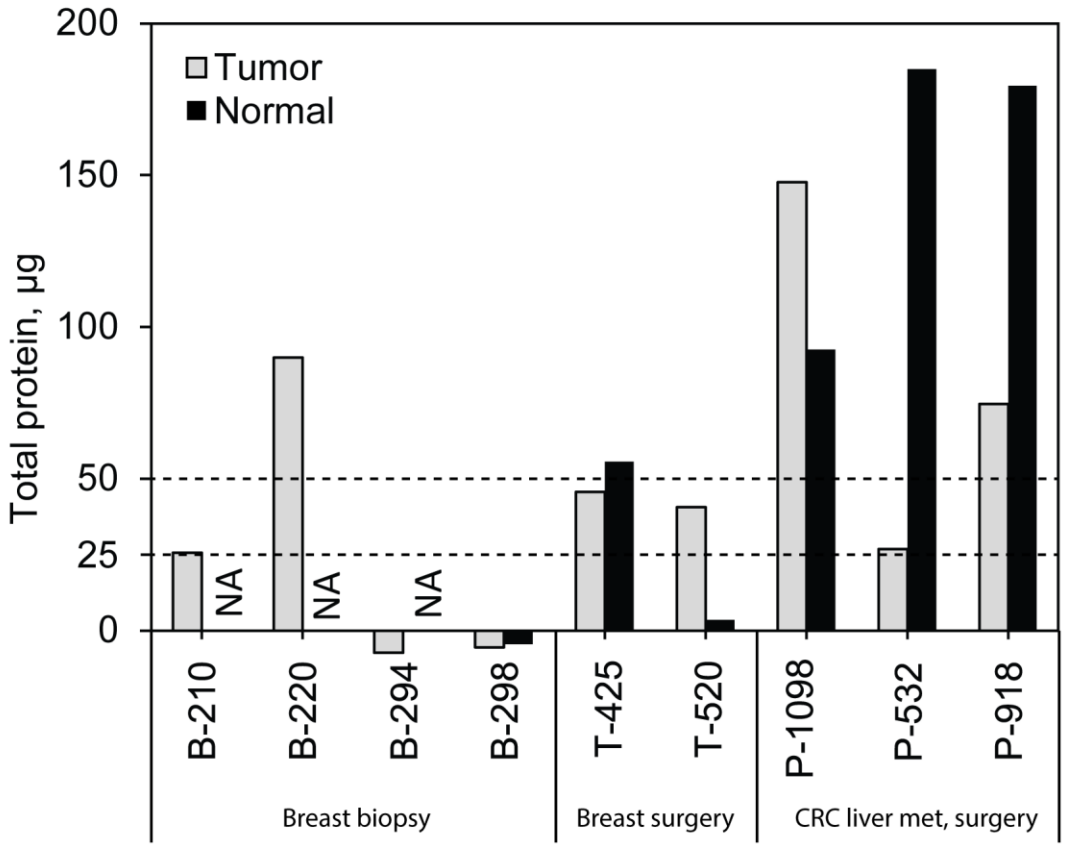

Figure 30: Total protein amounts quantified from normal and matched tumor-FFPE core-tissue lysates by BCA assay. NA indicates that no matching FFPE cores were available. The dashed lines represent the minimum protein amounts required for the analysis of either AKT1 or AKT2 expression and PS (25 µg required), or both AKT1 and AKT2 expression and PS (50 µg required).

Next, the six matched flash-frozen and FFPE-tissue lysates were analyzed by iMALDI and compared for protein expression levels and PS.

Both AKT1 and AKT2 could be quantified from flash-frozen and FFPE-tissue lysates (Figure 31), with the exception of AKT2 for the flash-frozen tumor sample T-425, which gave no signal for either END or SIS peptides in three technical replicates, suggesting that the antibody-peptide binding had been disrupted due to unknown matrix effects.

Furthermore, the FFPE tumor sample T-532 could not be analyzed for AKT2 due to the low extraction yield (see Figure 30).

Linear regression analysis indicated that the protein expression levels for FFPE and flash-frozen tissues showed no correlation, with R^2 values of 0.01 for AKT1 (Figure 31A), and 0.22 for AKT2 (Figure 31B). Furthermore, 5 of the 6 samples analyzed for AKT1 and 4 of the 4 samples analyzed for AKT2 showed higher protein expression levels when measured from flash-frozen tissue, ranging from 2.1-fold to 5.3-fold higher (Figure 31C). In contrast, 1 of the 6 samples analyzed for AKT1 (T-425, breast surgery) showed 1.4-fold higher protein expression levels when analyzed from FFPE. Furthermore, while the dephosphorylation control (*E. coli* lysate spiked with synthetic pS473-AKT1 and pS474-AKT2 NAT peptides) was positive, only one sample (P918, from FFPE), resulted in an AKT1 PS above the cut-off value of 22%, with a PS value of 41% (Figure 31D).

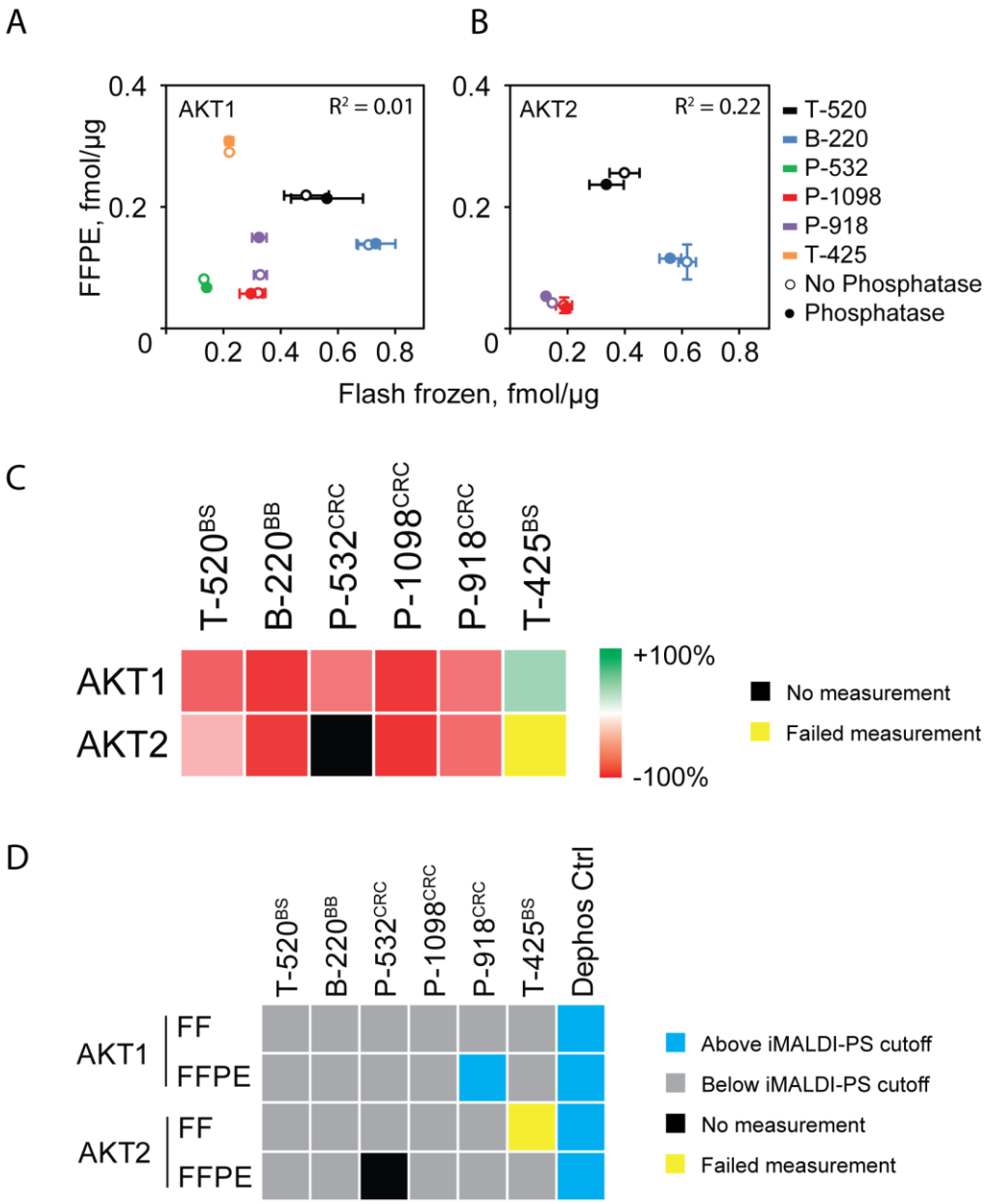

Figure 31: Comparison of six matched flash-frozen and FFPE tissues. Correlation of (A) AKT1 and (B) AKT2 protein concentrations. (C) Protein expression differences of FFPE compared to flash-frozen tissue. (D) Phosphorylation stoichiometry analysis. FF: flash frozen; FFPE: formalin-fixed paraffin embedded; P-: no dephosphorylation; P+: dephosphorylation; PS: phosphorylation stoichiometry

The general trend of lower AKT1 and AKT2 concentrations quantified from FFPE tissues could be caused by a variety of reasons. First, the preparation of FFPE tissues covalently links amino acid residues, DNA, and RNA within the tissues. These cross-links need to be reversed prior to iMALDI analysis, and reversal may not be 100% efficient. Furthermore, the recoveries of the protein-extraction protocol may differ between the FFPE and flash-frozen extractions and therefore lead to apparent differences in AKT1 and AKT2 expression levels. For instance, the mortar and pestle approach for breaking up FFPE cores used in this thesis project may not be ideal, and other methodologies such as a hand-held tissue blade blender might be more efficient. However, it should be noted that -- prior to choosing the mortar and pestle approach -- a Retsch bead grinder was evaluated and found to result in poorer homogenization than the mortar and pestle. Also, while the literature suggests that protein and peptide yields, as well as the number of protein identifications from both sample types, can be comparable on a global level (Ostasiewicz et al., 2010), this particular publication also showed that single proteins extracted from FFPE and flash-frozen tissues had significant differences in the amount of protein quantitated. Therefore, the lower AKT1 and AKT2 levels quantified from FFPE samples may be due to a combination of poor total protein extraction efficiency, and, specifically, lower AKT1 and AKT2 extraction efficiency.

In addition, the BCA assay used to quantify the total protein amount in each sample may have introduced a bias. This could have been due to the fact that the protein extraction buffers for flash-frozen and FFPE samples were different, which could impact the BCA results. The extraction buffers use different reagents due to the need to break up the cross-links in the FFPE tissues. Initial trials using the extraction buffer recommended for protein extraction from flash-frozen tissues had shown very poor extraction yield when used for FFPE tissues in my early experiments (data not shown), so two different buffers were used for flash-frozen versus FFPE tissues.

Furthermore, variability due to protein degradation caused by prolonged storage is a possibility, but this is unlikely. The stability of flash-frozen tumor lysates, analyzed before and after storage for 9 months at -80 °C, was demonstrated by an excellent correlation with an R^2 value of 0.99 and a slope of 1.29 (Appendix Figure 3), therefore

protein degradation is an unlikely reason for the differences seen between FFPE and flash-frozen tissues. The slope of 1.29 can be explained by the analyses being performed on different Bruker Microflex instruments, which might have introduced a systematic shift due to differences in electronics as well as different laser and detector settings.

In conclusion, while AKT1 and AKT2 could be quantified from both FFPE and flash-frozen tissues, the poor correlation of protein concentrations suggests that results between samples can only be compared when one or the other sample type is used exclusively. To address this observed bias, the FFPE extraction protocol needs to be optimized in future experiments, and potential BCA-related protein quantity differences also need to be assessed.

3.3.8 *Normal vs. adjacent tumor tissues*

To determine whether the iMALDI assays were sensitive and precise enough to detect expression level and phosphorylation differences between tissue samples, which could be of particular interest for serial biopsies from the same patient, matched normal and adjacent tumor tissues were provided by the JGH as FFPE cores and were analyzed by iMALDI. The results were assessed for differences in protein expression and PS. Three of the samples analyzed were colorectal liver metastases, and the fourth sample was a surgical breast tissue. The tumor P-532 samples could not be analyzed for AKT2 due to the limited amount of sample available. The normal P-1098 sample was analyzed for AKT2, but was excluded from the comparison due to the poor spectral quality of all three technical replicates.

Protein expression values ranged from 0.06 to 0.31 fmol/µg for AKT1 (Figure 32A), and 0.03 to 0.13 fmol/µg for AKT2 (Figure 32B), covering an approximately 4-5 fold concentration range. In contrast, AKT1 and AKT2 quantified from normal tissues fell within a concentration range of 0.06 to 0.10 fmol/µg for AKT1, and 0.04 to 0.09 fmol/µg for AKT2. This 2-fold concentration range suggests that the concentrations of AKT1 and AKT2 are tightly regulated in normal tissues.

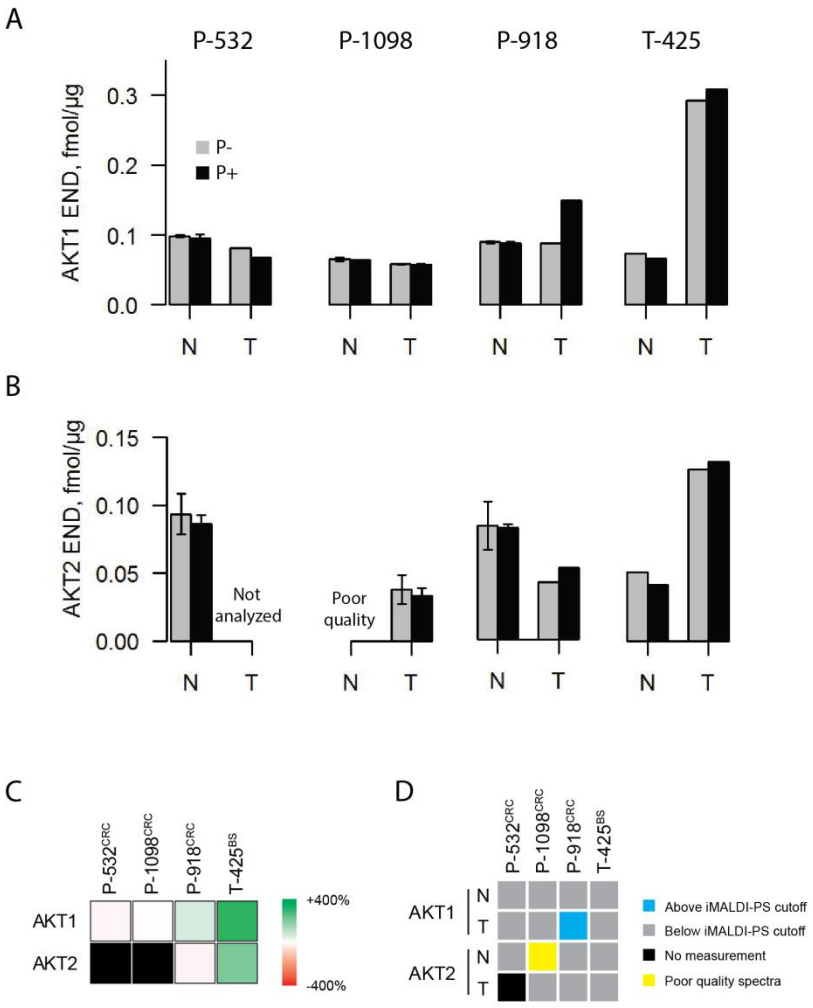

Figure 32: Comparison of normal and adjacent tumor tissues. (A) AKT1 and (B) AKT2 protein expression values for four normal and adjacent tumor tissues. (C) Expression level percent differences for tumor compared to adjacent normal tissue, and (D) phosphorylation stoichiometry. Samples P-352, P-1098, and P-918 were from colorectal cancer patients. Sample T-425 was a surgical breast tissue. N = normal tissue; T = tumor tissue; P-: no dephosphorylation; P+: dephosphorylated aliquot.

Figure 32C shows a comparison of the protein expression values obtained from tumor tissues compared to the adjacent normal tissues. While samples P-532 and P-1098 resulted in similar AKT1 expression levels in normal and tumor tissues, the tumor

samples P-918 and T-425 showed 1.5-fold and 3-fold elevated AKT1 expression levels compared to normal tissues, respectively.

The comparable levels between normal and tumor tissue for samples P-532 and P-1098 could be explained by the low tumor cellularity (only 25% and 70%, respectively (see Appendix Table 1)) and highlights the importance of histopathological tissue quality assessment.

Additionally, the T-425 tumor sample showed elevated AKT2 compared to the normal tissue, whereas sample P-918 had similar AKT2 expression levels in the tumor and normal tissues. Furthermore, as already noted in Figure 31, the P-918 tumor showed an AKT1 PS above the cut-off value of 22%, whereas none of the other samples did (Figure 32D).

The AKT1 and AKT2 expression levels and the PS variability between the samples could indicate a variety of things. First, the measured protein quantities are influenced by the tumor cellularity, as mentioned above, and therefore could vary due to varying tumor cellularity values (Appendix Table 1). However, it is also important to note that tumors are heterogeneous, with sub-populations of different cancer cells, normal tissue cells, and immune cells, which contribute to the final protein amounts quantified in varying degrees. In addition, the cell-cycle state further influences the protein expression and activation, adding to the variability of protein amounts in a tissue (K. Sharma et al., 2014). Furthermore, the varying protein concentrations and phosphorylation levels might indicate that the growth of the corresponding tumors may be influenced by the AKT1 and AKT2 signaling to varying degrees and could potentially be driven by additional cell-signaling nodes. It would also be interesting to confirm a link between AKT1 and AKT2 expression and PS and metastatic potential in a follow-up study, since Riggio et al. showed that elevated AKT1 and AKT2 expression levels contribute differently to tumor evolution. While AKT1 promotes localized tumor growth via S6 and cyclin D1 upregulation, AKT2 is involved in cell migration and invasion, thereby favoring metastasis through F-actin and vimentin induction, and has a poorer prognostic value than AKT1 (Riggio et al., 2017).

Although upfront sample considerations are important and need to be considered, the question behind this experiment has been answered, and I am able to conclude that the iMALDI assays developed are indeed sensitive enough to detect expression-level differences between normal and tumor tissues, whereas the determination of the phosphorylation stoichiometry is still challenging.

3.4 Conclusion

In conclusion, iMALDI assays have been developed that allow the quantitation of AKT1 and AKT2 expression levels and the PS from only 50 µg of total tissue-lysate protein, with 10 µg total protein required per replicate capture. After optimizing digestion and dephosphorylation parameters as well as sensitivity, the assays were validated and found to meet the FDA guidelines for linear range, analytical accuracy, and interferences. It was further confirmed that the phosphorylation sites in the target peptides did not reduce the digestion efficiency. Furthermore, PS cut-off values based on measurement errors were established to allow for the confident determination of the PS. The assays have been shown to be applicable to cell lines and flash-frozen tumor lysates as well as FFPE tissue lysates, with (on average) higher AKT1 and AKT2 levels measured from flash-frozen samples. In most cases, however, the PS measurements were below the determined cutoffs, indicating that the PPQ approach as it is currently used may not be sensitive enough to quantify the phosphorylation levels of target peptides in most samples. Finally, it has been demonstrated that the assays are sensitive and precise enough to detect differences between normal and adjacent tumor tissue, which will be important for future analyses of serial biopsies from the same patient.

Overall, the suitability of the assays for analysis of cancer-tissue lysates has been demonstrated and allowed me to move forward to the final experiment, which focused on answering the original hypothesis which was the existence of a strong correlation between PI3K/AKT/mTOR signaling pathway activity and patient response to targeted therapies.

Chapter 4: Correlation of PI3K/AKT/mTOR pathway activity and response with drug treatment in PDX mouse models

A manuscript based on this chapter is currently in preparation.

4.1 Introduction

To answer the main hypothesis of this thesis project, which was to determine whether there is a significant correlation between the PI3K/AKT/mTOR activity and response to drug treatment, a drug study involving patient-derived xenograft (PDX) mouse models was performed. Tumor size measurements were utilized as indicators of treatment response, and AKT1/AKT2 concentration and phosphorylation stoichiometry measurements were used as proxies for pathway activity.

The decision to use PDX models rather than other sample types such as human patient tumors or cancer cells treated with drugs was based on several factors.

First, while human tumor samples from a well-designed drug trial collected prior to, during and after treatment would have been the ideal choice, these samples were difficult to obtain. The sample type closest to treated patient tumors was PDX model tumors. PDXs have become an important tool for translational research and promise a more personalized approach to patient care. Compared to other types of models, including transgenic mice and patient-derived cell lines, PDX models have several distinct advantages (Whittle et al., 2015). For example, passing cell lines between mice results in clonal selection and loss of heterogeneity (L. M. Ellis and Fidler, 2010; Gillet et al., 2011), and has been shown to result in a poor correlation between clinical outcome and *in-vitro* and *in-vivo* data (Johnson et al., 2001). In contrast, PDX models do not undergo the high selection pressure of cell lines and maintain the initial tumor's sub-clones more effectively. Additionally, PDXs show stable genomes and patterns of protein expression between passages, which is important considering the necessity of passing tumors

between generations of mice to expand the tumor size and assess different drug treatments (DeRose et al., 2011; X. M. Zhang et al., 2013).

In conclusion, PDX model tissues were considered the most suitable compromise to answer the central hypothesis of this project.

4.2 Materials and Methods

4.2.1 *Experimental Design*

The study design to address the central hypothesis is shown in Figure 33. Briefly, PDX models were generated at the JGH by implanting pieces of a Herceptin-resistant, HER2-positive gastric-cancer tumor into four groups of mice which were treated with different drugs for 41 days. The first group received no drug (vehicle, V) and served as the baseline for both tumor size change and protein measurements. The second group was treated with Herceptin. Group 3 was treated with Everolimus, an mTORC1 inhibitor, which has been found to be beneficial in treating patients with advanced breast cancer which is resistant to endocrine therapies (Baselga et al., 2012). The fourth group was treated with a combination of Everolimus and Herceptin (E+H). During drug treatment, the tumor size changes were monitored by caliper measurements. The tumor sizes measured directly prior to tumor extraction, on day 41 of drug treatment, was used to assess the correlation of the tumor size changes with AKT1/2 protein expression levels and phosphorylation stoichiometry measurements, measured by iMALDI and western blot.

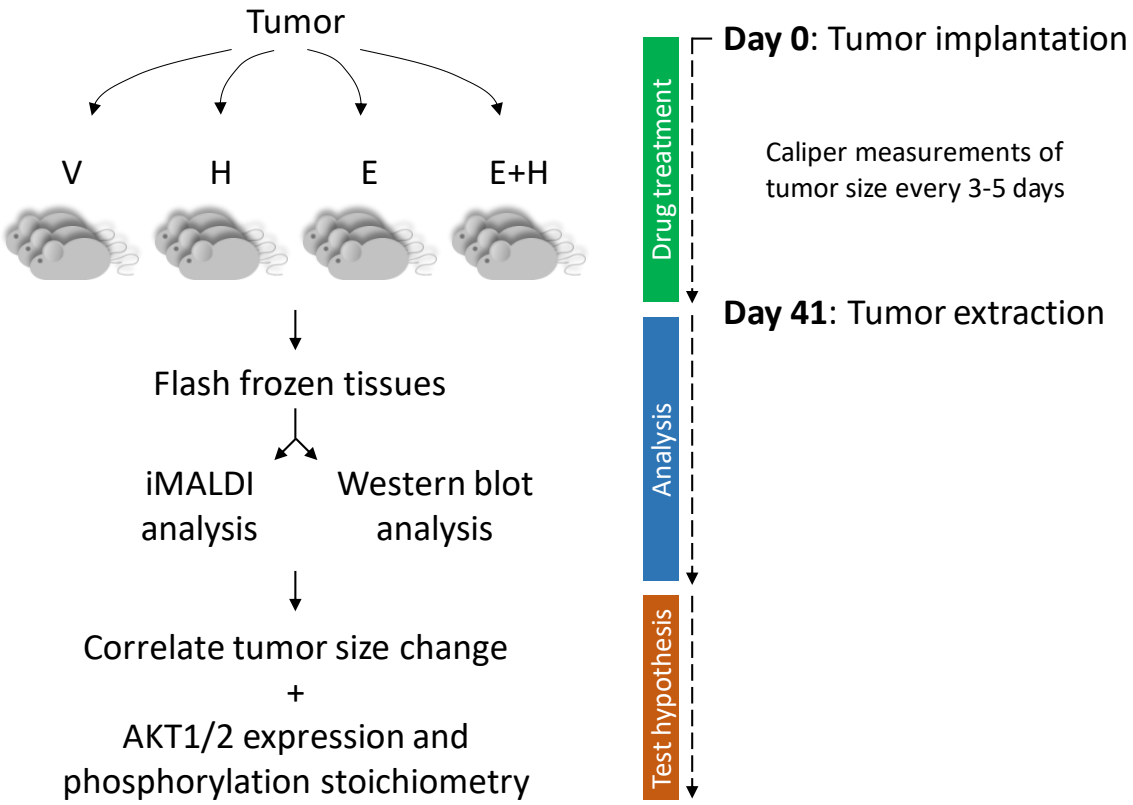

Figure 33: Experimental design to test the hypothesis using PDX models. Upon implantation of a Herceptin-resistant, HER2-positive gastric tumor pieces into twelve NOG mice (day 0), drug treatment was initiated with either no drug (V, vehicle), Herceptin (H), Everolimus (E), or a combination of Everolimus and Herceptin (E+H). Caliper measurements of the tumor size were recorded every 3-5 days. On day 41 of treatment, the mice were sacrificed, and the tumors were extracted and stored as flash frozen tissues to be analyzed by iMALDI and western blot analysis for AKT1 and AKT2 expression and phosphorylation stoichiometry. To answer the hypothesis, the data were assessed for a correlation between tumor size change and protein measurements.

4.2.2 *PDX samples*

The PDX samples used for the iMALDI analyses were provided by my collaborators at the JGH and consisted of 12 tissue lysates of gastric-cancer patient-derived PDX tumors

treated with Herceptin, Everolimus, E+H, or no treatment (n=3 per treatment). The mice used were of the NOG type, which is a severely immuno-deficient mouse model, which can result in improved engraftment rates (Whittle et al., 2015).

The samples used for iMALDI analysis belonged to "Drug Study #3" (Figure 34) and were part of a larger mouse study performed at the JGH (Ethics Protocol 14-168: Generation of Patient Derived Xenografts to Improve Breast Cancer Treatment), as explained below.

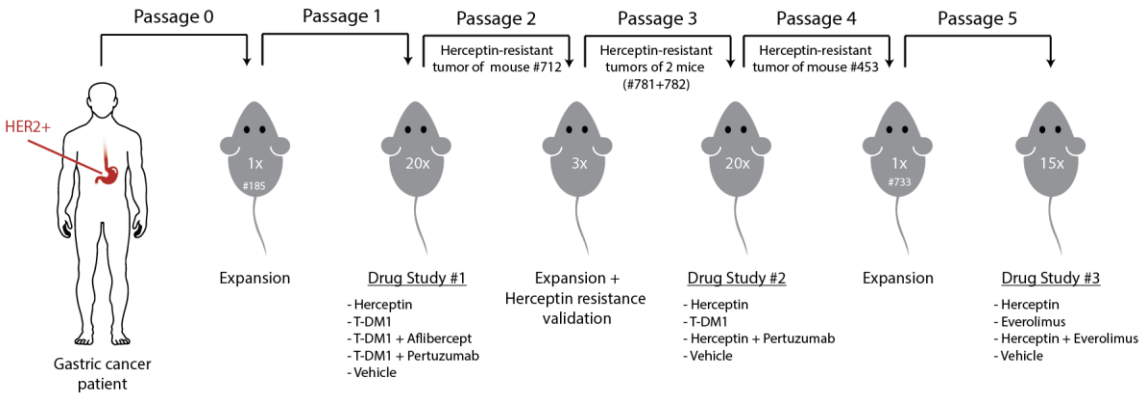

Figure 34: Overview of PDX drug study based on a HER2+, Herceptin-resistant tumor from a gastric cancer patient. Following several rounds of expansion and two drug studies, twelve samples from "Drug Study #3" were provided for iMALDI analysis, with mice treated with Herceptin, Everolimus, a combination of Everolimus and Herceptin, or no drug. The number of mice involved in each passage are indicated by "…x".

Briefly, a gastric-cancer patient's HER2-positive tumor was extracted and expanded in a single mouse (#185). The tumor was extracted and validated for HER2 expression via immunohistochemistry and western blot (data not shown) and passed on to 20 mice which were treated with Herceptin, T-DM1, a combination of T-DM1 and Aflibercept, a combination of T-DM1 and Pertuzumab, or no treatment ("Drug Study 1"). T-DM1 is an antibody-drug conjugate consisting of a monoclonal antibody (Herceptin) linked to the cytotoxic drug emtansine (DM1). Three of the Herceptin-treated mice responded to the

treatment, while one mouse failed to respond (#712). Illumina MiSEQ analysis of tumors from mice #185 and #712 had been performed to confirm that the identified mutations were carried forward into the next mouse. The tumor of mouse #712 was extracted and passed on to three new mice. One mouse was used to validate Herceptin-resistance, and the other two mice were used for expansion (#781 and #782). The tumors of #781 and #782 were transferred to 20 new mice which were treated with Herceptin, T-DM1, a combination of Herceptin and Pertuzumab, or no treatment ("Drug Study 2"). One mouse showed the development of Herceptin-resistance after rapid tumor growth towards the end of the 79 days of treatment, and the tumor was extracted and expanded in a new mouse (#733).

After extraction, the tumor was passed on to 15 new mice for "Drug Study 3" which treated four groups of mice with Herceptin, Everolimus, E+H, or without drug for 41 days. Tumor-size measurements were taken by caliper every 3-5 days. On treatment day 41, the tumors were extracted, embedded in optimal cutting temperature (OCT) compound, and one H&E slide was verified by a pathologist to confirm tumor cellularity. Flash-frozen tissue lysates were prepared, and samples of three mice per treatment group were sent to Victoria for iMALDI analysis.

4.2.3 *Western blot analysis*

Western blot analyses were performed at the JGH for pS473-AKT1 and pS474-AKT2 expression. Quantitative values for the pS473-AKT1 and pS474-AKT2 expression were determined in Victoria by calculating the densitometry ratio of the pAKT bands and the corresponding ß-actin loading controls using ImageJ software and Microsoft Excel.

4.2.4 *iMALDI analysis*

iMALDI analysis was performed as described in section 3.2.9. The concentrations of the phosphorylated AKT1 and AKT2 peptides were calculated by multiplying the PS of the sample by the corresponding protein concentration quantified after dephosphorylation.

4.2.5 *Z-score calculation*

Furthermore, data sets were converted to z-scores for data normalization according to the following equation:

$$z = \frac{x - \mu}{\sigma} \tag{4}$$

with z being the z-score, x being the measurement value, and μ and σ being the mean and standard deviation of the dataset, respectively.

4.3 Results and Discussion

4.3.1 *Responses to treatment*

After 41 days of treatment, all mice in the vehicle, Herceptin, and Everolimus groups (9/12) showed progressive disease (PD), as determined by assigning tumor-size changes to progression categories following the RECIST criteria (Eisenhauer et al., 2009), with tumor-size increases ranging between 1.3- and 9.2-fold (Figure 35). In contrast, the E+H treatment resulted in two mice exhibiting stable disease (SD), with tumor-size changes ranging between 1.0 and 1.2-fold, and one mouse showing a partial response (PR), with a tumor size decrease of 42%. The findings of progressive disease in the vehicle and the Herceptin groups were expected due to the absence of treatment in the vehicle group, and the resistance to Herceptin demonstrated in tumors of previous passages. Interestingly, treatment with the mTORC1-inhibitor Everolimus alone did not manage to reduce or stabilize tumor growth, while combining Everolimus with Herceptin did, even though the tumors had been shown to be resistant to Herceptin treatment alone. This suggested that different sub-populations of cancer cells with differential responses to Everolimus and Herceptin may have existed within the tumors, and the combination approach was effective enough to result in stabilization of the tumor-size or even shrinkage.

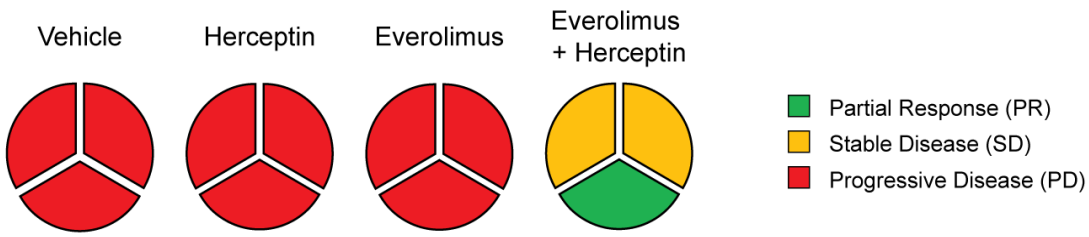

Figure 35: Treatment outcomes for the vehicle, Herceptin, Everolimus, and Everolimus + Herceptin combination groups evaluated following the RECIST guidelines (Eisenhauer et al., 2009).

4.3.2 *AKT1/AKT2 expression levels*

The AKT1 and AKT2 expression levels in all twelve samples were able to be quantified by iMALDI (Figure 36). The median concentrations across each treatment group were comparable, ranging from 0.31 to 0.42 fmol/µg for AKT1, and 0.20 and 0.29 fmol/µg for AKT2. While all four treatment groups showed a similar concentration spread for AKT2, the AKT1 concentration range for the Everolimus and E+H treatment showed a larger distribution than the vehicle and Herceptin groups. This suggests that Everolimus and the E+H treatment may have a regulatory impact on the expression and/or degradation rate of AKT1. However, because of the overlap of protein concentrations between treatments, and the limited number of samples, it is not possible to make a definitive statement about this impact. Interestingly, the partial response sample showed AKT1 and AKT2 concentrations at the high end of the protein-expression distributions, which could be a sign of the development of a resistance mechanism and it may be the case that a treatment time-frame longer than 41 days may have resulted in progressive disease rather than a partial response.

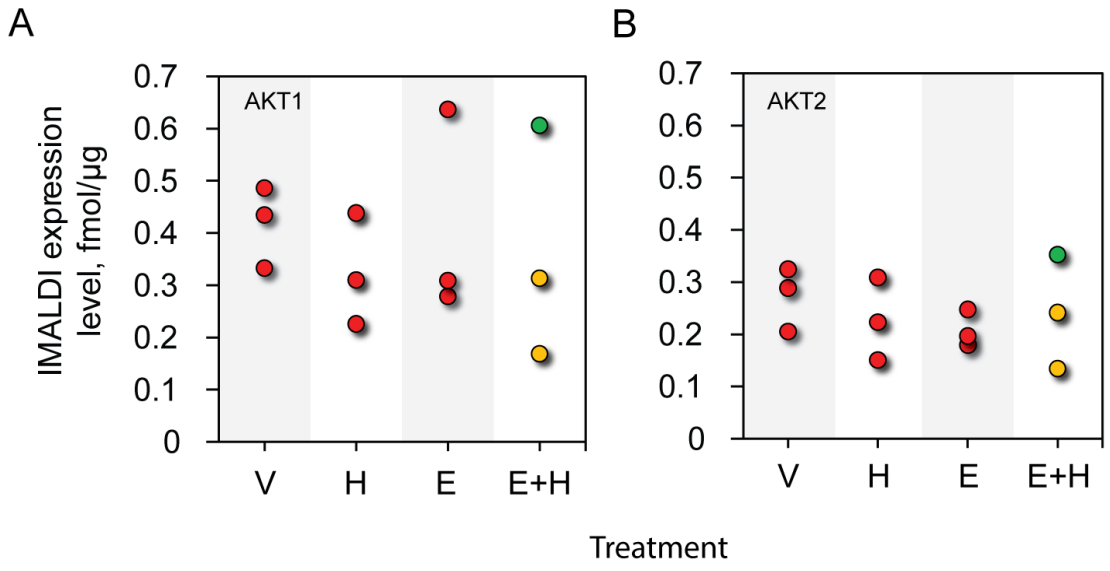

Figure 36: Expression levels quantified by iMALDI for (A) AKT1 and (B) AKT2. V: vehicle. H: Herceptin. E: Everolimus. E+H: combination of Everolimus and Herceptin

4.3.3 *iMALDI results for AKT1/AKT2 phosphorylation stoichiometries*

Of the twelve samples analyzed, only two gave AKT1 phosphorylation stoichiometries above the cut-off value of 22%, and no AKT2 PS values were found to be above the AKT2 cut-off value of 26% (see section 3.3.5 for cut-off details). Since the actual concentration of phosphopeptides present in the samples has more informative valuable than PS alone, the concentrations were calculated by multiplying the PS values and the corresponding AKT1 and AKT2 expression values shown in Figure 36. The resulting AKT1 and AKT2 phosphopeptide concentrations are shown in Figure 37.

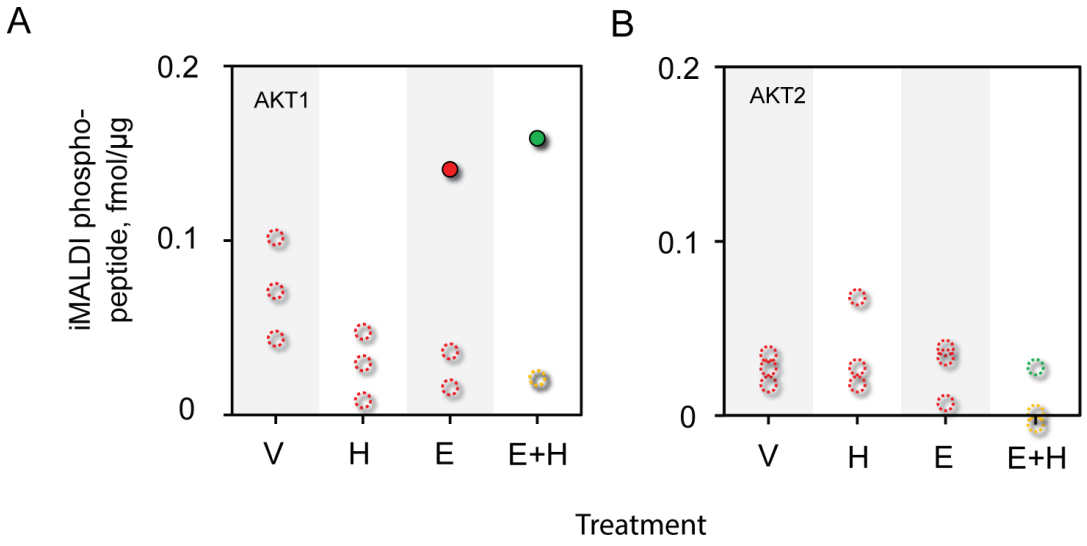

Figure 37: (A) AKT1 and (B) AKT2 phosphopeptide concentrations determined by iMALDI. Full circles: concentrations calculated with phosphorylation stoichiometry values above cut-off. Empty circles: concentrations calculated with phosphorylation stoichiometry values below cut-off, and therefore of lower confidence. V: vehicle. H: Herceptin. E: Everolimus. E+H: combination of Everolimus and Herceptin

Interestingly, the partial-response sample from the E+H treatment group showed the highest concentration of phosphorylated AKT1 peptide, followed by a progressive disease sample from the Everolimus group (Figure 37A), indicating an activated pathway. This could be explained by AKT activation via a negative feedback loop caused by treatment with Everolimus, which has been shown to be linked to mTORC1 inhibition-dependent induction of insulin receptor substrate-1 expression and thus AKT activation (Julien et al., 2010; O'Reilly et al., 2006), and this could indicate the onset of resistance.

Despite these findings, the limited number of phosphopeptide concentrations confidently determined make it difficult to find a correlation to treatment responses. This suggests that the dephosphorylation approach coupled with iMALDI may not be the most suitable approach, at least with the current performance measures, and improvements could be made in follow-up experiments. For instance, larger sample amounts and therefore

stronger signals could improve precision and therefore lower the acceptable PS cut-off. Alternatively, a different approach analyzing phosphorylated peptides directly without dephosphorylation, either with or without enrichment, could be assessed in more detail. However, multiple phosphorylation sites in both the AKT1 and AKT2 target peptides make this approach difficult.

Being able to quantify low phosphorylation stoichiometries is important considering that even at low levels, the phosphorylation can have regulatory relevance, as discussed by Olsen et al. (Olsen et al., 2010) and demonstrated by Sharma et al., who showed that the majority of proteins observed in HeLa cells with or without EGF-stimulation exhibit phosphorylation stoichiometries <25% (K. Sharma et al., 2014). Therefore, the AKT1 and AKT2 phosphorylation stoichiometries below the quantifiable cut-off values may still be relevant to downstream signaling, and the data presented here is limited to assess a correlation between signaling pathway activity and tumor size changes.

4.3.4 *Western blot results for AKT1/AKT2 phosphopeptides*

While the iMALDI PS results only yielded limited information regarding the abundance of the phosphorylated AKT1 and AKT2 target peptides, western blot analysis allowed a relative comparison of all twelve samples (Figure 38).

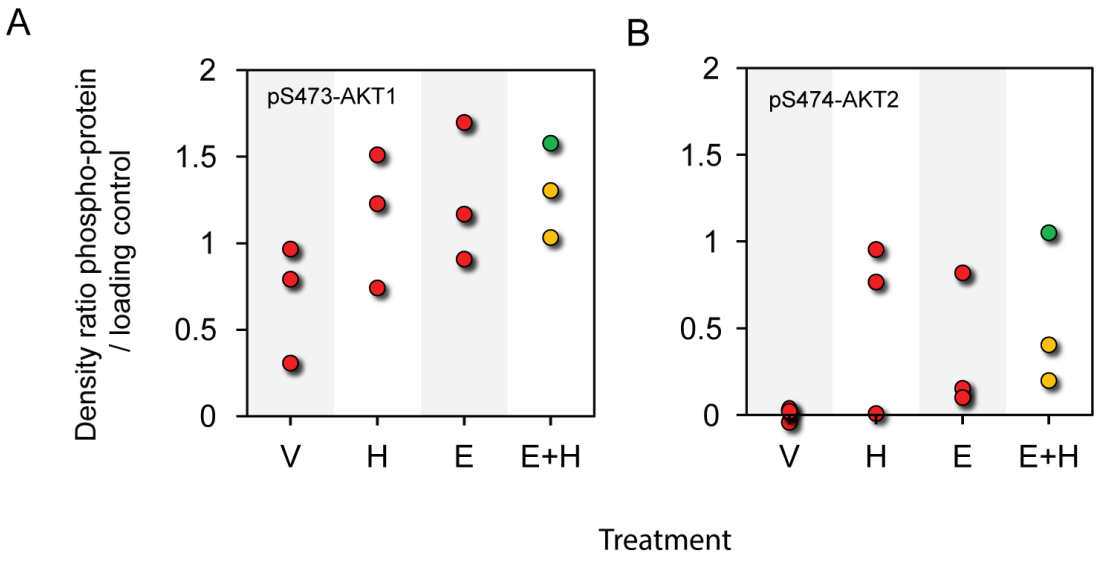

Figure 38: Western blot density ratios of (A) pS473-AKT1 and (B) pS474-AKT2 to loading control. V: vehicle. H: Herceptin. E: Everolimus. E+H: combination of Everolimus and Herceptin

Interestingly, the vehicle group showed the lowest median pS473-AKT1 and pS474-AKT2 abundances. In contrast, the pS473-AKT1 levels for the Herceptin, Everolimus, and E+H treatment groups showed approximately two-fold higher median concentrations, with a similar spread in each treatment group (Figure 38A). Intriguingly, the pS474-AKT2 values for all three biological replicates of the vehicle group were approximately 0 for the western blot band density ratio of phosphoprotein over loading control (Figure 38B). One could infer that the vehicle group's tumors may only have a limited or no metastatic potential, as AKT2 has been described as the only isoform responsible for promoting cell metastasis (Riggio et al., 2017).

Additionally, the Herceptin, Everolimus, and combined E+H group showed large within-group variability for pS474-AKT2, with a similar concentration spread, and the lowest values being close to 0 for the phosphoprotein/loading control density ratio (Figure 38B), again making it difficult to correlate phospho-protein expression to tumor size change at this small sample size. However, an interesting observation was that the partial response sample from the E+H combination treatment had among the highest pS473-AKT1 and

pS474-AKT2 amounts, indicating an activated pathway and potentially the onset of resistance.

While the western blot data complemented the iMALDI phosphorylation stoichiometry data, it is imported to point out its limitations, namely the potential of cross-reactivity of the antibodies, and semi-quantitativeness of western blots.

4.3.5 *Integration of measurements*

To examine the data for patterns, all the quantitative iMALDI and western blot results were normalized to z-scores and plotted as a heat map (Figure 39). While the AKT1 and AKT2 expression levels varied within all treatment groups, the vehicle group was characterized by very low pS473-AKT1 and pS474-AKT2 expression levels, as determined by western blot. In contrast, the other treatment groups showed variable pS473-AKT1 and pS474-AKT2 expression between and within groups. As mentioned above, two samples stood out due to elevated AKT1 and AKT2 expression levels as well as elevated pS473-AKT1 and pS474-AKT2 expression levels and were found in the Everolimus and the E+H treatment group. While these findings seem promising and may indicate that the molecular profiles related to the PI3K/AKT/mTOR pathway could be linked to treatment outcome, more samples would need to be evaluated in a follow-up study to draw firm conclusions.

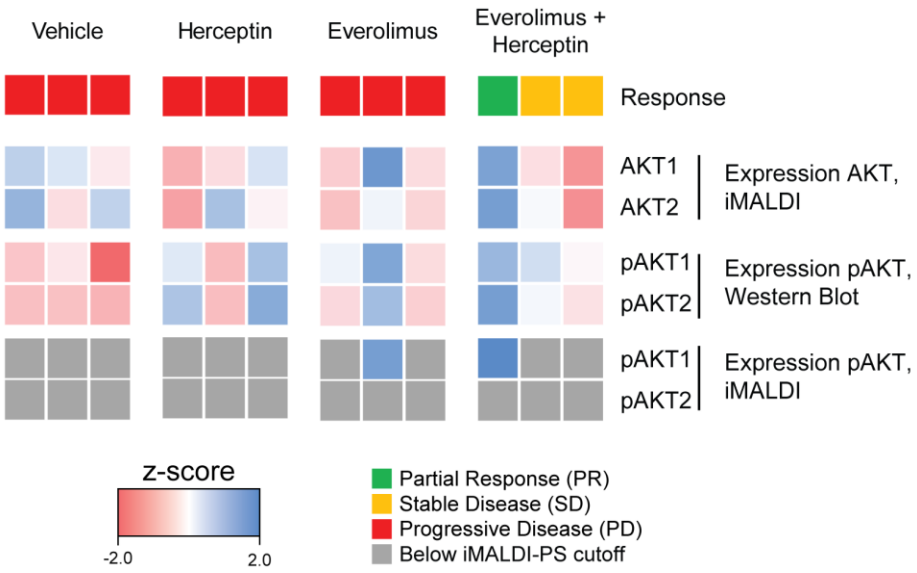

Figure 39: AKT1/2 expression data measured by iMALDI and western blot for twelve gastric cancer PDX tumors treated with Herceptin, Everolimus, a combination of Everolimus and Herceptin, or no drug.

The large within-group variability observed could be due to a variety of reasons. First, the mice used for this drug study received fragments of the same tumor, which is a common practice in generating PDX models (Whittle et al., 2015). This practice is limiting in that different pieces of the same tumor are likely heterogeneous, consisting of different sub-populations with distinct molecular profiles. To address this issue, it could be feasible to repeat a follow-up drug study with a homogenized tumor cell suspension to ensure homogenous distribution of sub-populations in all mice. A potential issue of this approach, however, would be the destruction of tumor architecture and tumor microenvironment, which may be crucial to maintaining comparable drug response of the initial patient tumor and the PDX tumor.

Another reason for the large within-group variability could be the development of resistance mechanisms, potentially due to the upregulation of alternative pathways, or due to the introduction of novel mutations in subclones of the cell mass. However, the high degree of mutational stability between passages in PDX models has been

documented (DeRose et al., 2011; X. M. Zhang et al., 2013), and has been confirmed for tumors of mice #185 and #712 from passage 1 (see Figure 34) via targeted MiSEQ analysis, and is therefore not likely to be the reason for the observed variability.

Also, the tumor environment in each of the mice could contribute to variability in the quantitative results. However, since the NOG mice are heavily immuno-compromised, this is less likely.

4.3.6 *Limitations of the study design and data*

While the data collected showed interesting molecular differences between samples which could potentially be linked to treatment response, both the data and study design limit the ability to answer the hypothesis with confidence (i.e. is there a strong correlation between PI3K/AKT/mTOR pathway activity and treatment response). This section aims at pointing out those weaknesses and suggesting possible solutions, but also potential pitfalls, to overcome the limitations.

In terms of study design, one critical point is that the tissue samples were PDX-derived tumors rather than tumors directly extracted from human patients. While PDX mouse models are superior to other types of mouse model tumors generated from cell line, as discussed in section 4.1, the engraftment process, while maintaining the histological integrity of the tumor, introduces the tumor to a new environment, potentially altering the tumor. For instance, tumors successfully engrafted may represent more aggressive forms of the disease (Pergolini et al., 2017).

Another limitation of the study design was that all tumor samples were taken after 41 days of treatment (or no treatment in case of the vehicle group), which represents a snapshot in time rather than a progression of time points. A more promising approach would have been to take serial biopsies prior to, during, and after treatment. A “before treatment”-sample could also show any variability between mouse tumors potentially caused by heterogeneity of the implanted tumor fragments. However, serial biopsy samples were not available and are difficult to obtain due to the risk of complications.

Additionally, normal tissue adjacent to the tumor tissues should have been collected as a baseline control for protein expression and phosphorylation stoichiometry measurements.

Another limitation of this pilot study was the low number of samples available (n=3 per treatment), which does not allow statistical approaches to be used effectively. Increasing the number of mice would improve the statistical power, but the high cost per mouse and treatment are prohibitive.

Furthermore, this study assumes that the AKT1/2 protein expression and phosphorylation stoichiometry are suitable proxies for PI3K/AKT/mTOR pathway activity. However, due to the complexity of cell signaling with varying signaling nodes interconnected at different levels between signal input at the cell membrane to transcription factors resulting in initiating DNA transcription in the nucleus, signaling proteins at varying signaling nodes, including members of relevant known feedback pathways, should be assessed for expression levels and PTMs.

In terms of data limitations, the large spread of measurements within and between treatment groups prohibits deriving firm conclusions from linking expression levels to treatment outcome, particularly at the small sample sizes. Additionally, only 2/12 samples analyzed by iMALDI resulted in confident PS values for AKT1, and none for AKT2. However, low PS may still have regulatory relevance to influence the cell phenotype and response to treatment. While western blot analysis did reveal phosphorylation measurements for all twelve samples, its potential for cross-reactivity make this method of choice less ideal. An alternative methodology to confirm iMALDI results for future experiments could be MRM by directly monitoring peptides with single and multiple phosphorylation sites. To overcome possible sensitivity issues, which would be more prevalent for multiply phosphorylated peptides due to their lower abundance, phosphopeptide enrichment could be performed with Ti^{4+}-IMAC, as has been shown by other groups before (de Graaf et al., 2015).

Another limitation of the data presented here is that the PS values represent the overall phosphorylation amounts for the entire peptide due to the phosphatase-induced removal of all peptide phosphate groups. This could be problematic if the peptide of interest has

multiple phosphorylation sites, as is the case for the C-terminal tryptic AKT1 and AKT2 peptides targeted in this thesis. Proteins are known to be phosphorylated on different residues by different kinases as a way of modulating the signal transduction from different inputs (S. J. Humphrey et al., 2015a), and some of the phosphorylation sites may act in an inhibitory rather than stimulatory fashion towards downstream signaling (Chow et al., 2011). Therefore, the removal of multiple phosphorylation groups resulting in a single PS measurement could mask the regulatory role of some of the underlying phosphorylation events and overestimate or skew the interpretation of the stimulatory effect.

4.4 Conclusion

In conclusion, while the results are intriguing and may indicate that the PI3K/AKT/mTOR signaling pathway activity, as measured by AKT1 and AKT2 expression and phosphorylation levels, could be linked to treatment outcome, the overlapping values between treatment groups, the large spread within groups, the low number of biological replicates, as well as limitations in the experimental design made it difficult to confirm a correlation, and future studies are required.

Chapter 5: Future steps for iMALDI and cancer treatment

This chapter discusses the steps going forward, the next steps for iMALDI and its potential impact on future cancer treatment, while considering the limitations of the present study.

In this thesis work, the first sub-project confirmed that the iMALDI methodology can be automated and shows characteristics suitable for clinical implementation (chapter 2), and could be applied to answer the central hypothesis discussed below. Due to it being one of the most commonly dysregulated pathways in cancer (Ciriello et al., 2013), the PI3K/AKT/mTOR pathway was chosen as the model pathway to investigate in this thesis project, using AKT1 and AKT2 as proxies for pathway activation. Therefore, in a next step, iMALDI assays for the quantitation of AKT1 and AKT2 expression levels and phosphorylation stoichiometry of the C-terminal tryptic peptides were analytically validated and were shown to reliably measure protein concentrations from cell lines, flash frozen and FFPE tissue samples (chapter 3). In the final data chapter (chapter 4), the hypothesis of a strong correlation between PI3K/AKT/mTOR signaling pathway activity and patient response could only be partially answered, and hints of high AKT1/2 expression and phosphorylation and partial response were intriguing. In the future, follow-up work will be required to obtain a confident answer, and the limitations of the presented thesis work need to be addressed.

As discussed in chapter 4, these limitations include the use of PDX tumors rather than tumors directly obtained from human patients. Additionally, the tumor samples analyzed were obtained after treatment only. To improve upon this, serial biopsies collected prior to, during and after treatment would greatly improve the informative value. Furthermore, normal tissues should be collected to provide baseline measurements which could be compared to the tumor analysis results. Moreover, the number of samples in this study was restricted to three biological replicates per drug treatment. A larger number of samples would improve the statistical power of the results and possibly allow determining significant differences between treatments.

Another limitation of the study was that only AKT1 and AKT2 were assessed as proxies for PI3K/AKT/mTOR pathway activity -- in particular their C-terminal tryptic peptides encompassing the conserved S473 phosphorylation site. This is limiting in three ways. First, AKT has phosphorylation sites distant from the C-terminus which contribute to AKT activation and could result in an activated pathway, such as T308 or Y176 (Mahajan et al., 2010), and these should be considered as targets in future assay development. Second, AKT1 has five and AKT2 four phosphorylation sites on their respective C-terminal tryptic peptides. While AKT1-S473 and AKT2-S474 are the major phosphorylation sites known to be required for full kinase activation, the other phosphorylation sites most likely have regulatory relevance as well. Therefore, the dephosphorylation approach in this thesis project which removes the phosphatase groups of the target peptides thereby results in loss of this site-specific information, and alternative methodologies could be used to address this (discussed below). Third, cell signaling is a complex process with compensatory pathways and adaptation mechanisms to drug intervention (Sever and Brugge, 2015) which, supported by the research presented here, suggests that two proteins alone may not be sufficient to predict a patient's response to treatment. Instead, the analysis of several proteins known to be dysregulated in cancer should be analyzed and evaluated in conjunction. Ideally, these proteins cover different signaling nodes to obtain a more accurate picture of the cell signaling status and detect potential alternative mechanisms resulting in the formation of drug resistance. To achieve this goal, multiplexed iMALDI assays targeting additional proteins of representative nodes in the signaling network could be developed and evaluated for their predictive power.

Currently in development are iMALDI assays for PI3K p110α, EGFR, PTEN, and S6K, which are part of the PI3K/AKT/mTOR pathway, and therefore ideal to be measured in addition to AKT1 and AKT2. Furthermore, the isoform AKT3 will be added as an additional target due to the distinct tissue-specific, temporally-regulated and context-dependent AKT isoform functions (Yu et al., 2015). Additional signaling pathways of interest are the MAPK/ERK pathway, Wnt signaling pathway, DNA mismatch repair (BRCA1/BRCA2), chromatin organization, p53-mediated apoptosis, and mitosis-related

proteins such as Aurora A kinase due to their demonstrated involvement in cancer (Ciriello et al., 2013). Moreover, signaling pathways exploited by immunotherapies, such as the PD-1/PD-L1 axis and other immunosuppressive pathways (P. Sharma and Allison, 2015) are of key interest for the development of new iMALDI assays due to their high impact and great potential in resulting in significant and long-lasting responses from cancer patients.

Furthermore, while iMALDI was shown to provide precise and accurate concentration measurements of non-modified peptides, a significant portion of samples in this thesis project could not be assessed for PS by iMALDI with great confidence, and alternative methodologies could be investigated to quantify phosphorylation stoichiometries. For instance, while technologically more challenging, MRM or PRM-based MS linked to nano-LC separation for improved sensitivity could be used to quantify phosphorylated peptides directly, rather than dephosphorylating peptides, thus retaining site-specific information (de Graaf et al., 2015; Dekker et al., 2018). This would be especially important for target peptides harboring phosphate groups with opposing or varying roles to downstream signaling (i.e. inhibitory vs. stimulatory). Moreover, this approach could replace western blots in future experiments to validate the iMALDI quantitation results, thereby improving upon the potential cross-reactivity of western blots.

In addition, to make use of the complementary nature of different levels of information and to address the issue of the discrepancy between genome and phenotype resulting in false conclusions from molecular measurements on treatment decisions (Bai et al., 2012), integrating the protein measurements, mutational data, gene expression profiling data, epigenetic information, and metabolomics data is key (Alfaro et al., 2014). Integrated molecular signatures can then be used as features and evaluated in machine learning algorithms such as support vector machines or neural networks (Chaudharyl et al., 2018).

Another important aspect to address in the future is tumor heterogeneity, which has the potential to result in skewing protein measurements by combining protein levels from different cellular sub-populations. This is important not only for iMALDI, but any technique that analyses tissue lysates. To address this problem, upfront cell fractionation by methods such as fluorescence activated cell sorting (FACS) could be evaluated for

grouping the tumor cells into subpopulations (Barteneva et al., 2013) which could then be analyzed for protein expression, PTMs and other molecular species separately.

Overall, the benefits of biomarker analysis for patient stratification on clinical outcome have been demonstrated, and iMALDI is well positioned to contribute to the improved well-being of patients in the future.

Bibliography

Abbatiello, S. E., et al. (2015), 'Large-Scale Interlaboratory Study to Develop, Analytically Validate and Apply Highly Multiplexed, Quantitative Peptide Assays to Measure Cancer-Relevant Proteins in Plasma', *Molecular and Cellular Proteomics*, 14 (9), 2357-74.

Adamson, Peter C., et al. (2014), 'National Cancer Institute (NCI) TARGET: Therapeutically Applicable Research to Generate Effective Treatments', *Database of Genotypes and Phenotypes: dbGaP*.

Adonna, T. A., et al. (2009), 'Multi-site assessment of the precision and reproducibility of multiple reaction monitoring-based measurements of proteins in plasma', *Nat Biotech*, 27.

Aebersold, R. and Mann, M. (2016), 'Mass-spectrometric exploration of proteome structure and function', *Nature*, 537 (7620), 347-55.

Albertson, Donna G. and Pinkel, Daniel (2003), 'Genomic microarrays in human genetic disease and cancer', *Human Molecular Genetics*, 12 (suppl_2), R145-R52.

Alderman, Michael H., et al. (2004), 'Plasma renin activity levels in hypertensive persons: their wide range and lack of suppression in diabetic and in most elderly patients', *American Journal of Hypertension*, 17 (1), 1-7.

Alessi, D. R., et al. (1997), 'Characterization of a 3-phosphoinositide-dependent protein kinase which phosphorylates and activates protein kinase Balpha', *Curr Biol*, 7 (4), 261-9.

Alexander, Walter (2016), 'The Checkpoint Immunotherapy Revolution: What Started as a Trickle Has Become a Flood, Despite Some Daunting Adverse Effects; New Drugs, Indications, and Combinations Continue to Emerge', *Pharmacy and Therapeutics*, 41 (3), 185-91.

Alfaro, Javier A., et al. (2014), 'Onco-proteogenomics: cancer proteomics joins forces with genomics', *Nature Methods*, 11 (11), 1107-13.

Alsaab, Hashem O., et al. (2017), 'PD-1 and PD-L1 Checkpoint Signaling Inhibition for Cancer Immunotherapy: Mechanism, Combinations, and Clinical Outcome', *Frontiers in Pharmacology*, 8, 561.

American Cancer Society (2016a), 'Cancer Facts & Figures 2016', in American Cancer Society (ed.), (Atlanta).

American Cancer Society 'Chemotherapy Side Effects', <https://www.cancer.org/treatment/treatments-and-side-effects/treatment-types/chemotherapy/chemotherapy-side-effects.html>, accessed 01-May-2018.

Anand, P., et al. (2008), 'Cancer is a Preventable Disease that Requires Major Lifestyle Changes', *Pharmaceutical Research*, 25 (9), 2097-116.

Anderson, N. L., et al. (2004), 'Mass spectrometric quantitation of peptides and proteins using stable isotope standards and capture by anti-peptide antibodies (SISCAPA)', *Journal of Proteome Research*, 3 (2), 235-44.

Asangani, I. A., et al. (2007), 'MicroRNA-21 (miR-21) post-transcriptionally downregulates tumor suppressor Pdcd4 and stimulates invasion, intravasation and metastasis in colorectal cancer', *Oncogene*, 27 (15), 2128-36.

Atkinson, A. J., et al. (2001), 'Biomarkers and surrogate endpoints: Preferred definitions and conceptual framework', *Clinical Pharmacology & Therapeutics*, 69 (3), 89-95.

Atrih, A., et al. (2014), 'Quantitative proteomics in resected renal cancer tissue for biomarker discovery and profiling', *British Journal of Cancer*, 110 (6), 1622-33.

Atrih, Abdelmadjid, et al. (2009), 'Stoichiometric Quantification of Akt Phosphorylation Using LC-MS/MS', *Journal of Proteome Research*, 9 (2), 743-51.

Bai, Y., et al. (2012), 'Phosphoproteomics identifies driver tyrosine kinases in sarcoma cell lines and tumors', *Cancer Research*, 72 (10), 2501-11.

Barteneva, N. S., et al. (2013), 'Cell sorting in cancer research-Diminishing degree of cell heterogeneity', *Biochimica Et Biophysica Acta-Reviews on Cancer*, 1836 (1), 105-22.

Baselga, J., et al. (2012), 'Everolimus in Postmenopausal Hormone-Receptor-Positive Advanced Breast Cancer', *New England Journal of Medicine,* 366 (6), 520-29.

Becker, K. F. and Schott, C. (2011), *Protein Extraction from Formalin-Fixed Paraffin-Embedded Tissues*, ed. G. Stanta (Guidelines for Molecular Analysis in Archive Tissues; Berlin: Springer-Verlag Berlin) 245-48.

Berndt, N., Karim, R. M., and Schonbrunn, E. (2017), 'Advances of small molecule targeting of kinases', *Current Opinion in Chemical Biology,* 39, 126-32.

Bhavin Patel, et al. (2014), 'Enrichment of EGFR/PI3K/AKT/PTEN Proteins for Research using Immunoprecipitation and with Mass Spectrometry-based Analysis', *ASMS 2014* (Thermo Fisher Scientific).

Biotechnology Innovation Organization (2016), 'Clinical Development Success Rates 2006-2015', (Biotechnology Innovation Organization).

Blanco-Calvo, M., et al. (2015), 'Colorectal Cancer Classification and Cell Heterogeneity: A Systems Oncology Approach', *International Journal of Molecular Sciences,* 16 (6), 13610-32.

Boja, E. S. and Rodriguez, H. (2012), 'Mass spectrometry-based targeted quantitative proteomics: Achieving sensitive and reproducible detection of proteins', *Proteomics*, 12 (8), 1093-110.

Bozic, Ivana, et al. (2010), 'Accumulation of driver and passenger mutations during tumor progression', *Proceedings of the National Academy of Sciences of the United States of America,* 107 (43), 18545-50.

Brentjens, R. J., et al. (2007), 'Genetically targeted T cells eradicate systemic acute lymphoblastic leukemia xenografts', *Clinical Cancer Research*, 13 (18 Pt 1), 5426-35.

Cai, S. L., et al. (2006), 'Activity of TSC2 is inhibited by AKT-mediated phosphorylation and membrane partitioning', *Journal of Cell Biology,* 173 (2), 279-89.

Camenzind, A. G., et al. (2013), 'Development and evaluation of an immuno-MALDI (iMALDI) assay for angiotensin I and the diagnosis of secondary hypertension', *Clinical Proteomics,* 10 (1), 20.

Carracedo, Arkaitz, et al. (2008), 'Inhibition of mTORC1 leads to MAPK pathway activation through a PI3K-dependent feedback loop in human cancer', *The Journal of Clinical Investigation,* 118 (9), 3065-74.

Carter, S., et al. (2012), 'A liquid chromatography tandem mass spectrometry assay for plasma renin activity using online solid-phase extraction', *Annals of Clinical Biochemistry,* 49, 570-79.

Chaudharyl, K., et al. (2018), 'Deep Learning-Based Multi-Omics Integration Robustly Predicts Survival in Liver Cancer', *Clinical Cancer Research,* 24 (6), 1248-59.

Chen, Mo and Manley, James L. (2009), 'Mechanisms of alternative splicing regulation: insights from molecular and genomics approaches', *Nature Reviews. Molecular Cell biology*, 10 (11), 741-54.

Cheng, J. Q., et al. (1996), 'Amplification of AKT2 in human pancreatic cancer cells and inhibition of ATK2 expression and tumorigenicity by antisense RNA', *Proceedings of the National Academy of Sciences of the United States of America,* 93 (8), 3636-41.

Chow, Jeremy P. H., Poon, Randy Y. C., and Ma, Hoi Tang (2011), 'Inhibitory phosphorylation of cyclin-dependent kinase 1 as a compensatory mechanism for mitosis exit', *Molecular and cellular biology,* 31 (7), 1478-91.

Christakis, Panos (2011), 'The Birth of Chemotherapy at Yale: Bicentennial Lecture Series: Surgery Grand Round', *The Yale Journal of Biology and Medicine,* 84 (2), 169-72.

Ciriello, Giovanni, et al. (2013), 'Emerging landscape of oncogenic signatures across human cancers', *Nature Genetics,* 45 (10), 1127-33.

Costa, D. B., et al. (2007), 'BIM mediates EGFR tyrosine kinase inhibitor-induced apoptosis in lung cancers with oncogenic EGFR mutations', *PLoS Medicine,* 4 (10), 1669-79; discussion 80.

Cox, J., et al. (2014), 'Accurate proteome-wide label-free quantification by delayed normalization and maximal peptide ratio extraction, termed MaxLFQ', *Molecular and Cellular Proteomics,* 13 (9), 2513-26.

Cross, Timothy G. and Hornshaw, Martin P. (2016), 'Can LC and LC-MS ever replace immunoassays?', *Journal of Applied Bioanalysis,* 2 (4), 108-16.

Cunningham, D., et al. (2004), 'Cetuximab monotherapy and cetuximab plus irinotecan in irinotecan-refractory metastatic colorectal cancer', *New England Journal of Medicine,* 351 (4), 337-45.

D'Amico, A. V., et al. (2008), 'Androgen suppression and radiation vs radiation alone for prostate cancer - A randomized trial', *Jama-Journal of the American Medical Association,* 299 (3), 289-95.

Datta, Sandeep Robert, et al. (1997), 'Akt Phosphorylation of BAD Couples Survival Signals to the Cell-Intrinsic Death Machinery', *Cell,* 91 (2), 231-41.

de Graaf, E. L., et al. (2015), 'Signal Transduction Reaction Monitoring Deciphers Site-Specific PI3K-mTOR/MAPK Pathway Dynamics in Onaigene-Induced Senescence', *Journal of Proteome Research,* 14 (7), 2906-14.

de Gramont, Armand, et al. (2015), 'Pragmatic issues in biomarker evaluation for targeted therapies in cancer', *Nature Reviews. Clinical Oncology,* 12 (4), 197-212.

De Marchi, Tommaso, et al. (2016), '4-protein signature predicting tamoxifen treatment outcome in recurrent breast cancer', *Molecular Oncology,* 10 (1), 24-39.

de Martel, C., et al. (2012), 'Global burden of cancers attributable to infections in 2008: a review and synthetic analysis', *Lancet Oncology,* 13 (6).

Dekker, L. J. M., et al. (2018), 'Determination of Site-Specific Phosphorylation Ratios in Proteins with Targeted Mass Spectrometry', *J Proteome Res,* 17 (4), 1654-63.

DeRose, Y. S., et al. (2011), 'Tumor grafts derived from women with breast cancer authentically reflect tumor pathology, growth, metastasis and disease outcomes', *Nature Medicine,* 17 (11), 1514-U227.

Dickhut, C., et al. (2014), 'Impact of Digestion Conditions on Phosphoproteomics', *Journal of Proteome Research,* 13 (6), 2761-70.

Dobashi, Y., et al. (2015), 'Diverse involvement of isoforms and gene aberrations of Akt in human lung carcinomas', *Cancer Science,* 106 (6), 772-81.

Domanski, D., Murphy, L. C., and Borchers, C. H. (2010), 'Assay Development for the Determination of Phosphorylation Stoichiometry Using Multiple Reaction Monitoring Methods with and without Phosphatase Treatment: Application to Breast Cancer Signaling Pathways', *Analytical Chemistry,* 82 (13), 5610-20.

Dove, A. Q. (1999), 'Proteomics: translating genomics into products?', *Nature Biotechnology,* 17 (3), 233-36.

Dracopoli, N. C. and Boguski, M. S. (2017), 'The Evolution of Oncology Companion Diagnostics from Signal Transduction to Immuno-Oncology', *Trends in Pharmacological Sciences,* 38 (1), 41-54.

Early Breast Cancer Trialists' Collaborative Group (EBCTCG) (2005), 'Effects of chemotherapy and hormonal therapy for early breast cancer on recurrence and 15-year survival: an overview of the randomised trials', *The Lancet,* 365 (9472), 1687-717.

Ebner, Michael, et al. (2017), 'Localization of mTORC2 activity inside cells', *The Journal of Cell Biology*.

Egan, Sean E., et al. (1993), 'Association of Sos Ras exchange protein with Grb2 is implicated in tyrosine kinase signal transduction and transformation', *Nature,* 363, 45.

Eisenhauer, E. A., et al. (2009), 'New response evaluation criteria in solid tumours: Revised RECIST guideline (version 1.1)', *European Journal of Cancer,* 45 (2), 228-47.

Elliott, M. H., et al. (2009), 'Current trends in quantitative proteomics', *Journal of Mass Spectrometry,* 44 (12), 1637-60.

Ellis, L., et al. (2014), 'Cancer incidence, survival and mortality: explaining the concepts', *International Journal of Cancer,* 135 (8), 1774-82.

Ellis, L. M. and Fidler, I. J. (2010), 'Therapy fails, patients don't', *Nature Medicine,* 16 (9), 974-75.

Ellis, M. J., et al. (2013), 'Connecting Genomic Alterations to Cancer Biology with Proteomics: The NCI Clinical Proteomic Tumor Analysis Consortium', *Cancer Discovery,* 3 (10), 1108-12.

Engelman, J. A., Luo, J., and Cantley, L. C. (2006), 'The evolution of phosphatidylinositol 3-kinases as regulators of growth and metabolism', *Nature Reviews Genetics,* 7 (8), 606-19.

Esteva, F. J. (2004), 'Monoclonal antibodies, small molecules, and Vaccines in the treatment of breast cancer', *Oncologist,* 9, 4-9.

Ezzati, M. and Riboli, E. (2012), 'Can Noncommunicable Diseases Be Prevented? Lessons from Studies of Populations and Individuals', *Science,* 337 (6101), 1482-87.

Fabi, Francois and Asselin, Eric (2014), 'Expression, activation, and role of AKT isoforms in the uterus', *Reproduction,* 148 (5), R85-R95.

Feng, Y., et al. (2016), 'Anti-EGFR antibody sensitizes colorectal cancer stem-like cells to Fluorouracil-induced apoptosis by affecting autophagy', *Oncotarget,* 7 (49), 81402-09.

Ferlay J., et al. 'GLOBOCAN 2012 v1.0', *Cancer Incidence and Mortality Worldwide: IARC CancerBase No. 11* <**Error! Hyperlink reference not valid.**, accessed 03-March-16.

Ferrara, N., et al. (2004), 'Discovery and development of bevacizumab, an anti-VEGF antibody for treating cancer', *Nature Reviews Drug Discovery,* 3 (5), 391-400.

Fila, J. and Honys, D. (2012), 'Enrichment techniques employed in phosphoproteomics', *Amino Acids,* 43 (3), 1025-47.

Fisher, R., Pusztai, L., and Swanton, C. (2013), 'Cancer heterogeneity: implications for targeted therapeutics', *British Journal of Cancer*, 108 (3), 479-85.

Flaherty, K. T., et al. (2012a), 'Improved survival with MEK inhibition in BRAF-mutated melanoma', *New England Journal of Medicine*, 367 (2), 107-14.

Flaherty, Keith T., et al. (2012b), 'Combined BRAF and MEK Inhibition in Melanoma with BRAF V600 Mutations', *New England Journal of Medicine*, 367 (18), 1694-703.

Fruman, DA. and Rommel, C. (2014), 'PI3K and cancer: lessons, challenges and opportunities', *Nature Reviews Drug Discovery*, 13 (2), 140-56.

Funder, J. W., et al. (2008), 'Case detection, diagnosis, and treatment of patients with primary aldosteronism: An endocrine society clinical practice guideline', *Journal of Clinical Endocrinology & Metabolism*, 93 (9), 3266-81.

Gao, Yuan (2014), 'Akt: a new activation mechanism', *Cell Research*, 24 (7), 785-86.

Gerlinger , Marco, et al. (2012), 'Intratumor Heterogeneity and Branched Evolution Revealed by Multiregion Sequencing', *New England Journal of Medicine*, 366 (10), 883-92.

Gillet, J. P., et al. (2011), 'Redefining the relevance of established cancer cell lines to the study of mechanisms of clinical anti-cancer drug resistance', *Proceedings of the National Academy of Sciences of the United States of America*, 108 (46), 18708-13.

Global Burden of Disease Cancer Collaboration (2015), 'The Global Burden of Cancer 2013', *JAMA oncology*, 1 (4), 505-27.

Goossens, Nicolas, et al. (2015), 'Cancer biomarker discovery and validation', *Translational cancer research*, 4 (3), 256-69.

Greaves, M. and Maley, C. C. (2012), 'Clonal evolution in cancer', *Nature*, 481 (7381), 306-13.

Grothey, A., et al. (2013), 'Regorafenib monotherapy for previously treated metastatic colorectal cancer (CORRECT): an international, multicentre, randomised, placebo-controlled, phase 3 trial', *Lancet,* 381 (9863), 303-12.

Guillermet-Guibert, J., et al. (2008), 'The p110 beta isoform of phosphoinositide 3-kinase signals downstream of G protein-coupled receptors and is functionally redundant with p110 gamma', *Proceedings of the National Academy of Sciences of the United States of America,* 105 (24), 8292-97.

Gurpinar, Evrim and Vousden, Karen H. (2015), 'Hitting cancers' weak spots: vulnerabilities imposed by p53 mutation', *Trends in Cell Biology,* 25 (8).

Gygi, Steven P., et al. (1999), 'Correlation between Protein and mRNA Abundance in Yeast', *Molecular and Cellular Biology,* 19 (3), 1720-30.

Hébert, James R., et al. (2009), 'Mapping Cancer Mortality-to-Incidence Ratios to Illustrate Racial and Sex Disparities in a High-risk Population', *Cancer,* 115 (11), 2539-52.

Hoeppe, S., et al. (2011), 'Targeting Peptide Termini, a Novel Immunoaffinity Approach to Reduce Complexity in Mass Spectrometric Protein Identification', *Molecular and Cellular Proteomics,* 10 (2).

Holmes, D. T. (2015), 'cp-R, an interface the R programming language for clinical laboratory method comparisons', *Clinical Biochemistry,* 48 (3), 192-95.

Hoofnagle, A. N., et al. (2008), 'Quantification of thyroglobulin, a low-abundance serum protein, by immunoaffinity peptide enrichment and tandem mass spectrometry', *Clinical chemistry,* 54.

Huang, Jingxiang and Manning, Brendan D. (2009), 'A complex interplay between Akt, TSC2 and the two mTOR complexes', *Biochemical Society transactions,* 37 (Pt 1), 217-22.

Humphrey, S. J., James, D. E., and Mann, M. (2015a), 'Protein Phosphorylation: A Major Switch Mechanism for Metabolic Regulation', *Trends in Endocrinology and Metabolism,* 26 (12), 676-87.

Humphrey, Sean J., Azimifar, S. Babak, and Mann, Matthias (2015b), 'High-throughput phosphoproteomics reveals in vivo insulin signaling dynamics', *Nature Biotechnology,* 33 (9), 990-95.

Inoki, Ken, et al. (2002), 'TSC2 is phosphorylated and inhibited by Akt and suppresses mTOR signalling', *Nature Cell Biology,* 4, 648.

Islami, F., et al. (2018), 'Proportion and Number of Cancer Cases and Deaths Attributable to Potentially Modifiable Risk Factors in the United States', *Ca-a Cancer Journal for Clinicians,* 68 (1), 31-54.

Iyer, Jayasri G., et al. (2016), 'Response rates and durability of chemotherapy among 62 patients with metastatic Merkel cell carcinoma', *Cancer Medicine,* 5 (9), 2294-301.

Jain, K.K. (2010), *The handbook of biomarkers* (New York: Springer).

Janku, F., Yap, T. A., and Meric-Bernstam, F. (2018), 'Targeting the PI3K pathway in cancer: are we making headway?', *Nature Reviews Clinical Oncology,* 15 (5), 273-91.

Janne, P. A., et al. (2015), 'AZD9291 in EGFR inhibitor-resistant non-small-cell lung cancer', *New England Journal of Medicine,* 372 (18), 1689-99.

Jiang, J., et al. (2007a), 'An immunoaffinity tandem mass spectrometry (iMALDI) assay for detection of Francisella tularensis', *Analytica Chimica Acta,* 605 (1), 70-79.

Jiang, Jian, et al. (2007b), 'Development of an immuno tandem mass spectrometry (iMALDI) assay for EGFR diagnosis', *Proteomics Clinical Applications,* 1 (12), 1651-59.

Johnson, J. I., et al. (2001), 'Relationships between drug activity in NCI preclinical in vitro and in vivo models and early clinical trials', *British Journal of Cancer,* 84 (10), 1424-31.

Julien, L. A., et al. (2010), 'mTORC1-Activated S6K1 Phosphorylates Rictor on Threonine 1135 and Regulates mTORC2 Signaling', *Molecular and Cellular Biology,* 30 (4), 908-21.

Kantarjian, Hagop, et al. (2002), 'Hematologic and Cytogenetic Responses to Imatinib Mesylate in Chronic Myelogenous Leukemia', *New England Journal of Medicine*, 346 (9), 645-52.

Kaplon, Hélène and Reichert, Janice M. (2018), 'Antibodies to watch in 2018', *mAbs*, 10 (2), 183-203.

Katayev, A., Balciza, C., and Seccombe, D. W. (2010), 'Establishing Reference Intervals for Clinical Laboratory Test Results Is There a Better Way?', *American Journal of Clinical Pathology*, 133 (2), 180-86.

Khalil, D. N., et al. (2016), 'The future of cancer treatment: immunomodulation, CARs and combination immunotherapy', *Nature Reviews. Clinical Oncology*, 13 (5), 273-90.

Kim, Y. J., et al. (2012), 'Mass spectrometry-based detection and quantification of plasma glycoproteins using selective reaction monitoring', *Nature Protocols*, 7 (5), 859-71.

Kokkat, Theresa J., et al. (2013), 'Archived Formalin-Fixed Paraffin-Embedded (FFPE) Blocks: A Valuable Underexploited Resource for Extraction of DNA, RNA, and Protein', *Biopreservation and Biobanking*, 11 (2), 101-06.

Kolch, W., et al. (2015), 'The dynamic control of signal transduction networks in cancer cells', *Nature Reviews Cancer*, 15 (9), 515-27.

Kovacina, K. S., et al. (2003), 'Identification of a proline-rich Akt substrate as a 14-3-3 binding partner', *J Biol Chem*, 278 (12), 10189-94.

Krześlak, Anna, Pomorski, Lech, and Lipińska, Anna (2011), 'Expression, Localization, and Phosphorylation of Akt1 in Benign and Malignant Thyroid Lesions', *Endocrine Pathology*, 22 (4), 206-11.

Kumar, Chandra C. and Madison, Vincent (2005), 'AKT crystal structure and AKT-specific inhibitors', *Oncogene*, 24, 7493.

Kummerer, K. and Al-Ahmad, A. (2010), 'Estimation of the cancer risk to humans resulting from the presence of cyclophosphamide and ifosfamide in surface water', *Environmental Science and Pollution Research,* 17 (2), 486-96.

Kuzyk, M. A., et al. (2009), 'Multiple Reaction Monitoring-based, Multiplexed, Absolute Quantitation of 45 Proteins in Human Plasma', *Molecular and Cellular Biochemistry,* 8 (8), 1860-77.

Lahtz, Christoph and Pfeifer, Gerd P. (2011), 'Epigenetic changes of DNA repair genes in cancer', *Journal of Molecular Cell Biology,* 3 (1), 51-58.

Larance, Mark and Lomond, Angus I. (2015), 'Multidimensional proteomics for cell biology', *Nature Reviews. Molecular Cell Biology,* 16 (5), 269-80.

Law, N. C., White, M. F., and Hunzicker-Dunn, M. E. (2016), 'G protein-coupled receptors (GPCRs) That Signal via Protein Kinase A (PKA) Cross-talk at Insulin Receptor Substrate 1 (IRS1) to Activate the phosphatidylinositol 3-kinase (PI3K)/AKT Pathway', *J Biol Chem,* 291 (53), 27160-69.

Ledford, Heidi 'DNA typos to blame for most cancer mutations', *Nature News* <https://www.nature.com/news/dna-typos-to-blame-for-most-cancer-mutations-1.21696>, accessed 25-Apr-2018.

Leighl, Natasha B., et al. (2010), 'A Multicenter, Phase 2 Study of Vascular Endothelial Growth Factor Trap (Aflibercept) in Platinum- and Erlotinib-Resistant Adenocarcinoma of the Lung', *Journal of Thoracic Oncology,* 5 (7), 1054-59.

Li, Huiyan, Popp, Robert, and Borchers, Christoph H. (2017), 'Affinity-mass spectrometric technologies for quantitative proteomics in biological fluids', *TrAC Trends in Analytical Chemistry,* 90, 80-88.

Li, Lei, et al. (2014), 'Integrated Omic analysis of lung cancer reveals metabolism proteome signatures with prognostic impact', *Nature Communications,* 5, 5469.

Lim, Stephen S., et al. (2012), 'A comparative risk assessment of burden of disease and injury attributable to 67 risk factors and risk factor clusters in 21 regions, 1990–2010: a systematic analysis for the Global Burden of Disease Study 2010', *Lancet,* 380 (9859), 2224-60.

Liu, Pengda, et al. (2014), 'Cell-cycle-regulated activation of Akt kinase by phosphorylation at its carboxyl terminus', *Nature,* 508 (7497), 541-5.

Lowy, Douglas R. 'Cancer Moonshot Moves Forward, Bringing Funding Opportunities for Researchers', <https://www.cancer.gov/news-events/cancer-currents-blog/2017/moonshot-funding-opportunities>, accessed 19-Mar-2018.

Magdeldin, S. and Yamamoto, T. (2012), 'Toward deciphering proteomes of formalin-fixed paraffin-embedded (FFPE) tissues', *Proteomics,* 12 (7), 1045-58.

Mahajan, K., et al. (2010), 'Ack1 mediated AKT/PKB tyrosine 176 phosphorylation regulates its activation', *PLoS One,* 5 (3), e9646.

Manning, B. D. and Toker, A. (2017), 'AKT/PKB Signaling: Navigating the Network', *Cell,* 169 (3), 381-405.

Manning, Brendan D., et al. (2002), 'Identification of the Tuberous Sclerosis Complex-2 Tumor Suppressor Gene Product Tuberin as a Target of the Phosphoinositide 3-Kinase/Akt Pathway', *Molecular Cell,* 10 (1), 151-62.

Marusyk, Andriy and Polyak, Kornelia (2010), 'Tumor heterogeneity: causes and consequences', *Biochimica et biophysica acta,* 1805 (1), 105.

Mason, D. Randal, et al. (2012), 'Duplexed iMALDI for the detection of angiotensin I and angiotensin II', *Methods,* 56 (2), 213-22.

Maude, S. L., et al. (2014), 'Chimeric antigen receptor T cells for sustained remissions in leukemia', *New England Journal of Medicine,* 371 (16), 1507-17.

McArthur, Grant A., et al. (2014), 'Safety and efficacy of vemurafenib in BRAF(V600E) and BRAF(V600K) mutation-positive melanoma (BRIM-3): extended follow-up of a phase 3, randomised, open-label study', *The Lancet. Oncology,* 15 (3), 323-32.

McDermott, Jason E., et al. (2013), 'Challenges in Biomarker Discovery: Combining Expert Insights with Statistical Analysis of Complex Omics Data', *Expert Opinion on Medical Diagnostics,* 7 (1), 37-51.

McFarland, C. D., et al. (2017), 'The Damaging Effect of Passenger Mutations on Cancer Progression', *Cancer Research,* 77 (18), 4763-72.

Mertins, P., et al. (2012), 'iTRAQ labeling is superior to mTRAQ for quantitative global proteomics and phosphoproteomics', *Molecular and Cellular Proteomics,* 11 (6), M111 014423.

Mertins, P., et al. (2016), 'Proteogenomics connects somatic mutations to signalling in breast cancer', *Nature,* 534 (7605), 55-+.

Miller, Kimberly D., et al. (2016), 'Cancer treatment and survivorship statistics, 2016', *CA: A Cancer Journal for Clinicians,* 66 (4), 271-89.

Mirzaei, Hamid R., et al. (2017), 'Chimeric Antigen Receptors T Cell Therapy in Solid Tumor: Challenges and Clinical Applications', *Frontiers in Immunology,* 8, 1850.

Miyazaki, M. and Takemasa, T. (2017), 'TSC2/Rheb signaling mediates ERK-dependent regulation of mTORC1 activity in C2C12 myoblasts', *FEBS Open Bio,* 7 (3), 424-33.

Morales-Betanzos, C. A., et al. (2017), 'Quantitative Mass Spectrometry Analysis of PD-L1 Protein Expression, N-glycosylation and Expression Stoichiometry with PD-1 and PD-L2 in Human Melanoma', *Molecular and Cellular Proteomics,* 16 (10), 1705-17.

Motoyoshi, Y., et al. (2006), 'Different mechanisms for anti-tumor effects of low- and high-dose cyclophosphamide', *Oncology Reports,* 16 (1), 141-6.

Moy, Beverly, et al. (2007), 'Lapatinib', *Nature Reviews Drug Discovery,* 6 (6), 431-32.

Murthy, R. K., et al. (2014), 'Effect of Adjuvant/Neoadjuvant Trastuzumab on Clinical Outcomes in Patients With HER2-Positive Metastatic Breast Cancer', *Cancer,* 120 (13), 1932-38.

National Cancer Institute 'Surgery to Treat Cancer', <https://www.cancer.gov/about-cancer/treatment/types/surgery>, accessed 29-May-2018.

National Cancer Institute 'Radiation Therapy to Treat Cancer', <https://www.cancer.gov/about-cancer/treatment/types/radiation-therapy>, accessed 29-May-2018.

Ng, John and Shuryak, Igor (2015), 'Minimizing second cancer risk following radiotherapy: current perspectives', *Cancer Management and Research*, 7, 1-11.

Nguyen, Paul L., et al. (2015), 'Adverse Effects of Androgen Deprivation Therapy and Strategies to Mitigate Them', *European Urology*, 67 (5), 825-36.

O'Reilly, K. E., et al. (2006), 'mTOR inhibition induces upstream receptor tyrosine kinase signaling and activates Akt', *Cancer Research*, 66 (3), 1500-8.

Office of Cancer Clinical Proteomics Research 'Assay Portal', <https://assays.cancer.gov>, accessed 12/05/2017.

Olsen, J. V., et al. (2010), 'Quantitative Phosphoproteomics Reveals Widespread Full Phosphorylation Site Occupancy During Mitosis', *Science Signaling*, 3 (104).

Ong, S. E., et al. (2002), 'Stable isotope labeling by amino acids in cell culture, SILAC, as a simple and accurate approach to expression proteomics', *Molecular and Cellular Proteomics*, 1 (5), 376-86.

Ostasiewicz, Paweł, et al. (2010), 'Proteome, phosphoproteome, and N-glycoproteome are quantitatively preserved in formalin-fixed paraffin-embedded tissue and analyzable by high-resolution mass spectrometry', *Journal of proteome research*, 9 (7), 3688-700.

Ott, J. J., et al. (2011), 'Global cancer incidence and mortality caused by behavior and infection', *Journal of Public Health*, 33 (2), 223-33.

Overdijk, M. B., et al. (2015), 'Antibody-mediated phagocytosis contributes to the anti-tumor activity of the therapeutic antibody daratumumab in lymphoma and multiple myeloma', *MAbs*, 7 (2), 311-21.

Parker, Carol E., et al. (2010), 'Mass-spectrometry-based clinical proteomics - a review and prospective', *Analyst*, 135 (8), 1830-38.

Patel, B., et al. (2015), 'Quantitative analysis of AKT/mTOR pathway using immunoprecipitation and targeted mass spectrometry', *Cancer Research,* 75.

Pergolini, I., et al. (2017), 'Tumor engraftment in patient-derived xenografts of pancreatic ductal adenocarcinoma is associated with adverse clinicopathological features and poor survival', *PLoS One,* 12 (8), e0182855.

Phuchareon, J., et al. (2015), 'EGFR inhibition evokes innate drug resistance in lung cancer cells by preventing Akt activity and thus inactivating Ets-1 function', *Proceedings of the National Academy of Sciences of the United States of America,* 112 (29), E3855-E63.

Piccart-Gebhart, M. J., et al. (2005), 'Trastuzumab after adjuvant chemotherapy in HER2-positive breast cancer', *New England Journal of Medicine,* 353 (16), 1659-72.

Polivka, J. and Janku, F. (2014), 'Molecular targets for cancer therapy in the PI3K/AKT/mTOR pathway', *Pharmacology & Therapeutics,* 142 (2), 164-75.

Proc, J. L., et al. (2010), 'A Quantitative Study of the Effects of Chaotropic Agents, Surfactants, and Solvents on the Digestion Efficiency of Human Plasma Proteins by Trypsin', *Journal of Proteome Research,* 9 (10), 5422-37.

Prowell, T. M. and Davidson, N. E. (2004), 'What is the role of ovarian ablation in the management of primary and metastatic breast cancer today?', *Oncologist,* 9 (5), 507-17.

Qiagen (2012), 'therascreen KRAS RGQ PCR KIT Instructions for Use (Handbook)'.

Raska, C. S., et al. (2002), 'Direct MALDI-MS/MS of phosphopeptides affinity-bound to immobilized metal ion affinity chromatography beads', *Analytical Chemistry,* 74 (14), 3429-33.

Raska, C. S., et al. (2003), 'Rapid and sensitive identification of epitope-containing peptides by direct matrix-assisted laser desorption/ionization tandem mass spectrometry of peptides affinity-bound to antibody beads', *Journal of the American Society for Mass Spectrometry,* 14 (10), 1076-85.

Rawlins, M. L. and Roberts, W. L. (2004), 'Performance characteristics of six third-generation assays for thyroid-stimulating hormone', *Clinical Chemistry,* 50 (12), 2338-44.

Rebello, P. R., et al. (1999), 'Anti-globulin responses to rat and humanized CAMPATH-1 monoclonal antibody used to treat transplant rejection', *Transplantation,* 68 (9), 1417-20.

Reid, Jennifer D., et al. (2010), 'Towards the development of an immuno MALDI (iMALDI) mass spectrometry assay for the diagnosis of hypertension', *Journal of the American Society for Mass Spectrometry,* 21 (10), 1680-86.

Reis-Filho, Jorge S. (2009), 'Next-generation sequencing', *Breast Cancer Research,* 11 (3), S12.

Riggio, Marina, et al. (2017), 'AKT1 and AKT2 isoforms play distinct roles during breast cancer progression through the regulation of specific downstream proteins', *Scientific Reports,* 7, 44244.

Ritchie, M., Tchistiakova, L., and Scott, N. (2013), 'Implications of receptor-mediated endocytosis and intracellular trafficking dynamics in the development of antibody drug conjugates', *Mabs,* 5 (1), 13-21.

Robert, C., et al. (2015), 'Nivolumab in Previously Untreated Melanoma without BRAF Mutation', *New England Journal of Medicine,* 372 (4), 320-30.

Rogel, Anne, et al. (2017), 'Akt signaling is critical for memory CD8(+) T-cell development and tumor immune surveillance', *Proceedings of the National Academy of Sciences of the United States of America,* 114 (7), E1178-E87.

Roy, H. K., et al. (2002), 'AKT proto-oncogene overexpression is an early event during sporadic colon carcinogenesis', *Carcinogenesis,* 23 (1), 201-05.

Santi, Stacey A. and Lee, Hoyun (2010), 'The Akt isoforms are present at distinct subcellular locations', *American Journal of Physiology-Cell Physiology,* 298 (3), C580-C91.

Schadendorf, Dirk, et al. (2015), 'Pooled Analysis of Long-Term Survival Data From Phase II and Phase III Trials of Ipilimumab in Unresectable or Metastatic Melanoma', *Journal of Clinical Oncology*, 33 (17), 1889-94.

Sealey, Jean E., Gordon, R. D., and Mantero, F. (2005), 'Plasma renin and aldosterone measurements in low renin hypertensive states', *Trends in endocrinology and metabolism*, 16 (3), 86-91.

Sever, R. and Brugge, J. S. (2015), 'Signal Transduction in Cancer', *Cold Spring Harbor Perspectives in Medicine*, 5 (4).

Sharma, K., et al. (2014), 'Ultradeep human phosphoproteome reveals a distinct regulatory nature of Tyr and Ser/Thr-based signaling', *Cell Reports*, 8 (5), 1583-94.

Sharma, P. and Allison, J. P. (2015), 'The future of immune checkpoint therapy', *Science*, 348 (6230), 56-61.

Shayesteh, L., et al. (1999), 'PIK3CA is implicated as an oncogene in ovarian cancer', *Nature Genetics*, 21 (1), 99-102.

Shlien, Adam, et al. (2015), 'Combined hereditary and somatic mutations of replication error repair genes result in rapid onset of ultra-hypermutated cancers', *Nature Genetics*, 47 (3), 257-+.

Sledge, G. W., et al. (2003), 'Phase III trial of doxorubicin, paclitaxel, and the combination of doxorubicin and paclitaxel as front-line chemotherapy for metastatic breast cancer: an intergroup trial (E1193)', *Journal of Clinical Oncology*, 21 (4), 588-92.

Smirnov, I. P., et al. (2004), 'Suppression of alpha-cyano-4-hydroxycinnamic acid matrix clusters and reduction of chemical noise in MALDI-TOF mass spectrometry', *Analytical Chemistry*, 76 (10), 2958-65.

Sorlie, T., et al. (2001), 'Gene expression patterns of breast carcinomas distinguish tumor subclasses with clinical implications', *Proceedings of the National Academy of Sciences*, 98 (19), 10869-74.

Straub, J. M., et al. (2015), 'Radiation-induced fibrosis: mechanisms and implications for therapy', *Journal of Cancer Research and Clinical Oncology,* 141 (11), 1985-94.

Straussman, Ravid, et al. (2012), 'Tumour micro-environment elicits innate resistance to RAF inhibitors through HGF secretion', *Nature,* advance online publication.

Swain, S. M., et al. (2015), 'Pertuzumab, trastuzumab, and docetaxel in HER2-positive metastatic breast cancer', *New England Journal of Medicine,* 372 (8), 724-34.

Teixidó, Cristina, et al. (2014), 'Concordance of IHC, FISH and RT-PCR for EML4-ALK rearrangements', *Translational Lung Cancer Research,* 3 (2), 70-74.

The Antibody Society 'Approved Antibodies', <https://www.antibodysociety.org/news/approved-antibodies/>, accessed 29-May-2018.

Thomas, A., Teicher, B. A., and Hassan, R. T. (2016), 'Antibody-drug conjugates for cancer therapy', *Lancet Oncology,* 17 (6), E254-E62.

Tomasetti, C., Li, L., and Vogelstein, B. (2017), 'Stem cell divisions, somatic mutations, cancer etiology, and cancer prevention', *Science,* 355 (6331), 1330-34.

Tomasetti, Cristian, et al. (2015), 'Only three driver gene mutations are required for the development of lung and colorectal cancers', *Proceedings of the National Academy of Sciences of the United States of America,* 112 (1), 118-23.

Tomczak, Katarzyna, Czerwińska, Patrycja, and Wiznerowicz, Maciej (2015), 'The Cancer Genome Atlas (TCGA): an immeasurable source of knowledge', *Contemporary Oncology,* 19 (1A), A68-A77.

Trédan, Olivier, et al. (2007), 'Drug Resistance and the Solid Tumor Microenvironment', *JNCI: Journal of the National Cancer Institute,* 99 (19), 1441-54.

U. S. National Institutes of Health, National Cancer Institute (2018), 'SEER Training Modules, Cancer Classification', <https://training.seer.cancer.gov>, accessed 26-Feb-2018.

U.S. Department of Health and Human Services (2016), 'Report on Carcinogens, Fourteenth Edition', (14 edn.: U.S. Department of Health and Human Services).

U.S. Food and Drug Administration 'Herceptin 103792 Approval Letter', <https://www.accessdata.fda.gov/drugsatfda_docs/appletter/1998/trasgen092598L.pdf>, accessed 07-May-2018.

U.S. Food and Drug Administration 'Gleevec NDA 21-335 Approval Letter', <https://www.accessdata.fda.gov/drugsatfda_docs/nda/2001/21-335_Gleevec_Approv.pdf>, accessed 07-May-2018.

U.S. Food and Drug Administration 'Erbitux STN/BLA 125804 Approval Letter', <https://www.accessdata.fda.gov/drugsatfda_docs/bla/2004/125084_ERBITUX_APPROV.PDF>, accessed 07-May-2018.

U.S. food and Drug Administration 'Avastin STN 125085 Approval Letter', <https://www.accessdata.fda.gov/drugsatfda_docs/nda/2004/STN-125085_Avastin_Approv.pdf>, accessed 08-May-2018.

U.S. Food and Drug Administration 'Yervoy (ipilimumab) BL 125377/0 Approval Letter', <https://www.accessdata.fda.gov/drugsatfda_docs/appletter/2011/125377s000ltr.pdf>, accessed 29-May-2018.

U.S. Food and Drug Administration (2013), 'Guidance for Industry - Bioanalytical Method Validation', (U.S. Department of Health and Human Services).

U.S. Food and Drug Administration 'Trametinib/Dabrafenib', <http://www.fda.gov/Drugs/InformationOnDrugs/ApprovedDrugs/ucm476837.htm >, accessed 14-March-2016.

U.S. Food and Drug Administration (2018), 'List of Cleared or Approved Companion Diagnostic Devices (In Vitro and Imaging Tools)', (updated 23-Jan-2018) <https://www.fda.gov/MedicalDevices/ProductsandMedicalProcedures/InVitroDiagnostics/ucm301431.htm>, accessed 18-Mar-2018.

Ullrich, A. and Schlessinger, J. (1990), 'Signal Transduction by Receptors with Tyrosine Kinase-Activity', *Cell*, 61 (2), 203-12.

Union for International Cancer Control (2013), 'World Cancer Declaration 2013'.

Union for International Cancer Control (2014), 'The Economics of Cancer Prevention and Control. Data Digest.', (World Cancer Leaders' Summit).

Valkov, Andrej, et al. (2011), 'The prognostic impact of Akt isoforms, PI3K and PTEN related to female steroid hormone receptors in soft tissue sarcomas', *Journal of Translational Medicine*, 9, 200-00.

Van Cutsem, E., et al. (2007), 'Open-label phase III trial of panitumumab plus best supportive care compared with best supportive care alone in patients with chemotherapy-refractory metastatic colorectal cancer', *Journal of Clinical Oncology*, 25 (13), 1658-64.

Van der Gugten, J. G. and Holmes, D. T. (2016), 'Quantitation of Plasma Renin Activity in Plasma Using Liquid Chromatography-Tandem Mass Spectrometry (LC-MS/MS)', in U. Garg (ed.), *Clinical Applications of Mass Spectrometry in Biomolecular Analysis: Methods and Protocols* (Methods in Molecular Biology, 1378; Totowa: Humana Press Inc), 243-53.

Vorm, O., Roepstorff, P., and Mann, M. (1994), 'Improved Resolution and Very High Sensitivity in MALDI TOF of Matrix Surfaces Made by Fast Evaporation', *Analytical Chemistry*, 66 (19), 3281-87.

Walsh, Colin T., Stupack, Dwayne, and Brown, Joan Heller (2008), 'G protein-coupled receptors go extracellular: RhoA integrates the integrins', *Molecular interventions*, 8 (4), 165-73.

Wang, W., et al. (2015), 'NK cell-mediated antibody-dependent cellular cytotoxicity in cancer immunotherapy', *Frontiers in Immunology*, 6.

Warren, E. N., et al. (2004), 'Development of a protein chip: A MS-based method for quantitation of protein expression and modification levels using an immunoaffinity approach', *Analytical Chemistry*, 76 (14), 4082-92.

Weiss, F., et al. (2014), 'Catch and measure-mass spectrometry-based immunoassays in biomarker research', *Biochimica Et Biophysica Acta-Proteins and Proteomics*, 1844 (5), 927-32.

Whiteaker, J. R., et al. (2015), 'Peptide Immunoaffinity Enrichment and Targeted Mass Spectrometry Enables Multiplex, Quantitative Pharmacodynamic Studies of Phospho-Signaling', *Molecular and Cellular Proteomics*, 14 (8), 2261-73.

Whittle, J. R., et al. (2015), 'Patient-derived xenograft models of breast cancer and their predictive power', *Breast Cancer Research*, 17.

Wiese, S., et al. (2007), 'Protein labeling by iTRAQ: A new tool for quantitative mass spectrometry in proteome research', *Proteomics*, 7 (3), 340-50.

Wilczynska, A. and Bushell, M. (2015), 'The complexity of miRNA-mediated repression', *Cell Death & Differentiation*, 22 (1), 22-33.

Wolchok, J. D., et al. (2017), 'Overall Survival with Combined Nivolumab and Ipilimumab in Advanced Melanoma', *New England Journal of Medicine*, 377 (14), 1345-56.

Wong, Martin C. S., et al. (2017), 'Incidence and mortality of lung cancer: global trends and association with socioeconomic status', *Scientific Reports*, 7 (1), 14300.

World Health Organization (2013), 'Global Action Plan for the Prevention and Control of Noncommunicable diseases 2013-2020'.

World Health Organization (2015), 'Health in 2015: from MDGs to SDGs', 204.

Wu, Leilei, et al. (2017), 'Population-based study of effectiveness of neoadjuvant radiotherapy on survival in US rectal cancer patients according to age', *Scientific Reports*, 7 (1), 3471.

Wu, P., Nielsen, T. E., and Clausen, M. H. (2016), 'Small-molecule kinase inhibitors: an analysis of FDA-approved drugs', *Drug Discovery Today*, 21 (1), 5-10.

Wu, R. H., et al. (2011), 'A large-scale method to measure absolute protein phosphorylation stoichiometries', *Nature Methods*, 8 (8), 677-U111.

Xu, L. L., et al. (2015), 'An MRM-based workflow for absolute quantitation of lysine-acetylated metabolic enzymes in mouse liver', *Analyst*, 140 (23), 7868-75.

Yang, Haijuan, et al. (2017), 'Structural mechanisms of mTORC1 activation by RHEB and inhibition by PRAS40', *Nature,* 552 (7685), 368-73.

Yu, Haixiang, Littlewood, Trevor, and Bennett, Martin (2015), 'Akt isoforms in vascular disease', *Vascular pharmacology*, 71, 57-64.

Zarghami, N., Grass, L., and Diamandis, E. P. (1997), 'Steroid hormone regulation of prostate-specific antigen gene expression in breast cancer', *British Journal Of Cancer,* 75, 579.

Zhang, B., et al. (2014), 'Proteogenomic characterization of human colon and rectal cancer', *Nature,* 513 (7518), 382-7.

Zhang, H., et al. (2012), 'Targeted glycomics by selected reaction monitoring for highly sensitive glycan compositional analysis', *Proteomics,* 12 (15-16), 2510-22.

Zhang, Ji-guang, et al. (2010), 'MicroRNA-21 (miR-21) represses tumor suppressor PTEN and promotes growth and invasion in non-small cell lung cancer (NSCLC)', *Clinica Chimica Acta,* 411 (11–12), 846-52.

Zhang, X. M., et al. (2013), 'A Renewable Tissue Resource of Phenotypically Stable, Biologically and Ethnically Diverse, Patient-Derived Human Breast Cancer Xenograft Models', *Cancer Research,* 73 (15), 4885-97.

Zhu, Zhengfei, et al. (2015), 'Phosphorylated AKT1 is associated with poor prognosis in esophageal squamous cell carcinoma', *Journal of Experimental & Clinical Cancer Research,* 34 (1), 95.

Zubarev, R. A. (2013), 'The challenge of the proteome dynamic range and its implications for in-depth proteomics', *Proteomics,* 13 (5), 723-26.

Appendices

Appendix I

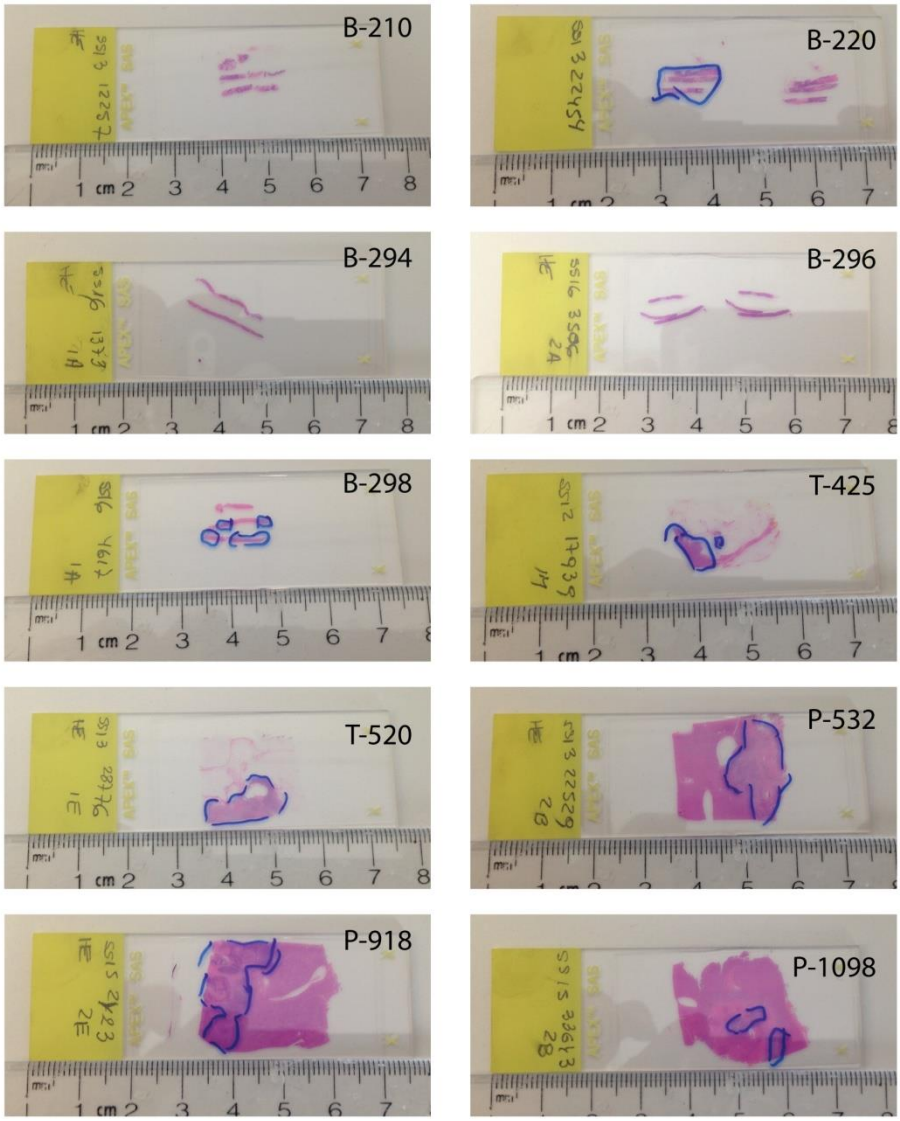

Appendix Figure 1: Histopathology assessed H&E-stained slides of six flash frozen tumor tissues. No slides for 719 and P-719A1

Appendix Table 1: Tumor cellularity and necrosis values for six flash frozen tumor tissues

Sample	Type	Tumor cellularity	Necrosis
T-520	Breast surgery	100%	0%
B-220	Breast biopsy	90%	NA
P-532	CRC liver metastasis, surgery	25%	65%
P-1098	CRC liver metastasis, surgery	70%	20%
P-918	CRC liver metastasis, surgery	65%	25%
T-425	Breast surgery	90%	NA

Appendix II

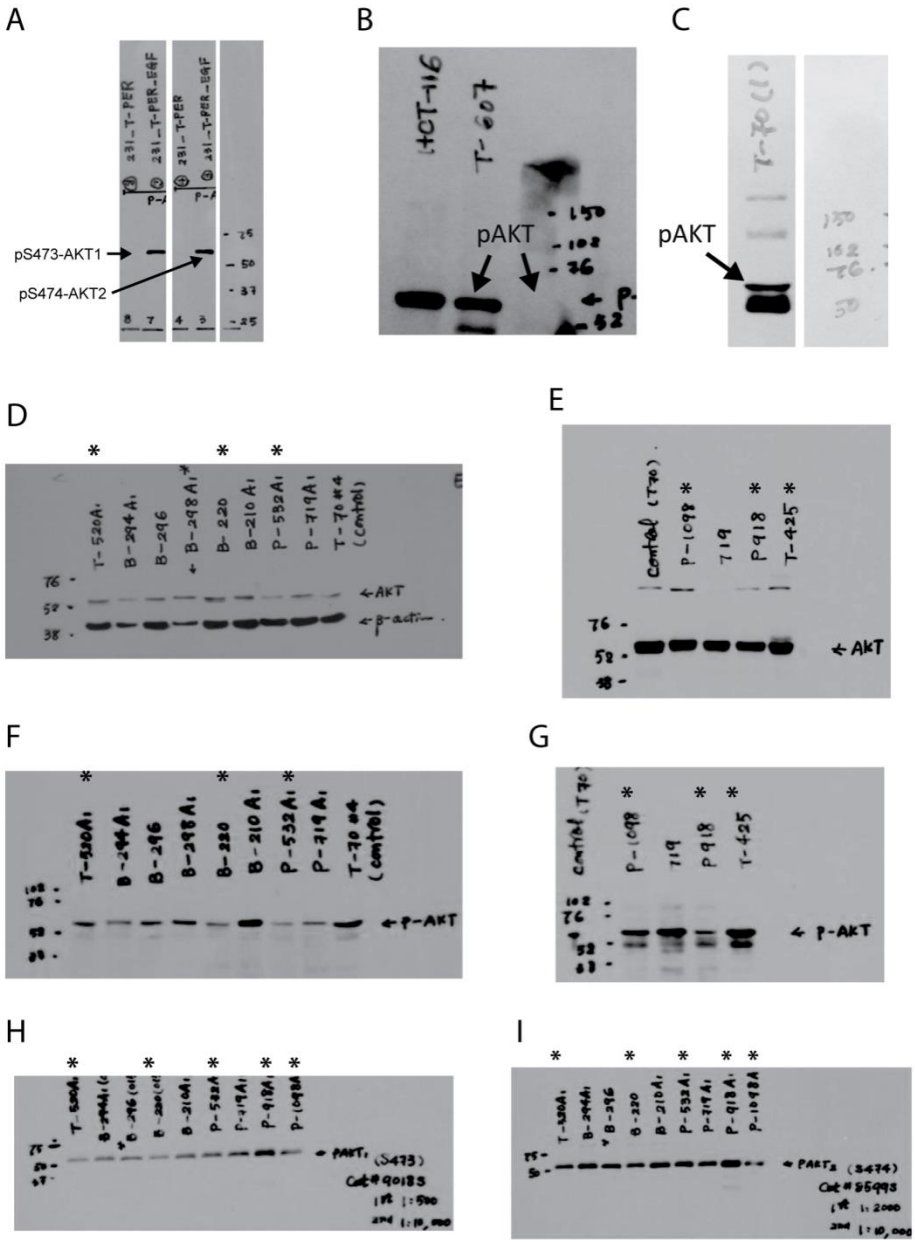

Appendix Figure 2: Western blots for various tumor samples provided by collaborators at the JGH. Expression of (A) Total AKT, (B) Total pAKT, (C) pS473-AKT1, and (D) pS474-AKT2. *marks matched flash-frozen and FFPE samples analyzed by iMALDI. Note: Sample T-425 was not analyzed for pS473-AKT1 or pS474-AKT2 due to the limited sample amount.

Appendix III

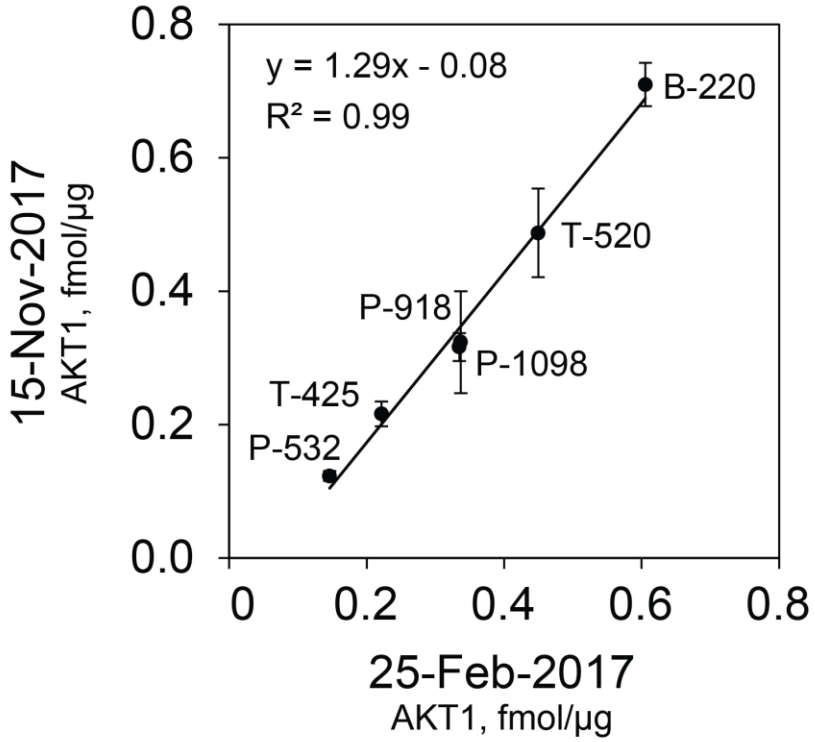

Appendix Figure 3: Stability of AKT1 over 9 months at -80 °C.

Appendix IV

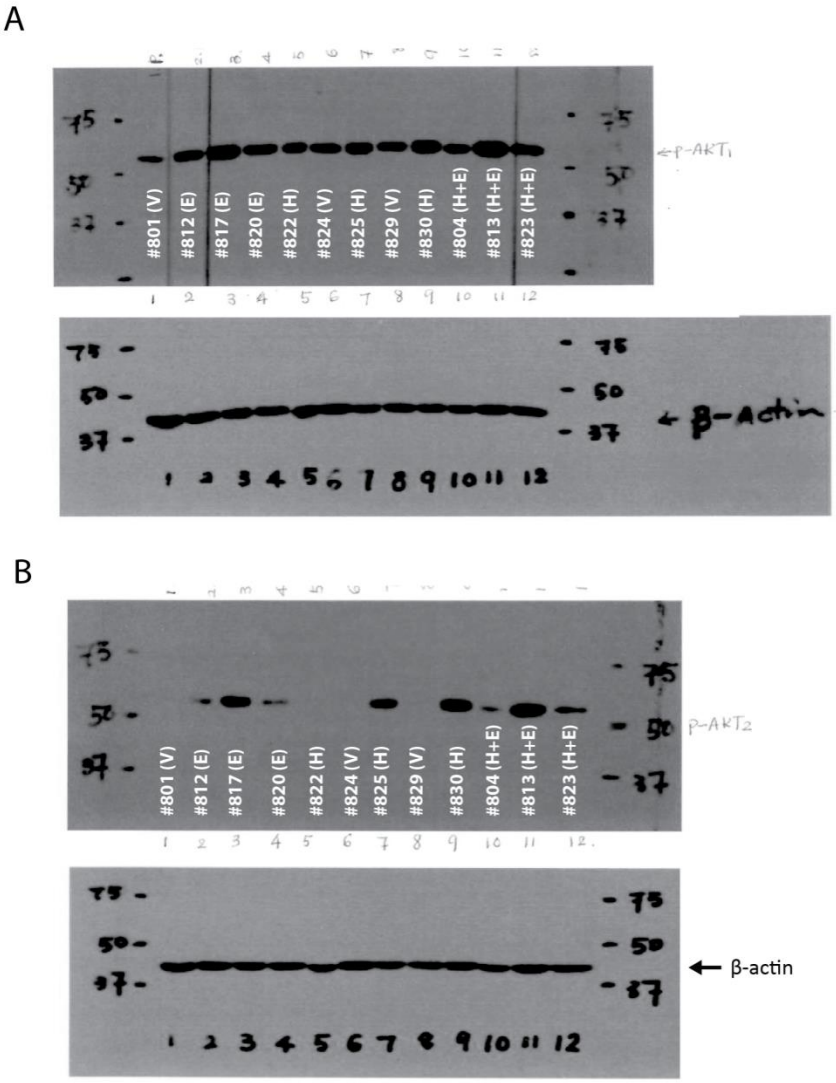

Appendix Figure 4: Western blots for the twelve PDX tumor lysates for (A) pS473-AKT1 and (B) pS474-AKT2. V: Vehicle; E: Everolimus; H: Herceptin; H+E: Herceptin and Everolimus treatment.